University of California
Santa Barbara

Explosive Outcomes from Rapid Accretion of Helium onto White Dwarfs in Tight Binaries

A dissertation submitted in partial satisfaction
of the requirements for the degree

Doctor of Philosophy
in
Physics

by

Jared C. Brooks

Committee in charge:

Professor Lars Bildsten, Chair
Professor Carl Gwinn
Professor Omer Blaes

September 2017

The Dissertation of Jared C. Brooks is approved.

Professor Carl Gwinn

Professor Omer Blaes

Professor Lars Bildsten, Committee Chair

August 2017

Explosive Outcomes from Rapid Accretion of Helium onto White Dwarfs in Tight Binaries

by

Jared C. Brooks

Acknowledgements

I have to start by thanking my advisor, Lars Bildsten. Even though he was usually extremely busy with his directorial duties for the KITP, I couldn't ask for a better advisor. He never lost sight of his reponsibilities as an advisor and always made time for me when I needed it. Lars was able to find a perfect balance of how much help to give me without micromanaging or leaving me spinning my wheels. I never saw Lars noticably stressed or flustered, even in the face of his mountain of responsibilites, which set an admirable example that I strive to live up to. Lars also has an incredible skill to navigate political waters and interpersonal conflicts in a way that he was able to avoid stepping on any toes while still achieving impressive scientific and administrative goals. I learned so much from Lars, and not just in science. I was very lucky to find an advisor like Lars, and my time spent here under his guidance was invaluable.

I also learned a great deal from other graduate students, but three in particular stand out: Kevin Moore, Bill Wolf, and Josiah Schwab. Kevin's last year of graduate school was my first, and him being Lars' senior graduate student, I went to him for help with this or that nearly every day. Kevin was always gracious and knowledgeable enough to give me the guidance I needed. Even long after he graduated, Kevin was willing to offer me advice and answer my questions on occasion. Without Kevin in the office, however, Bill Wolf was there to help answer questions, debug my script or simulation, and share his wisdom and experiences. Josiah and I never shared an office, but we collaborated on several different projects. I had read several of Josiah's papers before working with him, and felt honored to be collaborating with him on a project. That feeling never went away over the several years and projects we worked on together. Josiah continued to impress me with everything we collaborated on. Working with him was not only an absolute pleasure, but made me feel smarter and more capable. In addition to all the

help and advice all three gave me, they all produced incredibly high quality work. Their example set a very high bar to me to live up to, and striving to do so made me better in a multitude of ways. I am still in awe of all they have achieved, and can only hope that I can be as prolific and skillful as they are.

Finally, I have to thank my parents. They fostered my intellectual development while growing up and taught me that I could achieve my goals if I worked hard enough. They encouraged me to strive for excellence and to not be afraid to go after what I want in life. This thesis would not be possible without their love and support.

Curriculum Vitæ

Jared C. Brooks

Education

2017	Ph.D. in Physics (Expected), University of California, Santa Barbara.
2015	M.A. in Physics, University of California, Santa Barbara.
2011	B.S. in Physics, University of Southern California.

Publications

"Accretion-induced Collapse from Helium Star + White Dwarf Binaries" **Brooks, Jared**; Schwab, Josiah; Bildsten, Lars; Quataert, Eliot; Paxton, Bill, 2017, ApJ, 843, 151B

"PTF1 J082340.04+081936.5: A Hot Subdwarf B Star with a Low-mass White Dwarf Companion in an 87-minute Orbit," Kupfer, Thomas; van Roestel, Jan; **Brooks, Jared**; Geier, Stephan; Marsh, Tom R.; Groot, Paul J.; Bloemen, Steven; Prince, Thomas A.; Bellm, Eric; Heber, Ulrich; Bildsten, Lars; Miller, Adam A.; Dyer, Martin J.; Dhillon, Vik S.; Green, Matthew; Irawati, Puji; Laher, Russ; Littlefair, Stuart P.; Shupe, David L.; Steidel, Charles C.; Rattansoon, Somsawat; Pettini, Max, 2017, ApJ, 835, 131K

"Convection Destroys the Core/Mantle Structure in Hybrid C/O/Ne White Dwarfs," **Brooks, Jared**; Schwab, Josiah; Bildsten, Lars; Quataert, Eliot; Paxton, Bill, 2017, ApJ, 834L, 9B

"Carbon Shell or Core Ignitions in White Dwarfs Accreting from Helium Stars," **Brooks, Jared**; Bildsten, Lars; Schwab, Josiah; Paxton, Bill, 2016, ApJ, 821, 28B

"AM Canum Venaticorum Progenitors with Helium Star Donors and the Resultant Explosions," **Brooks, Jared**; Bildsten, Lars; Marchant, Pablo; Paxton, Bill, 2015, ApJ, 807, 74B

"Hydrogen Burning on Accreting White Dwarfs: Stability, Recurrent Novae, and the Post-nova Supersoft Phase," Wolf, William M.; Bildsten, Lars; **Brooks, Jared**; Paxton, Bill, 2013, ApJ, 777, 136W

Abstract

Explosive Outcomes from Rapid Accretion of Helium onto White Dwarfs in Tight Binaries

by

Jared C. Brooks

Accretion of helium onto white dwarfs at various rates can lead to several different types of explosive outcomes. Slow accretion from low mass He stars or He WDs in binaries with orbital periods less than an hour can build up helium shells of $\approx 0.1 M_{\odot}$ that ignite and detonate, generating faint and fast transients. In this dissertation, I explore this well known channel for generating transients from He accretion onto WDs, as well as with less explored channels that accrete He onto WD at rates that allow for steady helium shell burning. Stable helium burning significantly grows the degenerate core, which can result in several different outcomes, including type Ia supernovae and accretion induced collapse. I also explore deep convection in C/O/Ne hybrid WDs and found effective mixing to a level that will strongly affect their later explosions. Some binaries are unstable to mass transfer and merge the component stars. Previous studies explored explosive outcomes during the merger, whereas I studied a channel that leads to a unique type of explosion $\approx 10^5$ years after the merger event. Additionally, I made some predictions about observed compact binaries with He stars and He WDs.

Contents

Chapter 1

Introduction

Most stars are in binary systems (Jaschek & Gómez, 1970), and many of those stars orbit each other close enough to exchange mass during certain evolutionary stages (Paczyski, 1971). The stripping of the outer layers from these stars via their binary interactions throughout their lives can remove significant angular momentum, resulting in extremely short orbital periods ($P_{\rm orb} \approx$ minutes to days), and reveal the compact remnant cores of the component stars (Iben & Tutukov, 1991). Subsequent mass transfer between the two remnants can lead to bright transients such as mergers, novae, and supernovae (Wang et al., 2009; Woosley & Kasen, 2011; Piersanti et al., 2014; Shen, 2015), powered by a sudden turn-on of thermonuclear burning in extremely dense matter (Shen & Bildsten, 2007; Ruiter et al., 2012; Shen & Moore, 2014). The observational clues from such transients help us to understand stellar evolution, formation rates of different types of systems, and the evolution and fate of the cosmos (Howell, 2011).

1.1 Formation Scenarios

Stars spend most of their lives on the main sequence, burning hydrogen to helium in their cores. When stars run out of fuel in the cores, they transition into shell burning and expand into giant configurations. For stars in close binaries, this giant configuration can be larger than the star's Roche lobe (RL, Eggleton, 1983), which is a tear-drop shaped volume bounded by a critical gravitational equipotential in the co-rotating frame. When stars overflow their RLs, they begin to donate mass to their binary companion through the inner Lagrange point, L1. If the mass ratio $q > 2/3$, where $q = M_2/M_1$ and M_2 is the mass of the donor star (Marsh et al., 2004), or if the donor star has a deep convective envelope (Iben & Tutukov, 1991), the mass transfer is unstable and leads to a commom envelope (CE) event, where the gravitational potential energy between the two stars is exchanged for the binding energy of the donor's envelope, causing the donor to eject its outer layers from the system, extracting angular momentum from the binary, and resulting in a much shorter orbital period.

For the He star-WD systems relevant for this dissertation, the initially more massive star will burn its core to helium and then subsequently to carbon and oxygen (C/O), or to oxygen and neon (O/Ne) for a sufficiently massive progenitor, before expanding into its RL. RL overflow (RLOF) then begins on the asymptotic giant branch (AGB), and due to the AGB star's deeply convective envelope, rapidly developes into a CE, resulting in a tight orbit with a C/O or O/Ne WD and the companion star still on the main sequence. When the companion star evolves off its main sequence, it develops H-shell burning as the star ascends the red giant branch (RGB) and begins RLOF before He core burning can begin. Due to the fact that these stars mainly experience RLOF after core burning stages, there is a unique initial-final mass relation, as shown in Figure 1.1, where I compare values obtained from Modules for Experiments in Stellar Astrophysics

(MESA, see Paxton et al., 2011, 2013; Paxton et al., 2015), against those in Dominguez et al. (1999).

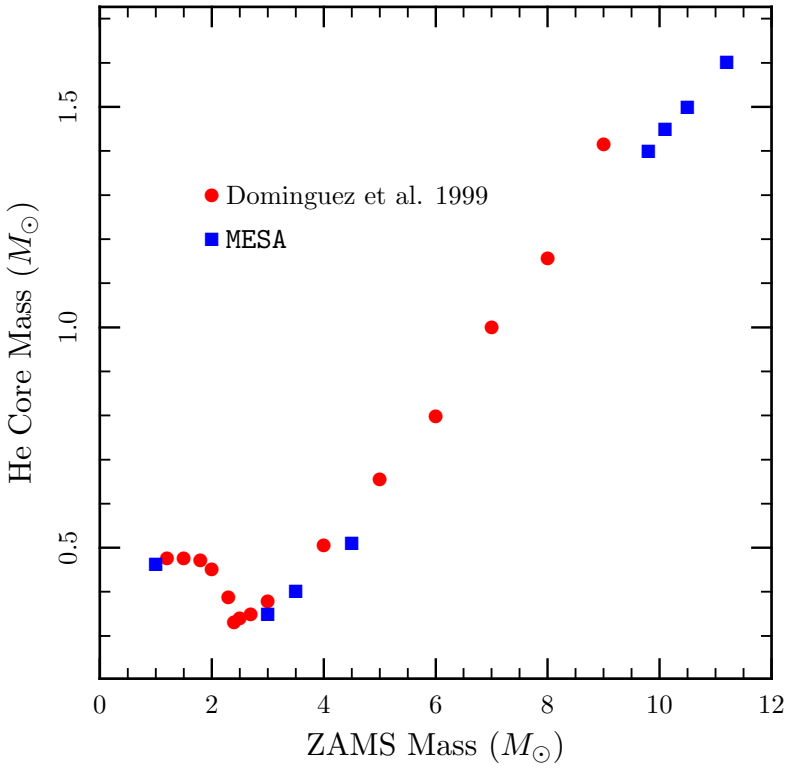

Figure 1.1 The relation between the total initial star mass and the He core mass at the moment of core He ignition. I compare models from Dominguez et al. (1999) in Table 4 (corresponding to $Z = Z_\odot$) shown by red circles, to the models made using MESA, shown by the blue squares. The lower mass points are from models prepared for Chapter 2 (MESA version 5118) and the higher mass points are from models prepared for Chapter 3 (MESA version 7624).

After the second common envelope event, the initially less massive star is stripped of its H envelope, leaving a naked He star in a short orbital period binary ($\approx$ minutes to days) with a C/O or O/Ne WD. There are other evolutionary scenarios that can lead

to short orbital period He star-WD binaries that involve episodes of convervative and non-conservative mass transfer (meaning matter is retained in or ejected from the binary system, respectively), but the scenario given above is the most common one (Wang et al., 2009).

1.2 Dominant Evolutionary Mechanisms

The focus of this dissertation is to study the episodic burning and explosions in and on WDs due to He accretion from a companion via RLOF at various rates. This section describes the dominant mechanisms that control the evolution of these common but enigmatic binary stellar remnants. In the following section I outline the various regimes of helium accretion studied in this dissertation, roughly in order of increasing accretion rates.

I briefly review some of the key physical ideas needed to understand the subsequent evolution of these systems. These include various sources of angular momentum loss, Roche lobe physics, the thin-shell instability, and the lack of hydrogen. Since these systems already start with low angular momentum, mechanisms that extract further angular momentum from the system, including gravitational wave radiation (GWR, Landau & Lifshitz, 1975), system mass loss, which can extract extra angular momentum via dynamical friction (similar to CE events, see Pejcha et al., 2016), and spin-orbit interaction (Marsh et al., 2004), strongly affect the evolution. The Roche lobe physics is closely related to angular mometum losses. If a star begins RLOF due to GWR shrinking the RL to the size of the stellar radius, the resulting mass transfer can proceed slowly enough for convervative mass transfer. Whereas if the star begins RLOF due to shell burning in the donor causing the radius to rapidly expand past its RL, the mass transfer rates can quickly rise above the Eddington accretion rate for the accretor, leading to non-

conservative mass transfer. Since the accretors are degenerate WDs, the accretion onto them and the eventual nuclear burning in a geometrically thin shell is unstable to the thin shell instability (Schwarzschild & Härm, 1965). This can lead to novae and high-velocity ejections of mass from the system. On the other hand, at high enough accretion rates the burning shell stays hot enough to keep the burning layer sufficiently geometrically thick such that the thermal structure can adjust quickly enough in response to nuclear burning and allow steady burning of accreted material at the accretion rate (see 3.1.1, also Paczynski & Zytkow, 1978). The lack of H in these systems is interesting because H burns at much lower temperature and densities than He. This means that for He accretion onto WDs, at slow rates, the mass of the shell required for ignition is a few orders of magnitude greater, and at higher rates, the accretion rates required for steady burning are an order of magnitude greater (see Figure 1.2).

1.3 Regimes of Helium Accretion

All the different regimes of He accretion onto WDs discussed above are explored in this dissertation. I start in Chapter 2 with low mass ($\lesssim 0.5 M_\odot$) He core burning stars in orbital periods short enough that GWR could bring the stars close enough that the He star begins RLOF while still core He burning ($P_{\rm orb} \lesssim 2$ hours). This leads to steady mass transfer at $\approx 3 \times 10^{-8} M_\odot$/yr starting at orbital periods of $\approx 20 - 25$ minutes (see the dashed curve in Figure 1.2 labeled "sdB Donor", Savonije et al., 1986; Tutukov & Fedorova, 1989; Tutukov & Yungelson, 1990; Iben & Tutukov, 1991; Yungelson, 2008; Piersanti et al., 2014), which is slow enough to build up cold helium layers on the surface of the accreting WD until they unstably ignite, leading to He novae, and possibly ".Ia" SNe (Bildsten et al., 2007a). He WDs, on the other hand, will make contact at much shorter orbital periods (>10 minutes) due to their compact configurations, and begin

donating He rich matter at a few $\times 10^{-6} M_{\odot}$/yr, leading to steady He burning on the accreting WD (as shown by the dot-dashed curve in Figure 1.2 labeled 'He WD Donor', also see §6.3 for discussion). As the orbital period begins to increase, the mass transfer rates decrease below the steady He burning boundary, leading to mild oscillations in He burning. The last He novae will only reach conditions for detonation in the most massive WDs ($\gtrsim 1.2 M_{\odot}$, see §2.4 for discussion), whereas most systems with He WD donors will never be able to produce detonations (Shen & Bildsten, 2009).

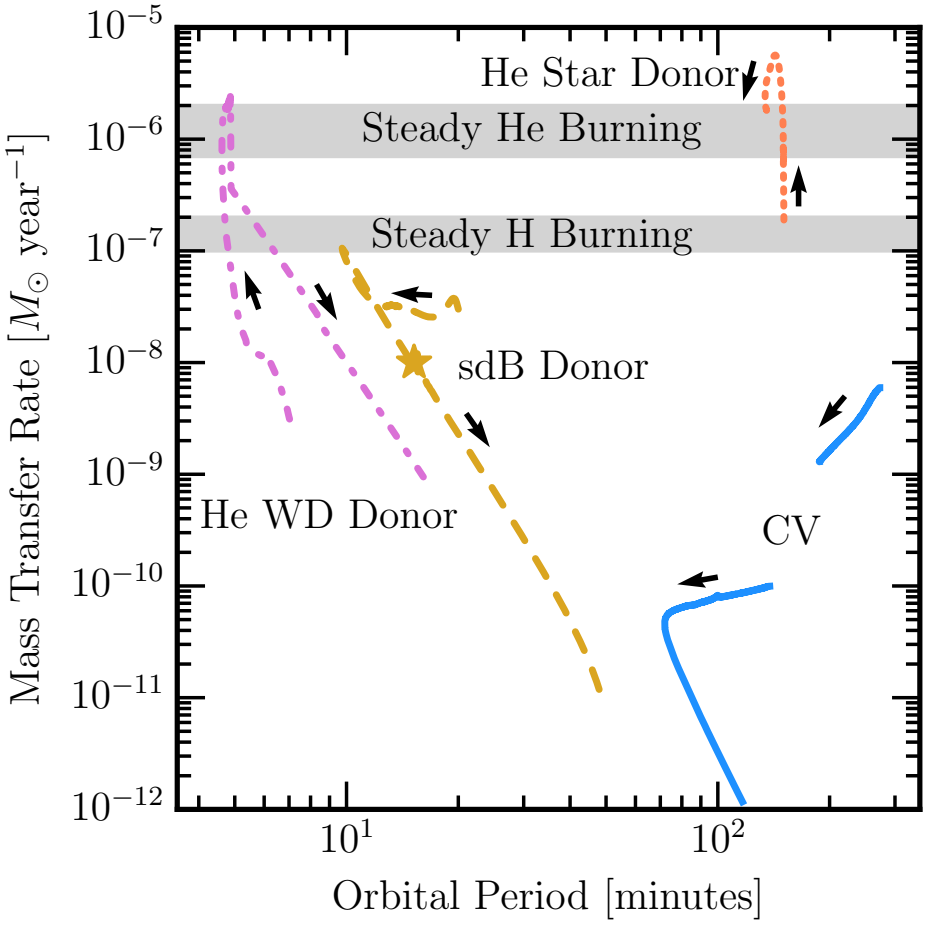

Figure 1.2 Accretion histories with arrows showing the evolution direction. The sdB case is a $0.4M_\odot$ sdB star undergoing core He burning and donating to a $0.6M_\odot$ WD. The He WD case is a $0.175M_\odot$ He WD that initiates mass transfer onto a $0.8M_\odot$ WD. The He star donor case consists of a $1.0M_\odot$ WD accreting from a $1.5M_\odot$ He star as it expands after core He exhaustion. The CV started with a $1.0M_\odot$ WD in a binary with a $0.6M_\odot$ MS star. The regions of stable H and He burning are shown for a $0.8M_\odot$ WD.

For systems with longer orbital periods (∼hours to days) and higher mass He stars, GWR is insufficient to bring the binary close enough for RLOF to occur during He core burning, but the He shell burning that follows is powerful enough to expand the envelope into a red giant configuration, rapidly pushing the radius past the RL. This leads to

mass transfer at rates of $\approx 10^{-6} - 10^{-5} M_{\odot}$/yr, which coincides with the accretion rates for steady helium burning (see Figures 1.2 and 3.3, also Yoon & Langer, 2003; Piersanti et al., 2014).

Cataclysmic Variable (CV) stars, on the other hand, which accrete solar material (i.e. hydrogen-dominate) from a low mass main sequence companion, experience much slower mass transfer rates at similar orbital periods (Robinson, 1976). A typical case is shown in Figure 1.2 by the solid blue curves.

Steady He burning on the surface of C/O WDs can lead to three different outcomes: for sufficiently massive C/O WDs, the steady He shell burning can build up the C/O core mass to $M_{\rm Ch}$ triggering runaway carbon burning in the core (Single Degenerate Channel for SNe Ia, see Maoz et al., 2014); if either the C/O WD or the He star donor is too low mass to build up the accretor mass to $M_{\rm Ch}$, after the He star donates all of its remaining He it contracts back inside its RL to become a cooling WD, and the two C/O WDs slowly spiral in via GWR and eventually merge and possibly detonate (Double Degenerate Channel for SNe Ia, see §3.5, also Ruiter et al., 2012; Moll & Woosley, 2013; Dan et al., 2014; Sato et al., 2015). If both the He star and C/O WD are massive enough, the hot C/O ashes from the He shell burning ignites before the core, leading to a thin carbon flame that propagates to the center, converting the entire C/O WD to O/Ne (see §3.2, also Nomoto & Iben, 1985; Saio & Nomoto, 1985; Schwab et al., 2016). Those systems will lead to an accretion induced collapse (AIC) instead of an explosion resembling a SNe Ia. Similarly, systems that start with a massive O/Ne WD as the accretor will lead to AIC (see Chapter 5).

I also study hybrid C/O/Ne WDs, which have C/O cores ($0.2 - 0.4 M_{\odot}$) with O/Ne mantles. A C flame from steady He burning on this type of hybrid WD would quench open reaching the C/O mantle, leaving the small C/O core unburned. Further growth of the degenerate core could then lead to a peculiar SNe Ia (Denissenkov et al., 2013, 2015;

Kromer et al., 2015; Willcox et al., 2016; Bravo et al., 2016). I found, however, that the interface between the C/O core and O/Ne is unstable to convective mixing on timescales short enough that they should be nearly fully mixed before He accretion even starts. A carbon flame ignited in such a model has the potential to propagate to the center (Lecoanet et al., 2016), leading to the same fate as systems with C/O WD accretors that ignite shell C flames: eventual AIC. For these systems, the He star is still shell burning and donating He, and the accretor is now a NS. These He star-NS binaries have properties consistent with ultraluminous X-ray sources (ULXs, see King et al., 2017), and will eventually become an intermediate mass binary pulsar (IMBP), or will merge and spin up to become a millisecond pulsar (MSP) (see §6.1).

All of the systems discussed above lose mass at some point in their evolution, and I have made certain assumptions about the amount of angular momentum that mass takes with it. If I have underestimated the amount of angular momentum loss, some of the systems I thought stable may in fact be unstable to mergers. Furthermore, systems with He WD donors may merge on contact due to weak spin-orbit coupling during the direct impact accretion phase, where the accretion stream hits the accretor instead of forming a disk first (Marsh et al., 2004; Brown et al., 2016), or due to dynamical friction within the expanding ejected shell from a H nova (Shen, 2015). Merger remnants from these sorts of systems have the He burning shell fed from an extended He envelope instead of a disk regulated by an accretion stream. Therefore, systems with sufficiently massive C/O cores and He envelopes will be converted to O/Ne cores by C flames, as described above and in §3.2. If the merger remnant is super-Chandrasekhar, then an AIC will occur inside the extended He envelope, leading to a shock that propagates outwards through envelope and produces a rapidly evolving and luminous transient.

1.4 Common Acronyms in this Dissertation

- AIC: Accretion Induced Collapse
- AGB: Asymptotic Giant Branch
- AM CVn: AM Canum Venaticorum
- CE: Common Envelope
- C/O: Carbon/Oxygen
- GWR: Gravitational Wave Radiation
- H: Hydrogen
- He: Helium
- $M_{\rm Ch}$: Chandrasekhar Mass
- MSP: Millisecond Pulsar
- NS: Neutron Star
- RGB: Red Giant Branch
- RL: Roche lobe
- RLOF: Roche lobe overflow
- O/Ne: Oxygen/Neon
- $P_{\rm orb}$: Orbital Period
- sdO/B: sub-dwarf O/B

- SN: Supernova
- ULX: Ultraluminous X-ray source
- WD: White Dwarf

1.5 Permissions and Attributions

1. The content of chapter 2 is adapted and reproduced from Brooks et al. (2015) with the permission of The Astrophysical Journal.
2. The content of chapter 3 is adapted and reproduced from Brooks et al. (2016) with the permission of The Astrophysical Journal.
3. The content of chapter 4 is adapted and reproduced from Brooks et al. (2017c) with the permission of The Astrophysical Journal Letters.
4. The content of chapter 5 is adapted and reproduced from Brooks et al. (2017b) with the permission of The Astrophysical Journal.
5. The content of chapter 6 is adapted and reproduced from Brooks et al. (2017a) and Kupfer et al. (2017) with the permission of The Astrophysical Journal.

Chapter 2

AM Canum Venaticorum Progenitors with Helium Star Donors and the Resultant Explosions

In this chapter, we explore the outcome of mass transfer via Roche lobe overflow (RLOF) of $M_{\rm He} \lesssim 0.51 M_\odot$ pure helium burning stars in close binaries with white dwarfs (WDs). The evolution is driven by the loss of angular momentum through gravitational wave radiation (GWR), and both stars are modeled using Modules for Experiments in Stellar Astrophysics (`MESA`). The donors have masses of $M_{\rm He} = 0.35, 0.4, \& \ 0.51 M_\odot$ and accrete onto WDs of mass $M_{\rm WD}$ from $0.6 M_\odot$ to $1.26 M_\odot$. The initial orbital periods ($P_{\rm orb}$) span 20 to 80 minutes. For all cases, the accretion rate onto the WD is below the stable helium burning range, leading to accumulation of helium followed by unstable ignition. The mass of the convective core in the donors is small enough so that the WD accretes enough helium-rich matter to undergo a thermonuclear runaway in the helium shell before

any carbon-oxygen enriched matter is transferred. The mass of the accumulated helium shell depends on $M_{\rm WD}$ and the accretion rate. We show that for $M_{\rm He} \gtrsim 0.4 M_{\odot}$ and $M_{\rm WD} \gtrsim 0.8 M_{\odot}$, the first flash is likely vigorous enough to trigger a detonation in the helium layer. These thermonuclear runaways may be observed as either faint and fast .Ia SNe, or, if the carbon in the core is also detonated, Type Ia SNe. Those that survive the first flash and eject mass will have a temporary increase in orbital separation, but GWR drives the donor back into contact, resuming mass transfer and triggering several subsequent weaker flashes.

2.1 Introduction

Core burning helium stars in semi-detached close binaries with WDs are one of the progenitor classes of AM Canum Venaticorum (AM CVn) stars, along with donors that are helium WDs and evolved main sequence stars. They are part of a larger class of binary stars called cataclysmic variables, but are further defined by their short orbital periods (5-80 minutes) and a complete absence of hydrogen. Their importance stems from common envelope stages during their formation, their detectability as gravitational wave sources, and their roles as possible projenitors for helium novae, SNe .Ia, and even SNe Ia (Nomoto, 1982b,a; Iben & Tutukov, 1991; Woosley & Weaver, 1994; Bildsten et al., 2007a; Deloye et al., 2007; Yungelson, 2008; Kato et al., 2008; Shen & Bildsten, 2009; Wang et al., 2009; Ruiter et al., 2009; Stroeer & Nelemans, 2009; Woosley & Kasen, 2011; Townsley et al., 2012; Piersanti et al., 2014; Ruiter et al., 2014; Shen & Bildsten, 2014).

One route by which He star + WD binaries are formed is realized/encountered when the initial binary configuration leads to so-called case CB mass transfer: the primary fills its Roche lobe during its AGB phase (C-type), and after a common envelope phase,

the secondary fills its Roche lobe during its RGB phase (B-type) (Iben & Tutukov, 1994a). The two common envelope phases release a large fraction of the initial angular momentum, leaving a helium star in a short orbital period with a WD. The binary is then driven closer together due to angular momentum loss via GWR until the helium star fills its Roche lobe and begins donating helium to the WD. Longer initial orbital periods lead to helium stars that complete their burning before making contact.

When the WD has accumulated enough accreted helium, a thermonuclear runaway begins in the helium shell. At this point, the WD will likely eject all the mass above the burning layer (Iben & Tutukov, 1991). Depending on the mass of the WD and of the accreted helium shell (and of the fraction of metals in the accreted material) the helium shell burning may result in a deflagration or detonation (Livne, 1990; Limongi & Tornambe, 1991; Livne & Glasner, 1991; Woosley & Weaver, 1994; Bildsten et al., 2007a; Shen & Bildsten, 2009; Woosley & Kasen, 2011; Moore et al., 2013; Shen & Moore, 2014; Shen & Bildsten, 2014). Helium detonations certainly unbind the shell and lead to fast and faint .Ia SNe. They may also trigger a carbon detonation in the core, which causes a Type Ia SN (Livne, 1990; Livne & Glasner, 1991; Arnett & Livne, 1994; Livne & Arnett, 1995; Fink et al., 2007, 2010; Sim et al., 2010; Kromer et al., 2010; Woosley & Kasen, 2011; Sim et al., 2012; Moll & Woosley, 2013; Shen & Bildsten, 2014).

The goal of our work is to use a realistic mass transfer model to calculate the He shell masses at ignition and assess the likelihood of their detonations. The mass loss from these events, which, given survival of the accretor, occur multiple times for each system, increases the orbital separation (at these low mass ratios), causing the stars to temporarily lose contact, until GWR drives them together again. Therefore, while the initial combined mass of the two compact stars may exceed the Chandrasekhar limit, this channel will not result in a near Chandrasekhar mass WD.

In §2.2 we describe the creation and subsequent simulation of the helium star models, compare the secular evolution results to those of previous studies, and explain the donor stars' response to mass loss during different stages. Then in §2.3 we include the behavior of the accreting WD and the conditions leading to the first thermonuclear runaway in order to determine the strength of the flash and the likelihood of a detonation occurring. As a case study, we simulated the binary system CD-30° 11223 (Geier et al., 2013) up to the first flash. Additionally, we follow through with the simulations assuming the first flash does not unbind the accreting WD, and calculate the effect of mass loss from ejection events on the binary parameters in §2.4, and follow up with conclusions and discussion in §2.5.

2.2 Donor Evolution and Mass Transfer Rates

These types of binary systems are formed when two comparable mass stars, with mass ratio less than 2, are born in a close binary. The more massive (primary) star will leave the MS and evolve through the RGB and AGB phases, donating some of its mass to its less massive companion. The primary star then becomes a WD, while the secondary, now the more massive of the two, accelerates through its MS evolution. Once the secondary leaves the MS and expands as it rises up the RGB, it overflows its RL and begins unstable mass transfer. The resulting common envelope removes the secondary's hydrogen envelope, revealing a low mass helium star. This happens soon enough that the WD's core is still hot ($\log(T_c/\mathrm{K}) > 7.2$) at an age of ≈200 Myr. The two stars are then close enough for GWR to drive them into contact before exhaustion of helium in the secondary's core as long as $P_{\mathrm{orb}} \lesssim 2$ hours after the final common envelope (Tutukov & Fedorova, 1989; Tutukov & Yungelson, 1990; Iben & Tutukov, 1991, 1994a; Yungelson, 2008).

Our 0.35 $M_\odot$ helium star model is created by evolving a 3.0 $M_\odot$ ZAMS star with solar metallicity, using a mixing length of twice the pressure scale height ($\alpha_{ml} = 2H$) and the Schwarzschild criterion with no convective overshooting, through the main sequence and into hydrogen shell burning until the mass fraction of hydrogen at mass coordinate $M_r = 0.35\ M_\odot$ has dropped below 10^{-6}. We then artificially remove mass from the surface until the mass is 0.35 $M_\odot$. The star is left to adjust to the mass loss until core helium burning luminosity reaches 1 $L_\odot$. The 0.4 $M_\odot$ helium star is created the same way starting with a 3.5 $M_\odot$ ZAMS star. We also created a 0.51 $M_\odot$ sdB star by evolving a 1 $M_\odot$ ZAMS star up to the helium core flash, at which point we turn on a very strong RGB wind until the mass drops to 0.51 $M_\odot$. The core flash then proceeds to stable core He burning.

We set "`tau_factor=100`", which puts the outer cell of the model at an optical depth of $\tau = (2/3) \times$ `tau_factor`. This setting omits the HeII ionization zone and leads to a thin surface convection zone and gives a $T_{\rm eff}$ consistent with sdB star observations. Setting a `tau_factor=1` leads to a deep surface convection zone, and initial mass transfer rates experience a runaway and encounter numerical problems. We leave this issue for future studies.

2.2.1 Mass Transfer Rates

The binary interactions are first computed, using `MESA` (Paxton et al., 2011, 2013) version 5118, by adding a point-mass companion, i.e. the evolution of the companion star is not computed during this calculation. We assume no rotation or magnetic braking, and conservative mass transfer. The only factors that affect the binary separation, a, are mass transfer and loss of angular momentum via GWR. To compute mass transfer rates, we used the "Ritter" implicit scheme of `MESA` (Paxton et al. 2015 in preparation), which

Table 2.1. Comparison to previous work by Yungelson

$\frac{M_{\rm He}}{M_\odot}$	$\frac{M_{\rm WD}}{M_\odot}$	$\frac{P_{\rm orb,0}}{\rm min}$	$\underline{t_c\ (\rm Myr)}$		$\underline{P_c\ (\rm min)}$		$\underline{Y_c}$	
			Yungelson	MESA	Yungelson	MESA	Yungelson	MESA
0.35	0.5	20	1.29	1.4	15.96	15.7	0.977	0.974
0.35	0.5	40	15.99	17.4	16.24	16.1	0.936	0.923
0.35	0.5	60	50.80	51.1	17.02	16.9	0.871	0.833
0.4	0.8	40	9.14	9.2	20.61	21.2	0.933	0.925
0.4	0.8	60	30.21	30.4	21.67	22.0	0.854	0.824
0.4	0.8	80	66.95	67.4	22.85	24.1	0.751	0.637

Note. — $M_{\rm He}$ and $M_{\rm WD}$ are the initial masses of the donor and the accretor, $P_{\rm orb,0}$ is the initial orbital period, t_c is the time before the donor fills its Roche lobe, P_c is the orbital period at time of contact, and Y_c is the central Helium mass fraction at the time of contact.

implicitly computes the prescription given by Ritter (1988).

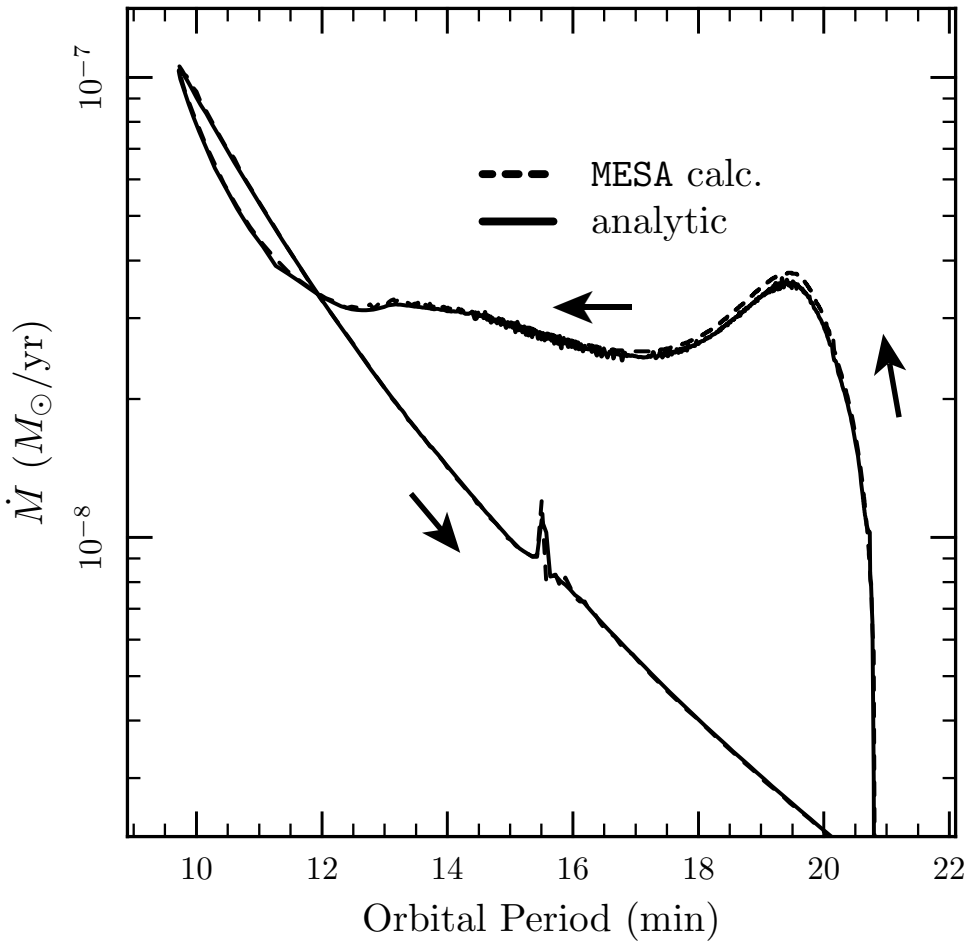

Figure 2.1 Comparison of $\dot{M}$ calculated by `MESA`'s root-finding algorithm (solid line) and using equations (2.1) and (2.2) given by component masses and $R_{\rm He}$ given in `MESA` output (dashed line). Arrows show the direction of evolution. From the case with $M_{\rm He} = 0.4M_\odot$, $M_{\rm WD} = 0.6M_\odot$ at $P_{\rm orb,0} = 40$ minutes.

The resulting mass transfer rate, $\dot{M}_{\rm He}$, matches what we would expect from the relation of mass and angular momentum loss rates,

$$\frac{\dot{M}_{\rm He}}{M_{\rm He}}\left(\frac{n}{2}+\frac{5}{6}-\frac{M_{\rm He}}{M_{\rm WD}}\right) = \left.\frac{\dot{J}}{J}\right|_{GWR} \quad , \tag{2.1}$$

where $M_{\rm He}$ and $M_{\rm WD}$ are the masses of the helium star and WD, respectively, and $n = d\ln R_{\rm He}/d\ln M_{\rm He}$ (Paczyński, 1967; Nelemans et al., 2001). Angular momentum loss

via GWR is given by Landau & Lifshitz (1975) as

$$\left.\frac{\dot{J}}{J}\right|_{GWR} = -\frac{32}{5}\frac{G^3}{c^5}\frac{M_{\rm He}M_{\rm WD}(M_{\rm He}+M_{\rm WD})}{a^4} \quad . \tag{2.2}$$

Figure 2.1 shows the $\dot{M}$ computed by `MESA` and the $\dot{M}$ calculated by equations (2.1) and (2.2) against $P_{\rm orb}$ given component masses and $R_{\rm He}$ (for the derivative n) reported in `MESA` output for a case with $M_{\rm He} = 0.4M_\odot$, $M_{\rm WD} = 0.6M_\odot$ at $P_{\rm orb,0} = 40$ minutes. The derivative $n = d\ln R_{\rm He}/d\ln M_{\rm He}$ was smoothed in certain regions using a raised cosine window because of numerical noise. The donor first starts RLOF at $P_{\rm orb} \approx 21$ minutes and $\dot{M}$ quickly rises to $\approx 3\times10^{-8}M_\odot$/yr, follows the arrows to a period minimum at 10 minutes, and then expands to larger $P_{\rm orb}$ with a declining $\dot{M}$. The glitch at ≈15.5 minutes results from the exposure of the once convective helium burning core.

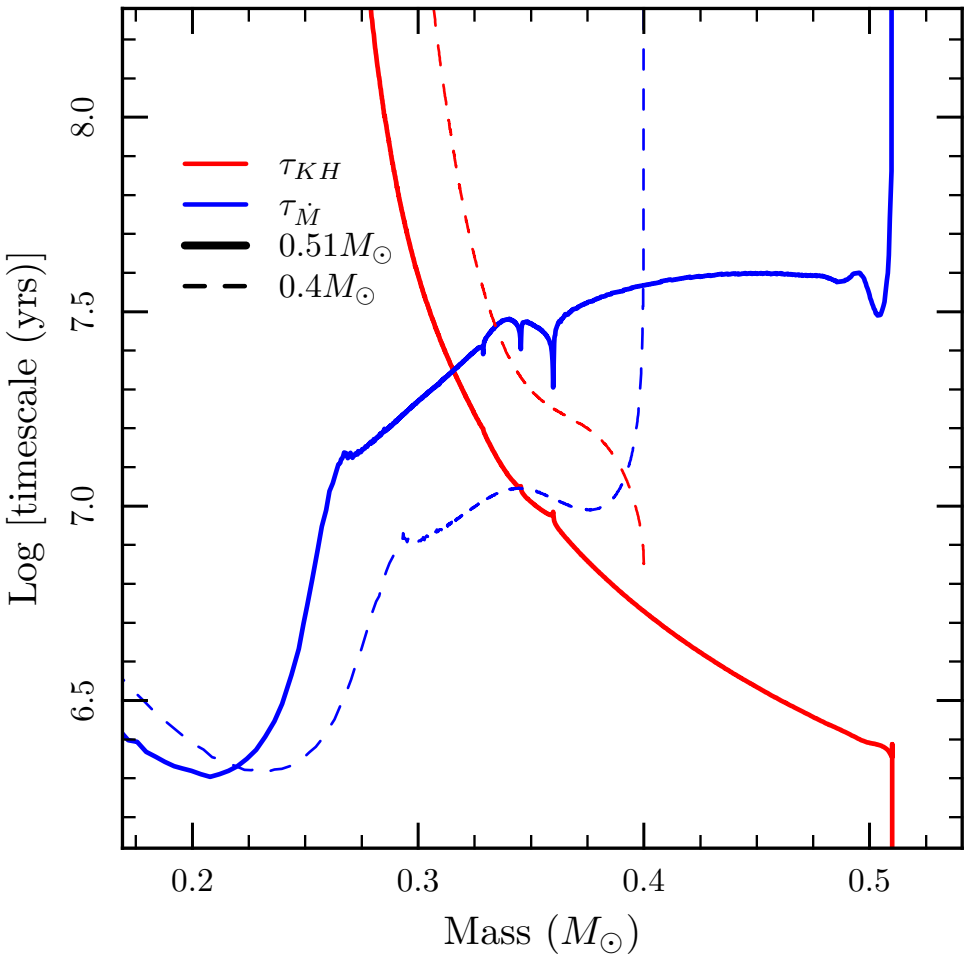

Figure 2.2 The two models shown here are the 0.51 $M_\odot$ and the 0.4 $M_\odot$ donors. The two timescales for each model are the thermal and the mass loss timescales. At the beginning of the mass transfer phase, the thermal timescale is much shorter than the mass loss timescale, so the donor star adjusts its thermal structure in response to mass loss. As mass transfer rates rise and core luminosity falls, the timescales become comparable, and the donor responds adiabatically to mass loss, causing thermal timescales to rise and mass loss timescales to fall even faster.

In addition to checking $\dot{M}$ histories from `MESA` against equations (2.1) and (2.2), we also compare our results to the work of Yungelson (2008). Shown in Table 2.1 are the age, $P_{\rm orb}$, and the core mass fraction of helium at the time of contact for six cases. We agree with this prior work. For a final comparison to Yungelson's results, we plotted

the evolution of the thermal ($\tau_{\rm KH} = GM^2/RL$) and angular momentum loss ($\tau_{\rm GW} = (J/\dot{J})|_{GWR}$) timescales for the case with initial parameters $M_{\rm He} = 0.35\ M_\odot$, $M_{\rm WD} = 0.5\ M_\odot$, and $P_{\rm orb,0} = 20$ min and found good agreement with the same plot shown in Figure 3(a) in Yungelson (2008).

2.2.2 Evolution of the Helium Star Donors

Figure 2.2 shows the evolution of the thermal and mass-loss ($\tau_{\dot{M}} = M/\dot{M}$, related to $\tau_{\rm GW}$ by equation 2.1) timescales for two cases with initial parameters ($M_{\rm He}$, $M_{\rm WD}$, $P_{\rm orb,0}$) = (0.51 $M_\odot$, 0.76 $M_\odot$, 70.5 min), (0.4 $M_\odot$, 1.0 $M_\odot$, 40 min). Models with lower donor mass climb to higher $\dot{M}$ faster because they make contact at smaller orbital separations, which means that radii and luminosities decrease faster and $\tau_{\rm KH} \approx \tau_{\dot{\rm M}}$ happens sooner in the evolution. This timescale crossing happens almost immediately after mass transfer turn-on for the two smaller mass donors, while the model with initial mass $M_{\rm He} = 0.51$ $M_\odot$ has $\approx 0.2\ M_\odot$ removed before $\tau_{\rm KH} \approx \tau_{\dot{\rm M}}$.

As the nuclear burning luminosity starts to decrease due to mass loss, the core temperature slowly decreases, allowing core contraction to increase the central density, shown in Figure 2.3. The bump in $L_{\rm nuc}/L$ in the middle panel of Figure 2.4 is caused by the envelope's absorption of the nuclear burning luminosity due to mass-loss (Savonije et al., 1986; Yungelson, 2008), explained more in §2.4. After the bump in the top and middle panel of Figure 2.4, n begins to fall, which, as can be seen from equation (2.1), increases $\dot{M}$. At this point the star is being driven out of thermal equilibrium as $\tau_{\rm KH} \gg \tau_{\dot{\rm M}}$, so further mass loss causes the central density to decrease, hence the bend in the $\rho_c - T_c$ curves in Figure 2.3 (Savonije et al., 1986; Deloye et al., 2007).

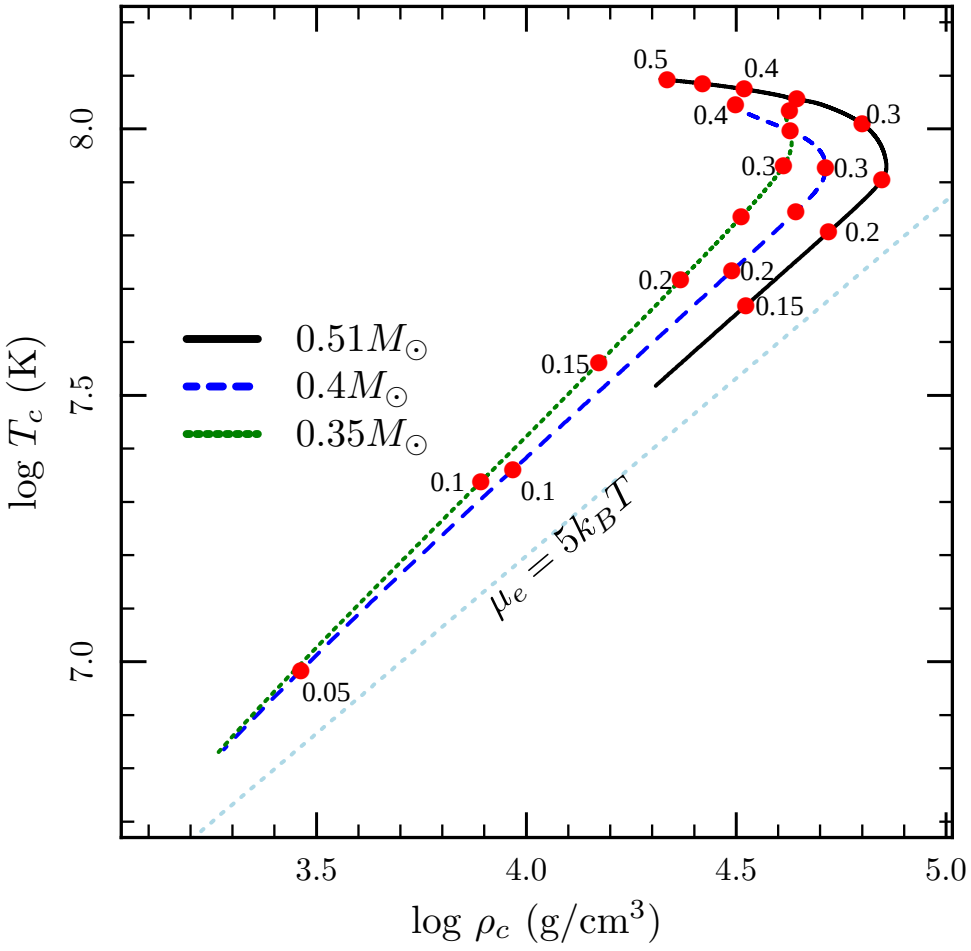

Figure 2.3 Evolutionary tracks of the central conditions in the donor stars. The $M_{\rm He} = 0.51\ M_\odot$ case has a $M_{\rm WD} = 0.76\ M_\odot$ companion with $P_{\rm orb,0} = 70.5$ min and donor core electron degeneracy parameter $\eta_c = 3.8$ (see end of sect. 2.2.2) when $M_{\rm He} = 0.2\ M_\odot$. The $M_{\rm He} = 0.4\ M_\odot$ case has a $M_{\rm WD} = 1.0\ M_\odot$ companion with $P_{\rm orb,0} = 40$ min and donor core electron degeneracy parameter $\eta_c = 3.1$ when $M_{\rm He} = 0.2\ M_\odot$. The $M_{\rm He} = 0.35\ M_\odot$ case has a $M_{\rm WD} = 1.0\ M_\odot$ companion with $P_{\rm orb,0} = 20$ min and donor core electron degeneracy parameter $\eta_c = 2.6$ when $M_{\rm He} = 0.2\ M_\odot$.

The increase in $\dot{M}$ continues until the period minimum is reached, where $n = d\ln R_{\rm He}/d\ln M_{\rm He} \approx 0.14$ for each model. The decreasing central temperature and density keep the star evolving along lines of nearly constant entropy where the cores are only mildly degenerate (Savonije et al., 1986; Deloye et al., 2007)). The core electron

degeneracy parameter, $\eta_c = \mu_{e,c}/k_B T_c$, that each of the three models considered here reach when their masses drop to 0.2 $M_\odot$ are ($M_{\rm He}$, η_c) = (0.51 $M_\odot$, 3.8), (0.4 $M_\odot$, 3.1), (0.35 $M_\odot$, 2.6). The fact that the donors are only mildly degenerate means that they will have higher mass transfer rates for a given $P_{\rm orb}$ than their fully degenerate counterparts during the AM CVn stage (Deloye et al., 2007).

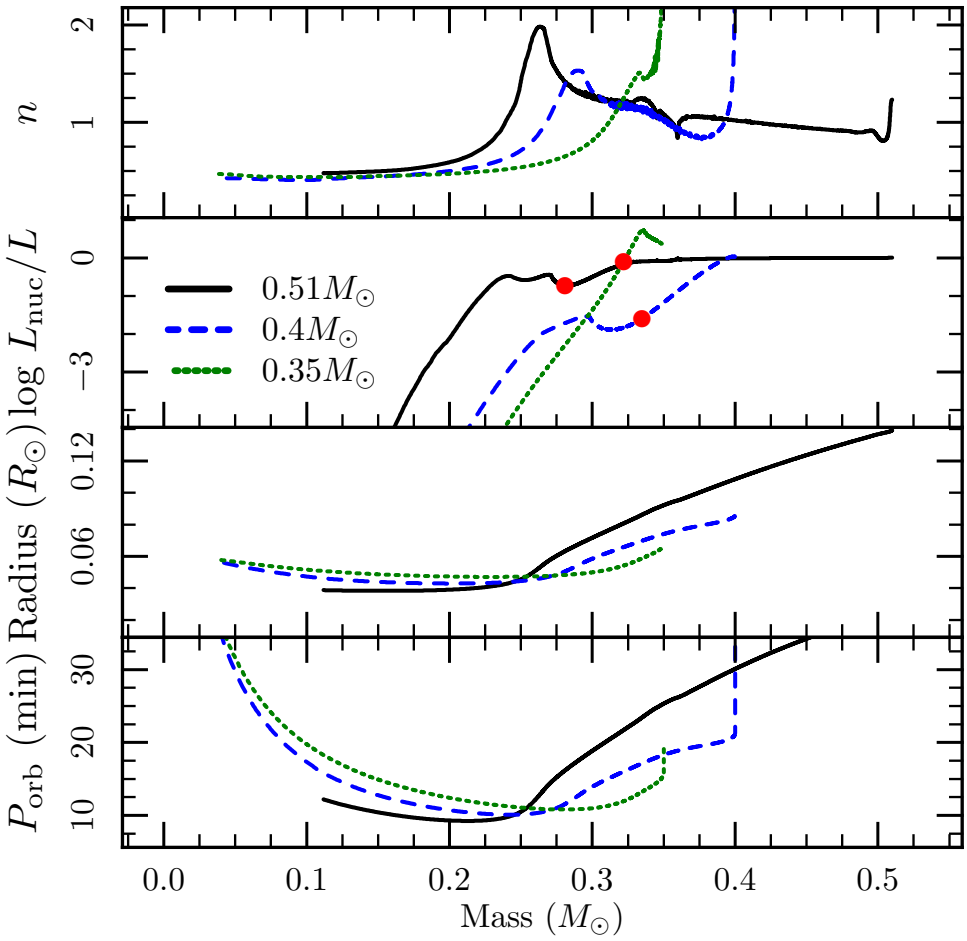

Figure 2.4 The models here are the same as plotted in Figures 2.3 and 2.2. The top section shows the derivative $n = d\ln R_{\rm He}/d\ln M_{\rm He}$, which was smoothed. The red circles in the middle panel mark when the core convection zone disappears. The mass at which the period minimum is reached for each model are ($M_{\rm initial}$, $M_{P_{\rm orb,min}}$) = (0.51 $M_\odot$, 0.21 $M_\odot$), (0.4 $M_\odot$, 0.24 $M_\odot$), and (0.3 $M_\odot$, 0.28 $M_\odot$), which corresponds to $n \approx 0.14$ for each case.

2.3 Accretion onto White Dwarfs and the First Flash

As mentioned above, enough helium is accreted onto the WD for a thermonuclear runaway to occur. A negligible amount of helium is burned before the runaway occurs, as the stable helium burning range for WDs of this mass is $10^{-6} M_{\odot}/\mathrm{yr} \lesssim \dot{M} \lesssim 3 \times 10^{-6} M_{\odot}/\mathrm{yr}$ (Piersanti et al., 2014; Brooks et al., 2016), a full order of magnitude larger than the accretion rates achieved by the cases in this study. The outcome may either be dynamical or hydrostatic, with the WD slowly expanding to fill its Roche lobe. Under the assumption that ejecta take the specific angular momentum of the accretor, mass loss causes the binary separation to increase, which temporarily shuts off mass transfer until GWR brings the component stars back into contact. We chose not to explore the possibility that dynamical friction within expanding envelope removes extra angular momentum (Shen, 2015). Below we show the results of "true" binary runs where both stars are evolved simultaneously, including the binary parameters, using `MESA` version 6596. The WD models were created

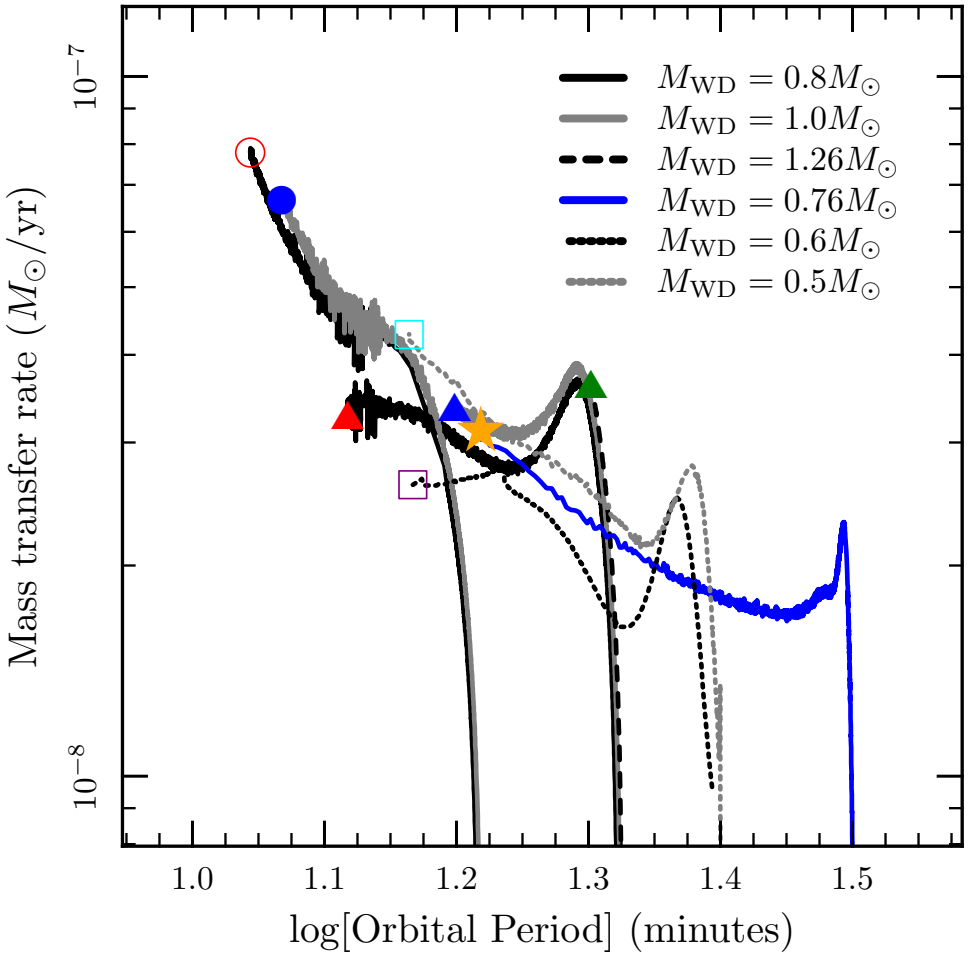

Figure 2.5 Black solid lines are systems with $M_{\rm WD} = 0.8M_\odot$, Grey solid lines are systems with $M_{\rm WD} = 1.0M_\odot$. The black dashed line is from a system with $M_{\rm WD} = 1.26M_\odot$. The black dotted line is from a system with $M_{\rm WD} = 0.6M_\odot$. The grey dotted line is from a system with $M_{\rm WD} = 0.5M_\odot$. The blue line is from the system modelling CD-30° 11223, see §2.3.2. The symbol marking the first flash correspond with those in Figure 2.7

in `MESA` by the same method described in Wolf et al. (2013). We age the WD models to 200 Myr, the relevant age for the 0.35 and 0.4 $M_\odot$ helium star donors. These WDs have core temperatures of a few$\times 10^7$K at the start of mass transfer. The WDs with sdB star companions could be even colder.

In this section we show results from cases with ($M_{\rm He}$, $M_{\rm WD}$) = ($0.35M_\odot$, $0.8M_\odot$),

$(0.35M_\odot, 1.0M_\odot)$, $(0.4M_\odot, 0.8M_\odot)$, $(0.4M_\odot, 1.0M_\odot)$, $(0.4M_\odot, 1.26M_\odot)$, $(0.46M_\odot, 0.5M_\odot)$, $(0.46M_\odot, 0.6M_\odot)$ all with initial orbital periods of $P_{\rm orb,0} = 40$ minutes, and a case with $(0.51M_\odot, 0.76M_\odot)$ and $P_{\rm orb,0} = 70.5$ to model the observed system CD-30° 11223.

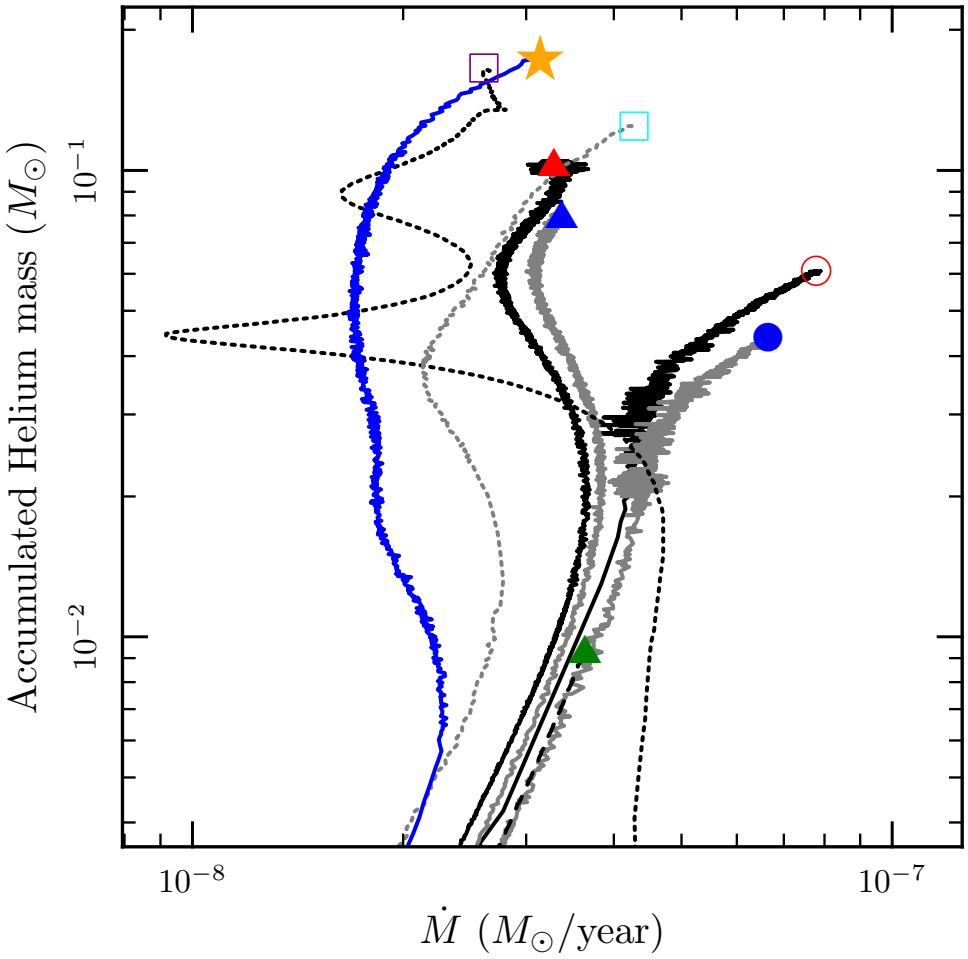

Figure 2.6 Accumulated helium shell mass for the first flash. Line Types, colors, and markers are the same as for Figure 2.5.

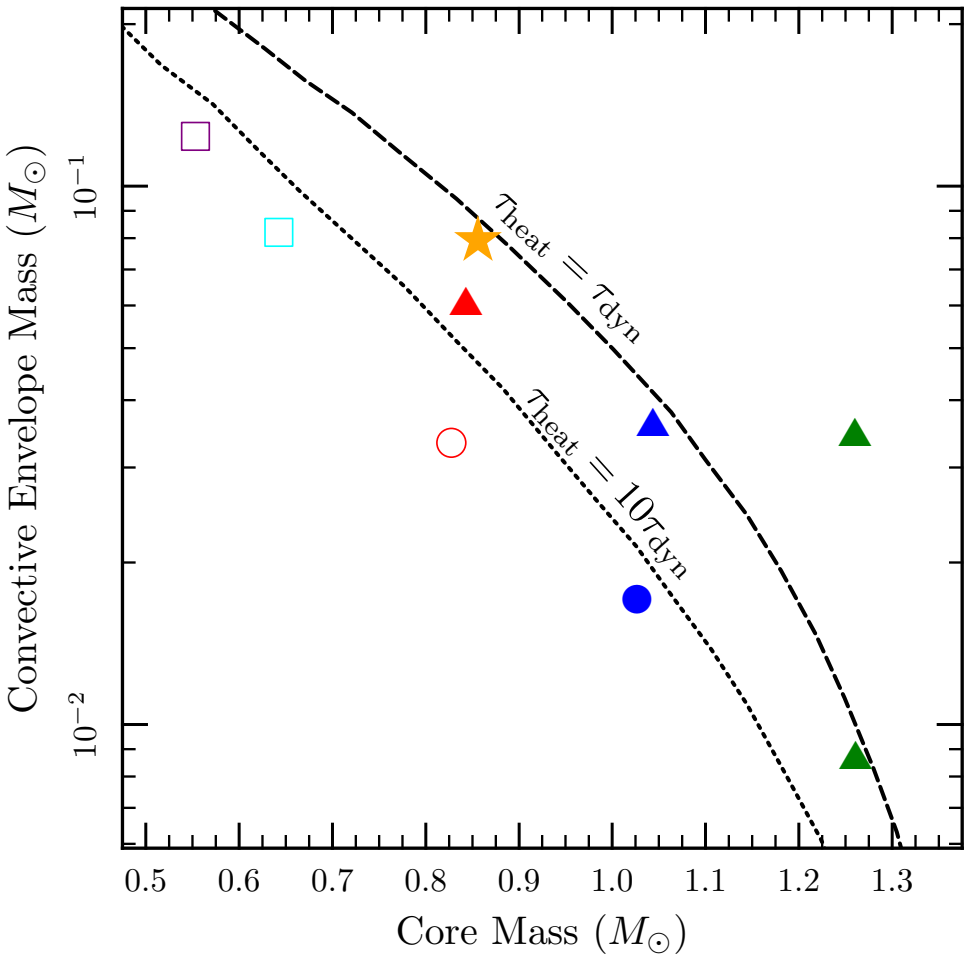

Figure 2.7 First burst from all "true" binary runs. Blue markers are from $1.0M_\odot$ WDs, red markers from $0.8M_\odot$ WDs, green from $1.26M_\odot$ WDs, purple from $0.5M_\odot$ WDs, and cyan from $0.6M_\odot$ WDs. Circles are from $0.35M_\odot$ donors, triangles from $0.4M_\odot$ donors, squares from $0.46M_\odot$ sdB star donors. Filled markers had $c_pT/\epsilon_{\rm nuc} < \pi r/C_{\rm sound}$. The orange star-shape is from the case study CD-30° 11223. The last (larger) burst on the $1.26M_\odot$ WD is included as a special case and is discussed in §2.4.

Our immediate goal is to calculate the thermal properties of the accumulating helium shell on the WD and find the shell mass at the time of the thermonuclear runaway. Most earlier work (see Figure 1 of Shen & Bildsten (2009)) assumed a constant accretion rate, whereas these binaries undergo a factor of about three change in $\dot{M}$ during the accumulation phase. Figure 2.5 shows the changing $\dot{M}$ as the orbital period shrinks for our distinct

cases. We terminate this plot at the moment of the first helium shell thermonuclear runaway. The resulting helium shell masses at the time of ignition (shown in Figure 2.6) are not that different than earlier works, but are now derived self-consistently. At these accretion rates, there is adequate time for thermal contact with the colder core, resulting in a temperature inversion in the helium shell and an ignition location above the base of the freshly accreted material. Hence, the convective shell masses will always be less than the accumulated masses and we do not concern ourselves with possible mixing during the burning into the underlying CO (or ONeMg) core. Piro (2015) recently discussed mixing during accumulation, which also looks unlikely at these lower accretion rates. Hence, we assume our shells have the abundance distribution of the material from the surface of the donor.

To calculate the nuclear burning rates we used `MESA`'s `co_burn` network, which includes alpha chain reactions up to ^{28}Si. The qualitative nature of all bursts are quite similar, so we study one typical case in detail in §2.3.1.

In Figure 2.7 we plot the core mass, which includes all the helium below the burning zone, against the convective envelope mass. The black lines, from Shen & Bildsten (2009), represent where the local heating timescale ($c_p T/\epsilon_{\rm nuc}$) equals the (dashed line) local dynamical time ($H/C_{\rm sound}$), and (dotted) $10\times$ the local dynamical time, included for uncertainty in detonation requirements. The filled markers met the condition that the burning timescale became shorter than the sound travel time across a hemisphere ($c_p T/\epsilon_{\rm nuc} < \pi r/C_{\rm sound}$), meaning that the burning was at least non-spherically symmetric.

2.3.1 Typical First Helium Thermonuclear Instability

The explosion studied here is the first from the case with $M_{\rm He} = 0.35 M_\odot$, $M_{\rm WD} = 1.0 M_\odot$ (filled blue circle in Figure 2.7). Because the compressional heat leaks both out of

the surface and into the core, the maximum temperature and burning zones are located within the helium shells, instead of the core-envelope boundary. This "off-center" ignition was also found to be prevalent at constant $\dot{M}$ (Nomoto, 1982b; Iben & Tutukov, 1991; Woosley & Kasen, 2011). The base of the helium shell (where helium mass fraction $Y < 0.05$), shown by the black markers in Figure 2.8, therefore, lies below the ignition location, and stays fairly degenerate.

The evolution of the instability proceeds most rapidly near the minimum local heating timescale ($\tau_{\rm heat} = c_p T/\epsilon_{\rm nuc}$). Shown in Figure 2.9, at the base of the convective envelope (coincident with the burning zone) the temperature increases and the pressure decreases by a factor of ≈2, and the carbon mass fraction (X_{12}) rises from 0.02 to 0.08. The heating timescale, $\tau_{\rm heat}$, reaches a minimum of ≈3.5 seconds, compared to a dynamical time ($\tau_{\rm dyn} = H/C_{\rm sound}$) of ≈0.2 seconds, and the sound travel time around a hemisphere, $\pi r/C_{\rm sound} \approx 6$ seconds. Convection extends almost all the way to the surface, and becomes fairly inefficient with convective speeds reaching ≈15% of the sound speed and eddy-turnover times ($\tau_{\rm conv} = H/v_{\rm conv}$) drop below 1 second, faster than the heating timescale, $\tau_{\rm heat}$. This particular flash does not become dynamical, as dynamical flash models could not be evolved passed a $\tau_{\rm heat}$ minimum.

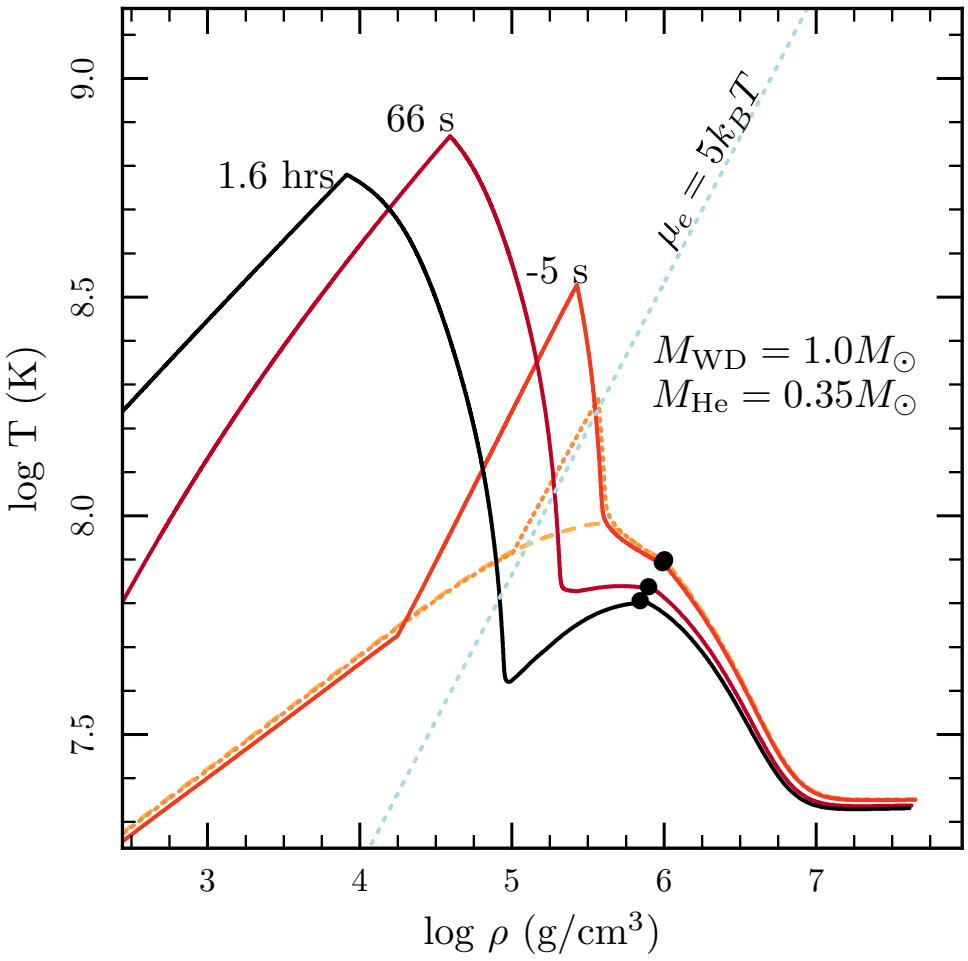

Figure 2.8 Temperature-density profiles from the specific helium explosion studied in this section. The $0.0436M_{\odot}$ of helium sits on a $1.0M_{\odot}$ C/O core. The size of the convective envelope (all the mass above the burning zone) is $0.0171M_{\odot}$. The first profile is dashed (1530 yrs before min. $\tau_{\rm heat}$), the second profile is dotted (0.5 yrs before min. $\tau_{\rm heat}$), and the third, fourth and fifth are labelled above by time since min. $\tau_{\rm heat}$. The black markers show the base of the helium shell in each profile (helium mass fraction $Y < 0.05$). The light blue dotted line marks the degeneracy border where $\mu_e = k_B T$.

In Figure 2.10 we plot a composition profile of the helium envelope. The accreted material is almost pure helium with ≈1% ^{14}N, and the pre-dynamical convective burning produces ≈2% ^{12}C and negligible ^{16}O.

As the results of Figures 2.7 and 2.9 show, these helium shells evolve rapidly and we

certainly should not depend on a hydrostatic code to resolve any transition to a more dynamical outcome such as a deflagration or detonation. However, we have shown that many of these first flashes (especially those with $M_{\rm He} > 0.4 M_\odot$ and $M_{\rm WD} > 0.8 M_\odot$) have an adequately massive convecting helium shell to trigger dynamical burning (i.e. deflagration or detonation). In light of more recent work, specifically Shen & Moore (2014), who showed that using a larger nuclear reaction network that allows the proton-catalyzed α-capture $^{12}\mathrm{C}(p,\gamma)^{13}\mathrm{N}(\alpha,p)^{16}\mathrm{O}$ significantly reduces that effective ^{4}He lifetime, detonations are able to begin and propagate in much lower mass shells. This and other reaction rates depend on the relative abundances in the burning layer. Therefore we need to know not only the composition of the accreted matter, but also the build-up of burning products from pre-dynamical convective burning.

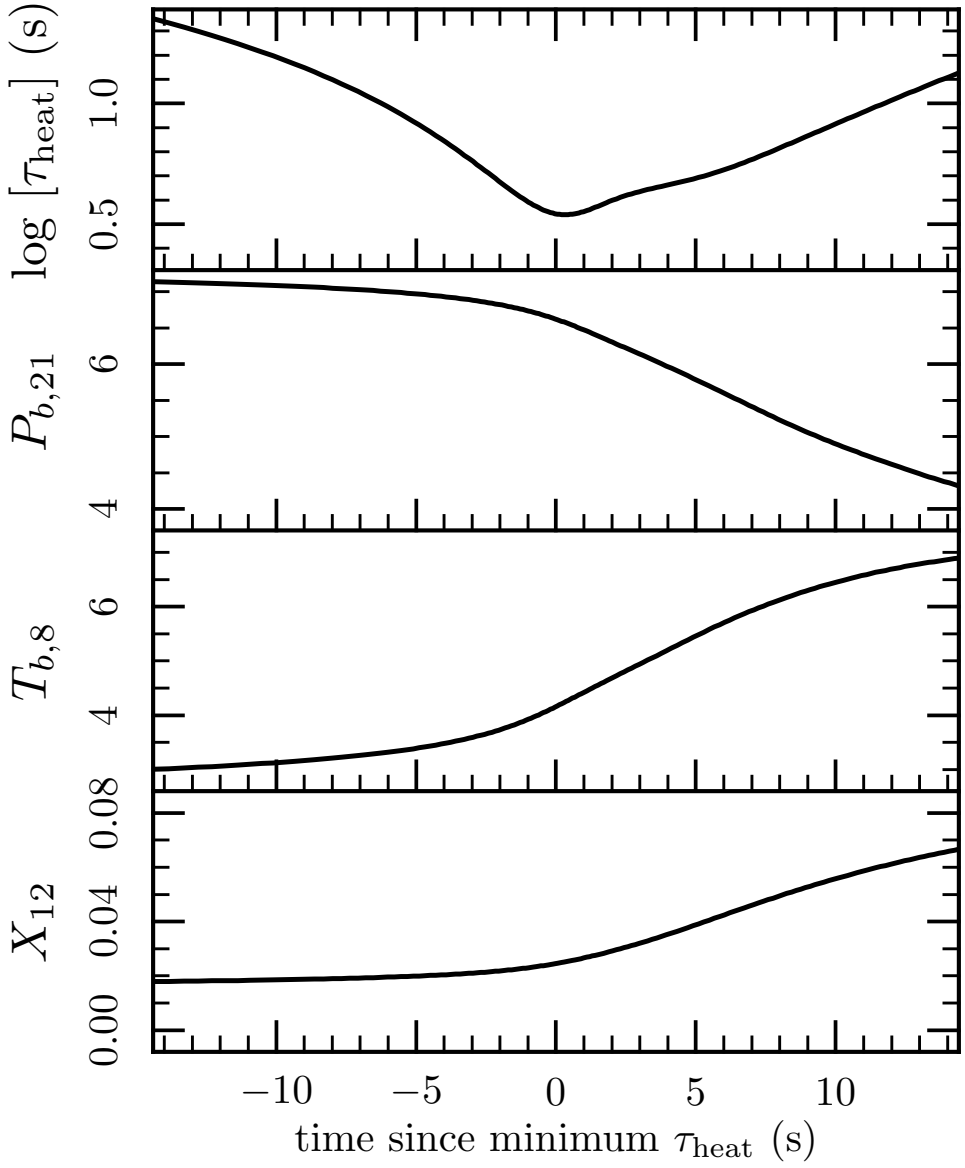

Figure 2.9 Same model as Figure 2.8. Shown are the evolution of four quantities defined at the maximum burning zone, with $t = 0$ corresponding to the minimum $\tau_{\rm heat}$. The top row shows the local heating timescale, $\tau_{\rm heat} = c_p T/\epsilon_{nuc}$. The second row shows the local pressure, $P_{b,21} = P_b/10^{21}$erg$\cdot$ cm^{-3}. The third row shows the local temperature, $T_{b,8} = T_b/10^8$K. The bottom row shows the local mass fraction of ^{12}C, X_{12}.

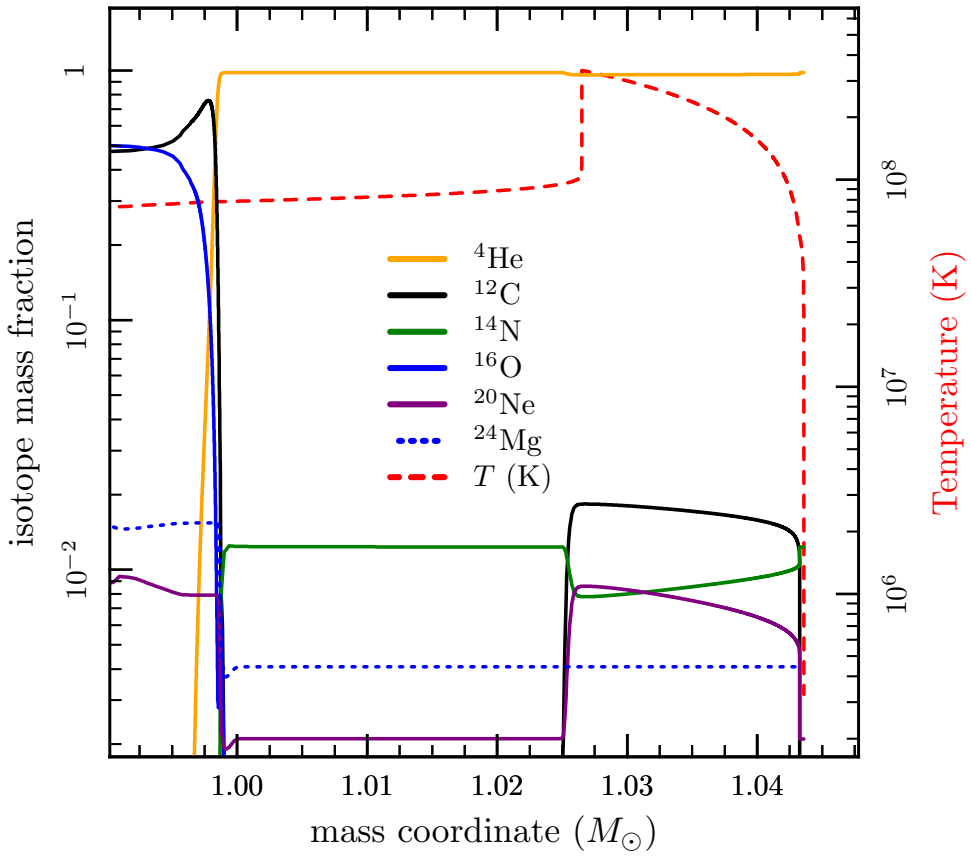

Figure 2.10 Composition and temperature profile of the helium envelope for the first burst of the system with $M_{\rm He} = 0.35 M_\odot$, $M_{\rm WD} = 1.0 M_\odot$ near minimum $\tau_{\rm heat}$.

With the composition information from Figure 2.10, which, as we stated above, is typical of the bursts studied here, we can plot each of these bursts on Figure 10 of Shen & Moore (2014), which tells that all the bursts studied here will be able to laterally propagate helium detonations. Furthermore, it tells us that the largest bursts from the $0.8 M_\odot$ and the $1.0 M_\odot$ WD accretors, and all the bursts from the $1.26 M_\odot$ WD accretor, will produce a significant fraction of isotopes that are radioactive on relevant timescales ($X_{\rm 48Cr} + X_{\rm 52Fe} + X_{\rm 56Ni} > 0.2$). The rest of the smaller bursts will be rich in ^{28}Si and ^{40}Ca, but will mainly consist of unburnt helium, which will likely be neutral and unobservable.

2.3.2 Case Study: CD-30°11223

The system CD-30° 11223 is the only known sdB+WD binary system expected to make contact within the sdB's core He-burning lifetime. We used data measured by Geier et al. (2013) to model this system, which includes a $0.51 M_{\odot}$ sdB star and a $0.76 M_{\odot}$ WD in an orbital period of 70.5 minutes. Comparison of measurements to simulated sdB evolutionary tracks in the $T_{\rm eff} - \log g$ diagram suggest that the sdB had just recently been formed and started the core He-burning phase.

Given the longer initial orbital period of this system compared to the systems in this study, the sdB had a longer time for core He-burning to inject heat into the envelope, leaving the star in a higher entropy state when mass transfer starts. This leads to a lower mass transfer rate during the plateau phase by a factor of a few. The lower mass transfer rate allows a larger helium shell to build up on the WD before thermonuclear runaway occurs.

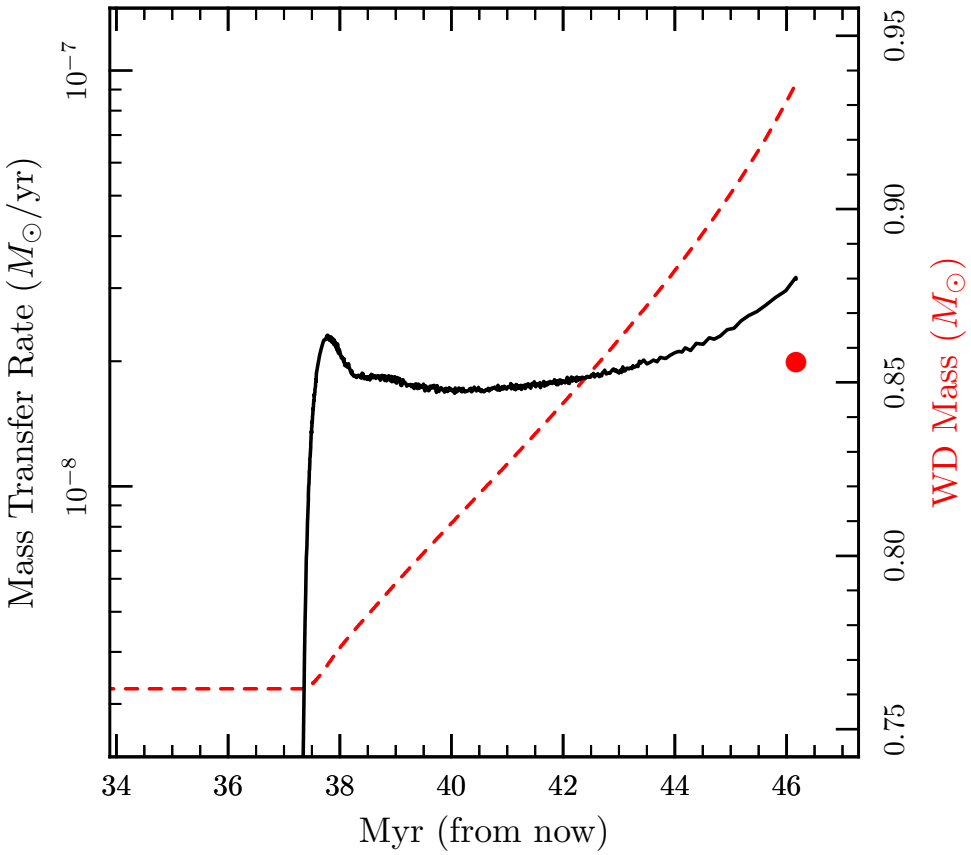

Figure 2.11 Mass transfer rate shown in black solid line, left y-axis. Mass of the WD accretor in red dashed line and mass coordinate of the ignition location as a red marker, right y-axis.

Our results from modeling this system show (Figure 2.11) that the helium star fills its Roche lobe after 37.3 Myr at an orbital period of 32 minutes. The donor transfers $0.18M_\odot$ of helium to the WD before thermonuclear runaway after 46.1 Myr at an orbital period of 16.5 minutes. Compare this to the prediction of Geier et al. (2013) of a helium shell of $0.1M_\odot$ that explodes after only 42 Myr at an orbital period of 27.4 minutes. The initial mass transfer rates we computed agree well with those in Geier et al. (2013), but our model climbs to higher accretion rates by about 50% by the first burst.

Our model shows a $0.09M_\odot$ convective envelope on top of a ($0.76M_\odot$ C-O + $0.09M_\odot$ cold He) $0.85M_\odot$ core, which will detonate and produce a significant mass of radioactive

isotopes.

2.4 Later Flashes and Subsequent Evolution

If we assume that the system survives the first flash, the loss of mass via the ejection of the helium envelope will cause the binary separation to increase. GWR will then bring the component stars back into contact, and the cycle of helium accumulation, ignition, and ejection continues until the mass transfer rates fall to such low values that another ignition never occurs (Shen & Bildsten, 2009). To model this, each time helium burning on the WD begins to run away, the helium envelope is removed from the system, taking with it the specific orbital angular momentum of the WD.

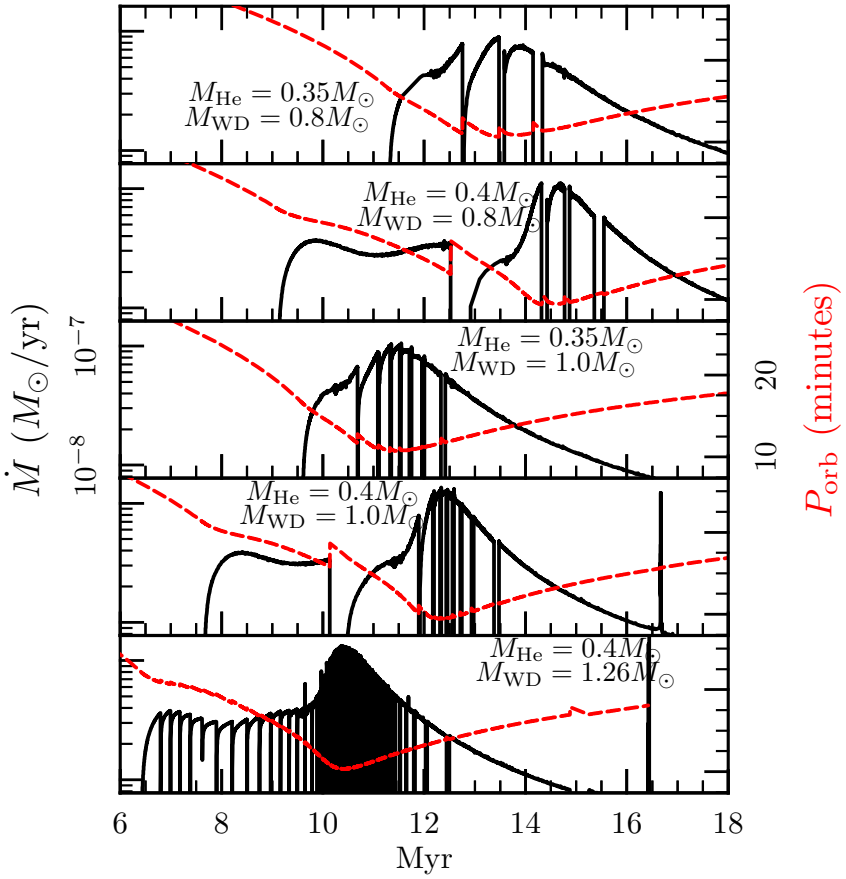

Figure 2.12 Four true binary runs all started at $P_{\rm orb,0} = 40$ minutes. The WD accretors experience between 3 and 9 bursts, each of which temporarily shut-off mass transfer. Mass transfer rates are shown by the black solid lines and the orbital periods are shown by the red dashed lines. All panels have the same scale.

We show the effects on the mass transfer and orbital period histories caused by including the mass ejection episodes in Figure 2.12. The $0.35M_\odot$ donor models lack the plateau feature in the $0.4M_\odot$ donor models because the thermal timescale ($\tau_{\rm KH}$) drops below the mass transfer timescale ($\tau_{\dot{M}}$) much sooner for lower mass donors. The higher mass WDs have lower envelope masses ($\Delta M_{\rm env}$) necessary for helium ignition, so these models have more bursts. This behavior can also be seen in Figure 2.13, which shows the mass of helium shell in the black lines, and the luminosities of the helium star and

WD in red and blue, respectively.

Before contact, the helium star is more luminous than the WD. After contact, that relation is reversed, and $L_{\rm WD} \sim 10 L_\odot$. This approximately matches the compression luminosity, $L_{\rm comp} \approx 3 k_B T_c \langle \dot{M} \rangle / \mu m_p$, given in Bildsten et al. (2006). This does not include the accretion luminosity, $L_{\rm acc} \approx G M_{\rm WD} \dot{M} / R_{\rm WD} \sim 100 L_\odot$, which is released in the accretion disk and will outshine both stars.

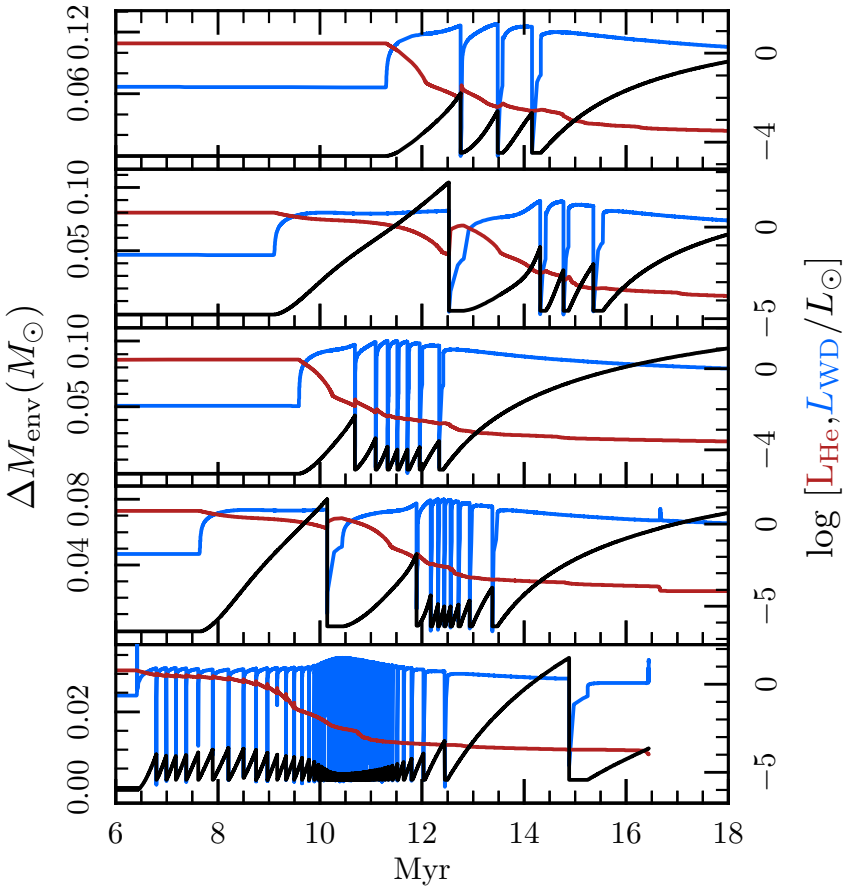

Figure 2.13 Same four binary runs as in Figure 2.12. Mass of the helium envelope on the WD ($\Delta M_{\rm env}$) shown in black lines, luminosities of the helium star and WD in red and blue, respectively.

For bursts that remove enough mass and mass transfer is shut off for long enough, the WD can be seen to dim to the original cooling curve, before climbing back up to the compression luminosity once mass transfer begins again. During these same periods, after a

burst but before re-contact, the donor luminosity increases. This happens because during mass loss periods, the nuclear burning luminosity in the donors core is absorbed in the stellar envelope (Yungelson, 2008). In the donor's envelope there is no nuclear burning, so the luminosity's slope is dominated by mass loss ($dL/dm \approx (\dot{M}/\Delta M)(k_B T/m_p) < 0$, where ΔM is overlying mass). When mass loss suddenly shuts off, this mass loss term disappears giving $dL/dm \approx 0$ in the envelope, meaning the trapped heat gets released on the timescale $\sim 10^4$ years.

The features seen in the bottom two panels after 16 Myr result from the exposure of the once convective helium burning core. When sharp compositional gradients are exposed, the mass transfer rates experience a spike.

For all cases studied here, except the one with $M_{\rm WD} = 1.26 M_\odot$, the first burst is the largest because the helium is accumulated at the lowest rate. As the mass transfer rates decrease after the period minimum, they quickly become too low to trigger helium ignitions (Shen & Bildsten, 2009) and the WD ends up with a cold, thick helium shell. The case with the $M_{\rm WD} = 1.26 M_\odot$ accretor is the only case in which the last explosion is the strongest (Figure 2.7), as the ignition mass is much lower for the more massive WD accretors. In fact, the last explosion on the $M_{\rm WD} = 1.26 M_\odot$ accretor is the most powerful one studied here. After this last explosion, likely as a .Ia SN, the donor does not have enough mass left to increase the mass of the accretor to the Chandrasekhar mass, so an accretion induced collapse is not expected through this channel.

2.5 Conclusions

We present the first self-consistent calculation of mass transfer between a low-mass helium star and a WD in a short-period binary and the resulting helium shells and their explosions on the surface of the WD. We started by simulating the secular evolution of

low mass helium stars, that is, evolved with a point-mass binary companion, to see how structure and mass-loss feed back on each other. We found, confirming Yungelson (2008), that during the first stage of mass transfer, the donor maintains thermal equilibrium, as $\tau_{\rm KH} < \tau_{\dot{M}}$, leading to a relatively constant $\dot{M}$ during the so-called plateau phase. Eventually the donor loses enough mass to effectively shut-off nuclear burning and reverse the timescale inequality, meaning the star responds adiabatically to mass-loss. At this point mass transfer rates rise until mass transfer effects become dominant over GWR in determining the orbital separation, and the system reaches a period minimum of 9-10 minutes, after which the binary separation increases. Core evolution proceeds adiabatically along nearly constant entropy trajectories that are mildly degenerate until nearly all the mass of the donor has been removed.

When we include the evolution of the accreting WD in the binary simulations, helium shells build up on the WD until a thermonuclear runaway develops. In studying these models, we find that the first flash is usually the largest, and the first flashes from systems with $M_{\rm He} > 0.4 M_\odot$ and $M_{\rm WD} > 1.0 M_\odot$ meet the requirements for triggering dynamical burning and developing a deflagration or detonation. Using the conditions derived by Moore et al. (2013) and Shen & Moore (2014), all the flashes studied here, including the "later" flashes, are massive enough to sustain a laterally propagating detonation within the He shell. Furthermore, the first bursts from the $0.8 M_\odot$ and the $1.0 M_\odot$ WD accretors, and all the burst from the $1.26 M_\odot$ WD accretor, will produce a significant fraction of isotopes that are radioactive on relevant timescales.

We also follow through with some simulations assuming that the first helium flash does not unbind the WD. The ejected mass increases the binary separation, temporarily shutting off mass transfer until GWR brings the stars back into contact. This series of events repeats itself until the stars are far enough apart and mass transfer rates are low enough to prevent runaways in the helium shells.

Chapter 3

Carbon Shell or Core Ignitions in White Dwarfs Accreting from Helium Stars

White dwarfs accreting from helium stars can stably burn at the accreted rate and avoid the challenge of mass loss associated with unstable Helium burning that is a concern for many Type Ia supernovae scenarios. We study binaries with helium stars of mass $1.25M_{\odot} \leq M_{\rm He} \leq 1.8M_{\odot}$, which have lost their hydrogen rich envelopes in an earlier common envelope event and now orbit with periods ($P_{\rm orb}$) of several hours with non-rotating 0.84 and $1.0M_{\odot}$ C/O WDs. The helium stars fill their Roche lobes (RLs) after exhaustion of central helium and donate helium on their thermal timescales ($\sim 10^5$yr). As shown by others, these mass transfer rates coincide with the steady helium burning range for WDs, and grow the WD core up to near the Chandrasekhar mass ($M_{\rm Ch}$) and a core carbon ignition. We show here, however, that many of these scenarios lead to an ignition of hot carbon ashes near the outer edge of the WD and an inward going carbon flame that does not cause an explosive outcome. For $P_{\rm orb} = 3$ hours, $1.0M_{\odot}$ C/O WDs with

donor masses $M_{\rm He} \gtrsim 1.8 M_\odot$ experience a shell carbon ignition, while $M_{\rm He} \lesssim 1.3 M_\odot$ will fall below the steady helium burning range and undergo helium flashes before reaching core C ignition. Those with $1.3 M_\odot \lesssim M_{\rm He} \lesssim 1.7 M_\odot$ will experience a core C ignition. We also calculate the retention fraction of accreted helium when the accretion rate leads to recurrent weak helium flashes.

The possible progenitor systems for SNe Ia presently fall into two categories: the single degenerate and double degenerate scenarios, each with theoretical challenges. The double degenerate scenario, characterized by the merger of two WDs that unstably ignites degenerate carbon, is challenged because an off-center ignition of carbon likely converts C/O WDs to O/Ne WDs via an inward-propagating carbon flame (Nomoto & Iben, 1985; Saio & Nomoto, 1985; Woosley & Weaver, 1986; Saio & Nomoto, 1998; Shen et al., 2012). Recent 3D simulations of these mergers found a prompt detonation can be triggered during the merger process when the mass ratio is close to unity (Pakmor et al., 2010, 2011, 2012; Ruiter et al., 2012). The single degenerate scenario, characterized by stable accretion onto WDs until they grow to the Chandrasekhar mass ($M_{\rm Ch}$), is challenged by many theoretical and observational issues, including hydrogen flashes, or flashes of the helium built up via steady hydrogen burning, which remove mass, possibly preventing efficient growth of the core (Iben & Tutukov, 1989; Nomoto et al., 2007; Wolf et al., 2013). Included in the single degenerate scenario, however, are systems with helium star donors of mass $M_{\rm He} \approx 1.2 - 1.8 M_\odot$ that donate He-rich matter to WDs at $\dot{M} > 10^{-6} M_\odot {\rm yr}^{-1}$. This avoids hydrogen flashes, and, given a certain range of helium star masses, can allow for steady helium burning on the surface of the WD at the rate that it is accreted (Yoon & Langer, 2003; Shen & Bildsten, 2007; Piersanti et al., 2014) leading to steady growth of the WD core and a possible core carbon ignition. However, at these large $\dot{M}$s, another possible outcome is a shell ignition of carbon that will non-explosively convert a C/O WD to an O/Ne WD, leading eventually to an accretion induced collapse (AIC) rather

than a SN Ia (Nomoto & Iben, 1985; Saio & Nomoto, 1985, 1998).

Wang et al. (2009) explore this channel using an optically thick wind model (Hachisu et al., 1996), instead of solving the stellar structure equations of the accreting WDs. They find the area in the initial orbital period $-M_{\rm He}$ plane where binary systems with these initial parameters will end in core ignitions. Assuming that the core ignitions lead to Type Ia SNe, they perform binary population synthesis (BPS) studies and calculate the birthrate of SNe Ia. By not solving the stellar structure equations of the WDs, however, they do not take into account the possibility of non-explosive shell carbon ignition. As we show, the effect of including this possibility shrinks the area in the $\log P_{\rm orb,0} - M_{\rm He}$ plane that lead to SNe Ia, and lowers the estimated SNe Ia rate through this channel.

In §3.1 we calculate the boundaries for steady helium burning accretion rates using `MESA` (Paxton et al., 2011, 2013; Paxton et al., 2015), and explain the behavior of the models above and below the steady helium burning range. Then in §3.2 we explore the behavior of the core as it grows to core ignition near $M_{\rm Ch}$ and explain the "race" to ignition between carbon the core and in the shell. We include in §3.3 a discussion on the effects of neutrino cooling the cores of the WDs, discuss the possible observables from these systems in §3.4, and explore a low mass binary case that leads to a double degenerate scenario in §3.5. We conclude in §3.6.

3.1 Steady Helium Burning

When binary systems have high mass helium star donors ($1.3M_{\odot} \leq M_{\rm He} \leq 1.8M_{\odot}$) the mass transfer is driven by the expansion of the donor as core helium is exhausted and the star leaves the He-main sequence. This allows for mass transfer rates that cross the regime for steady He burning (Piersanti et al., 2014).

3.1.1 Calculation of Steady He burning boundaries

The steady burning boundaries are calculated using `MESA` (r7624) by taking a set of WD models that span the mass range [0.8,1.397] $M_\odot$ and running them each with various $\dot{M}$'s. We first create a steady burning model for each mass by setting an $\dot{M}$ in the middle of the steady burning zone from Piersanti et al. (2014), calculating through the first burst and allowing the burning rate to stabilize. The example case shown in Figures 3.1 and 3.2 is for a $1.25M_\odot$ model that starts with $\dot{M}_{\rm WD} = 3.5 \times 10^{-6} M_\odot$ yr^{-1}. Then we lower the accretion rate until the burning rate, $L_{\rm nuc}$, begins to oscillate by more than 15 per cent, and use this accretion rate as the lower steady burning boundary.

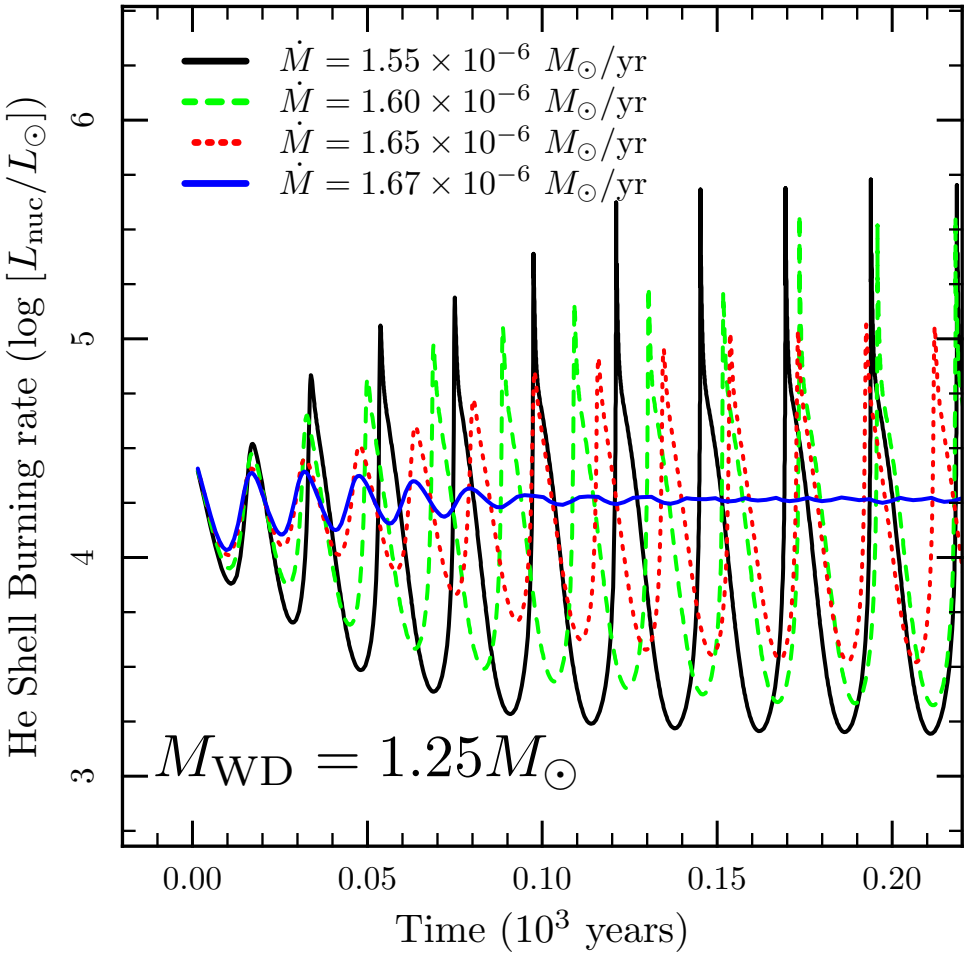

Figure 3.1 Nuclear burning rates for a narrow set of accretion rates near the lower stability boundary for a $1.25 M_\odot$ WD. Starting from a stable burning model at $\dot{M}_{\rm WD} = 3.5 \times 10^{-6} M_\odot$ yr^{-1}, the accretion rate is lowered to shown values. Above a certain accretion rate the oscillations in the burning rate are effectively damped.

The lower stability boundary exists because at lower accretion rates, the helium shell has a lower temperature and higher density. When the accretion rate is lowered beneath the lower stability boundary, the heating timescale drops below the time required for the shell to adjust its thermal structure and a temporary runaway occurs. Above this boundary, the shell is hotter and less dense such that the thermal structure can adjust quickly enough in response to helium ignition, so nuclear burning rates are able

to stabilize, as shown in Figure 3.1.

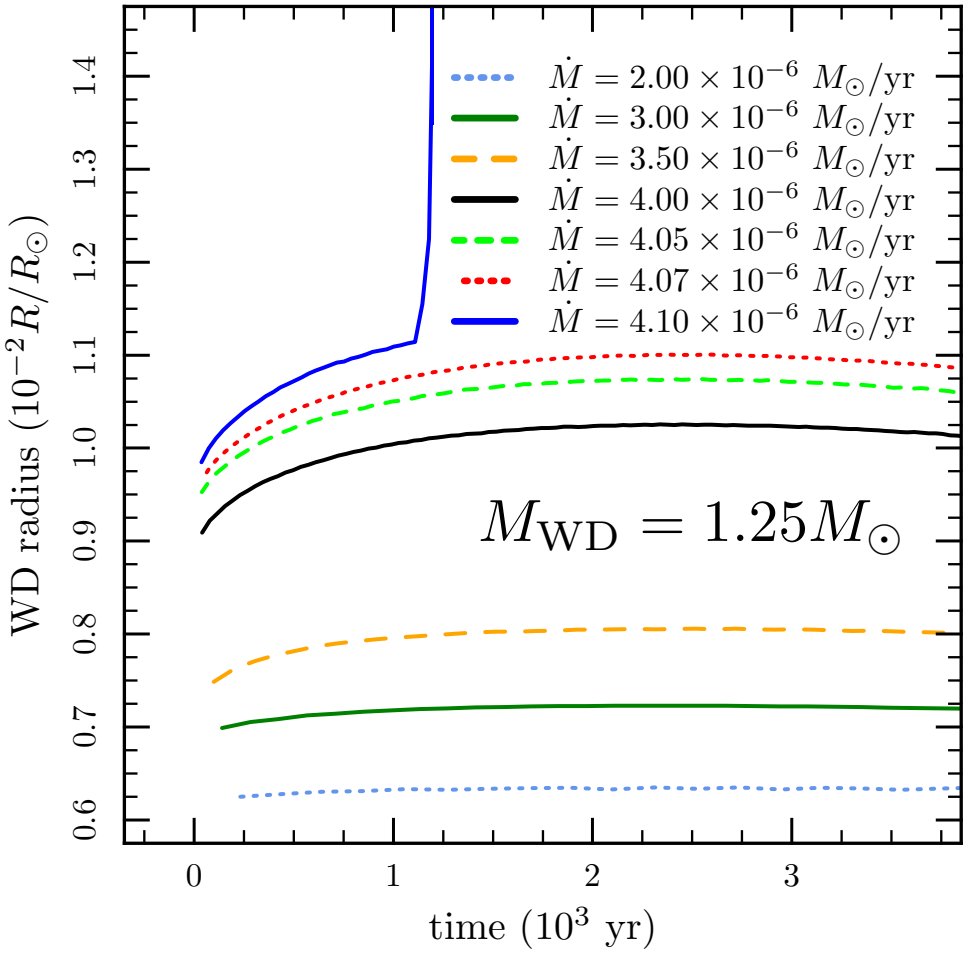

Figure 3.2 Starting from $\dot{M}_{\rm WD} = 3.5 \times 10^{-6} M_\odot$ yr^{-1} on a $1.25 M_\odot$ WD, the accretion rate is raised to the shown value. Above a certain accretion rate, the radius rapidly expands as the WD enters the RG regime.

To find the upper steady burning boundary, we raise the accretion rate until the surface radius experiences a rapid expansion. Increasing the accretion rate discontiously, as we have done here, will naturally increase the surface radius, but only by a factor of order unity. Due to the core mass-luminosity relation (Paczyski, 1971), there exists a maximum luminosity at which it can burn, and therefore a maximum accretion rate (Shen & Bildsten, 2007). Once the accretion rate increases above this threshold, mass

builds up in the shell and the WD either enters the RG regime (Piersanti et al., 2014) or drives an optically thick wind (Hachisu et al., 1999), both resulting in the rapid expansion of the surface radius by a few orders of magnitude, as shown in Figure 3.2.

3.1.2 He Burning during Binary Evolution

While the system is in the regime for steady He-burning, the WD is burning helium to carbon and oxygen at the same rate that it is accreting helium. As the mass transfer rates rise above the steady burning regime, the WD rapidly expands into its Roche lobe and only accepts mass at the maximum steady burning rate. The rest of the mass is lost from the system such that $\dot{M}_{\rm WD} + \dot{M}_{\rm wind} = -\dot{M}_{\rm He}$, where $\dot{M}_{\rm wind}$ is the rate of mass loss from the binary system, as shown by the difference between the dotted and solid lines in Figure 3.3.

We compute $\dot{M}_{\rm wind}$ by attenuating the mass transfer efficiency as the WD expands into a significant fraction of its Roche lobe. The shape of the mass transfer efficiency versus $R_{\rm WD}/R_{\rm RL}$ has little effect on the $\dot{M}$ accepted by the WD due to the high sensitivity of the WD radius to the accretion rate near the upper stability boundary, as shown in Figure 3.2. The dynamic range of radii within the steady helium burning range is relatively small compared to that near the upper steady boundary. We compare this method with that used in Yoon & Langer (2003) who used a radiation driven wind using $\dot{M} = 10^{-2} R_{\rm WD} L_{\rm WD}/[G M_{\rm WD}(1-\Gamma)]$, where $R_{\rm WD}$, $L_{\rm WD}$, and $M_{\rm WD}$ are the radius, luminosity, and mass of the WD, and Γ is the ratio of photospheric luminosity to the Eddington luminosity. For their model starting with $M_{\rm WD} = 1.0 M_\odot$, $M_{\rm He} = 1.6 M_\odot$, when $M_{\rm WD} = 1.04 M_\odot$ the wind reaches a maximum of $4.8 \times 10^{-6} M_\odot$ yr^{-1}. In our model with the same initial conditions, at the corresponding point in evolution, we calculate a maximum wind rate of $4.2 \times 10^{-6} M_\odot$ yr^{-1}, which is comparable.

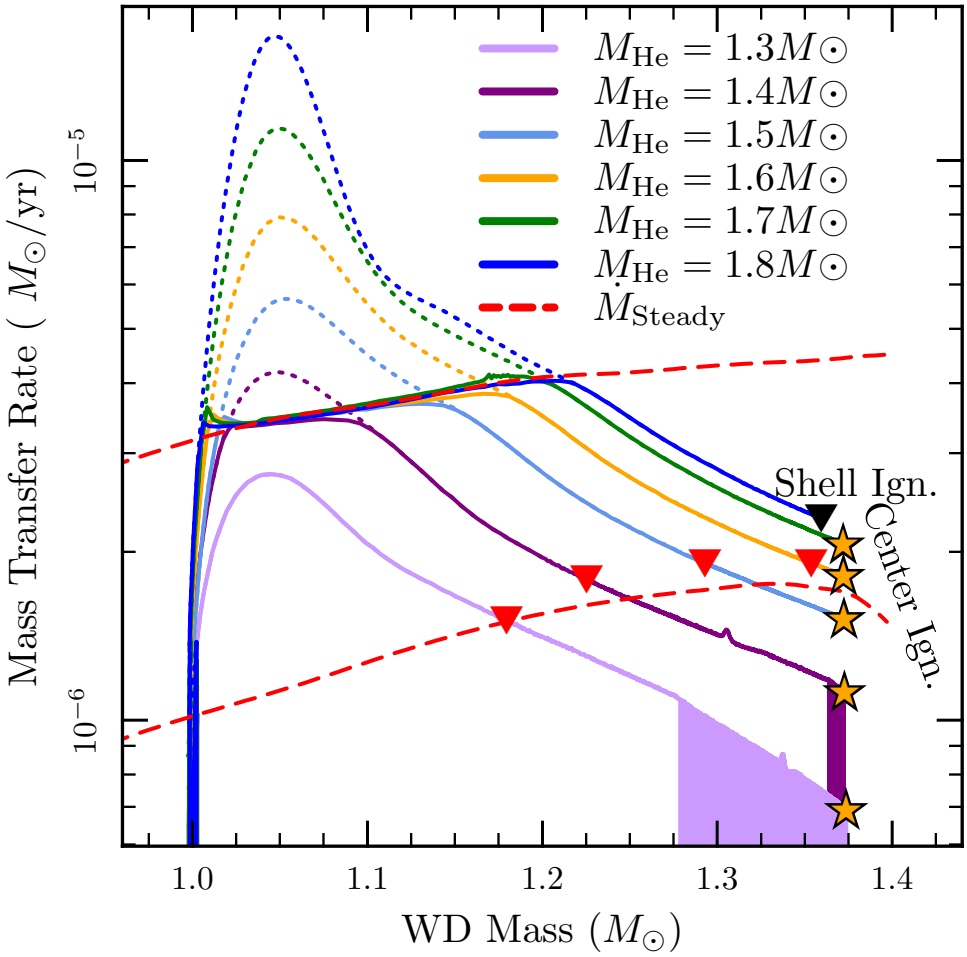

Figure 3.3 Evolutionary tracks of the mass transfer rates for six systems with different initial donor masses. All systems start with the same WD accretor model ($M_{\rm WD} = 1.0M_\odot$) and the same initial orbital period ($P_{\rm orb,0} = 3$ hours). The solid tracks are the rate at which the WD is gaining mass; the dotted tracks are the rate at which the He star is losing mass. The difference between the dotted and solid tracks represent the mass that is lost from the system. The red dashed lines border the steady helium burning regime, as found in §3.1.1. The downward-facing red triangles mark where the helium burning rate begins to oscillate by more than a factor of two.

The system mass-loss increases the orbital separation, and thus acts to reduce the rapid mass transfer rates. We assume that the mass loss from the system takes with it the specific angular momentum of the WD, and address the validity of this assumption

in §3.1.3. When mass transfer rates fall back into, and then below the steady He-burning regime, the envelope begins to oscillate (in temperature, density, burning rate, etc.). The mass transfer rates as a function of the WD accretor mass are shown in Figure 3.3 for six models with different initial donor masses. The downward-facing red triangles mark where the helium burning rate begins to oscillate by more than a factor of two. They differ from the lower stability boundary due to their accretion history building a layer of hot C/O on top of the colder core.

Steady burning on the WD avoids the complications of flashes and whether the WD mass increases or decreases after multiple novae. On the other hand it introduces the complication of a possible carbon shell ignition before a core ignition. These high mass transfer rates and strong helium burning rapidly heat the outer-most carbon in the WD. So much so that if mass transfer rates stay too high for too long, the WD experiences a carbon shell ignition that (Nomoto & Iben, 1985; Piersanti et al., 2014) propagates inwards and transforms the C/O WD into a O/Ne WD. The situation that results is a "race" between the core and the shell as to which will ignite first.

Both the WD and helium star models were first constructed in single star evolution, with the only simulated binary interaction being the artificial removal of their envelopes at the last stage in their evolution before becoming a WD or helium star. After their envelopes have been removed, and the WD cools for 10 Myr, they are placed into a 3 hour orbit in a binary run. All simulation after this point are true binary runs whose angular momentum evolution is only affected by gravitational wave radiation (GWR) and mass loss as described in §3.1.3.

The mass transfer rate from the helium star due to Roche lobe overflow (RLOF) is computed using the "Ritter" implicit scheme of `MESA` (Paxton et al., 2015), which computes the prescription given by Ritter (1988).

3.1.3 Angular Momentum Loss in Winds

We now address the validity of the assumption that the mass loss from the system takes with it the specific angular momentum of the WD. It is perfectly valid if the wind leaves the system quickly without interacting with the binary after being launched off the WD's surface.

If, however, the wind speed is low, then it gets gravitationally torqued by the stars as it leaves the system, extracting extra angular momentum from the orbits. Hachisu et al. (1999) explore this issue of the angular momentum evolution in a binary, and parameterize the extraction of extra angular momentum from a slow wind. They first define the dimensionless quantity $l_{\rm wind}$ as

$$\left(\frac{\dot{J}}{\dot{M}}\right)_{\rm wind} = l_{\rm wind} a^2 \Omega_{\rm orb}, \tag{3.1}$$

where J is the total angular momentum, $\dot{M}$ is the mass loss rate of the system, a is the binary separation, and $\Omega_{\rm orb}$ is the orbital angular frequency. If, as per our assumption, the wind from the system takes with it the specific angular momentum of the WD, then $l_{\rm wind} = (q/(1+q))^2$, where q is the mass ratio $M_{\rm He}/M_{\rm WD}$. If the wind is slow, on the other hand, it extracts more angular momentum, and thus $l_{\rm wind}$ is larger. The expression for $l_{\rm wind}$ as given by Hachisu et al. (1999) is then

$$l_{\rm wind} \approx \max\left[1.7 - 0.55\left(\frac{v}{a\Omega_{\rm orb}}\right)^2, \left(\frac{q}{1+q}\right)^2\right], \tag{3.2}$$

where v is radial velocity of the wind near the RL surface.

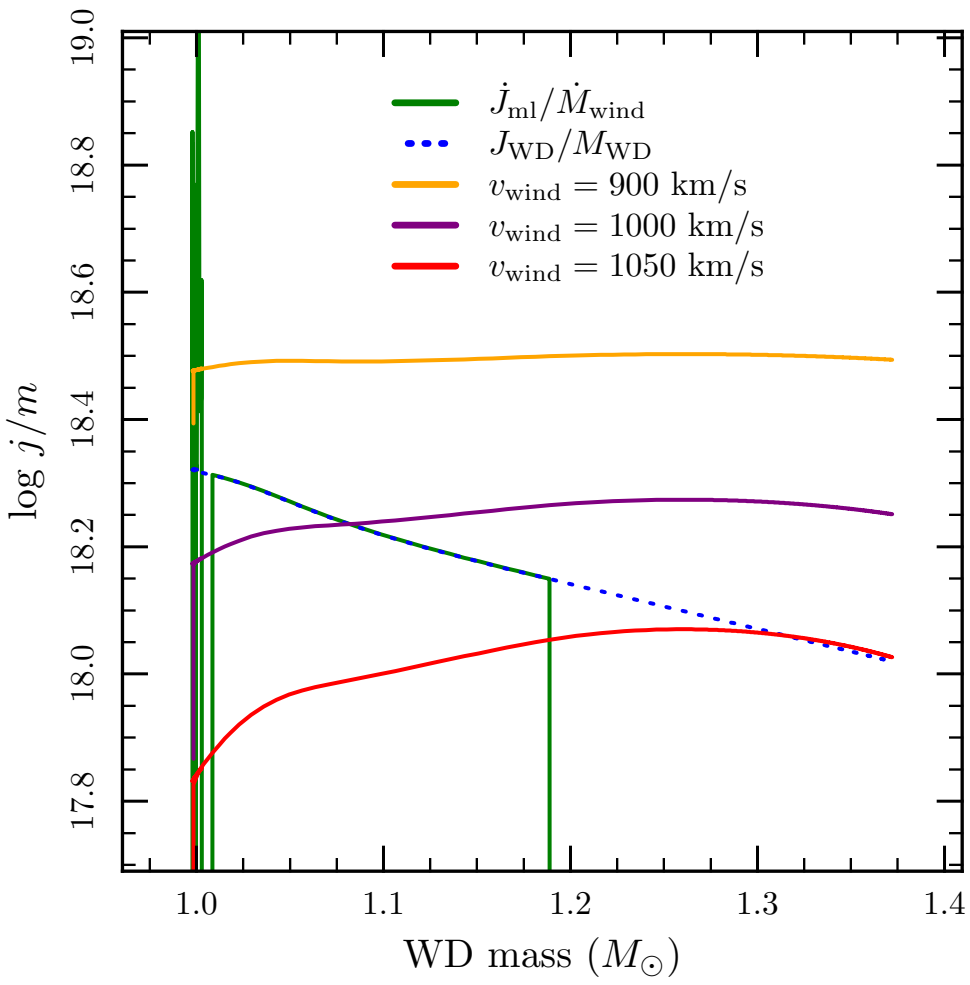

Figure 3.4 Angular momentum evolution for the binary case with $M_{\rm WD} = 1.0M_\odot$, $M_{\rm He} = 1.6M_\odot$. The specific angular momentum of the WD is shown by the blue dotted line. The specific angular momentum of the wind leaving the system is shown by the solid green line. The green line drops to zero when the WD mass reaches $\approx 1.19M_\odot$ because the system mass loss rate drops to zero. The orange, purple, and red solid lines show what the specific angular momentum of the wind would be if the speeds were 900, 1000, and 1050 km/s, respectively. This shows that our angular momentum loss rate assumptions are valid if $v_{\rm wind} \gtrsim 1000$km/s.

We show in Figure 3.4 for the case with $M_{\rm WD} = 1.0M_\odot$, $M_{\rm He} = 1.6M_\odot$, the specific angular momentum of the WD with the blue dotted line, and the specific angular momentum of the wind leaving the WD surface with solid green. The orange, purple, and

red solid lines are from equation 3.1 assuming the left-hand-side option in the square brackets in equation 3.2 with wind speeds of 900, 1000, and 1050 km/s, respectively. This figure shows that if $v_{\rm wind} \gtrsim 1000$ km/s, then our initial assumption that the mass loss from the system takes with it the specific angular momentum of the WD is valid. Lower wind velocities would extract extra angular momentum, thus decreasing the orbital period and increasing system mass loss rates. We did not consider that possibility for this initial exploration.

3.2 Core and Envelope Evolution

Here we return to describe the "race" between the core and the envelope as to which will ignite carbon first. We present example models that explore the different possible outcomes, and thus the final fate of these systems.

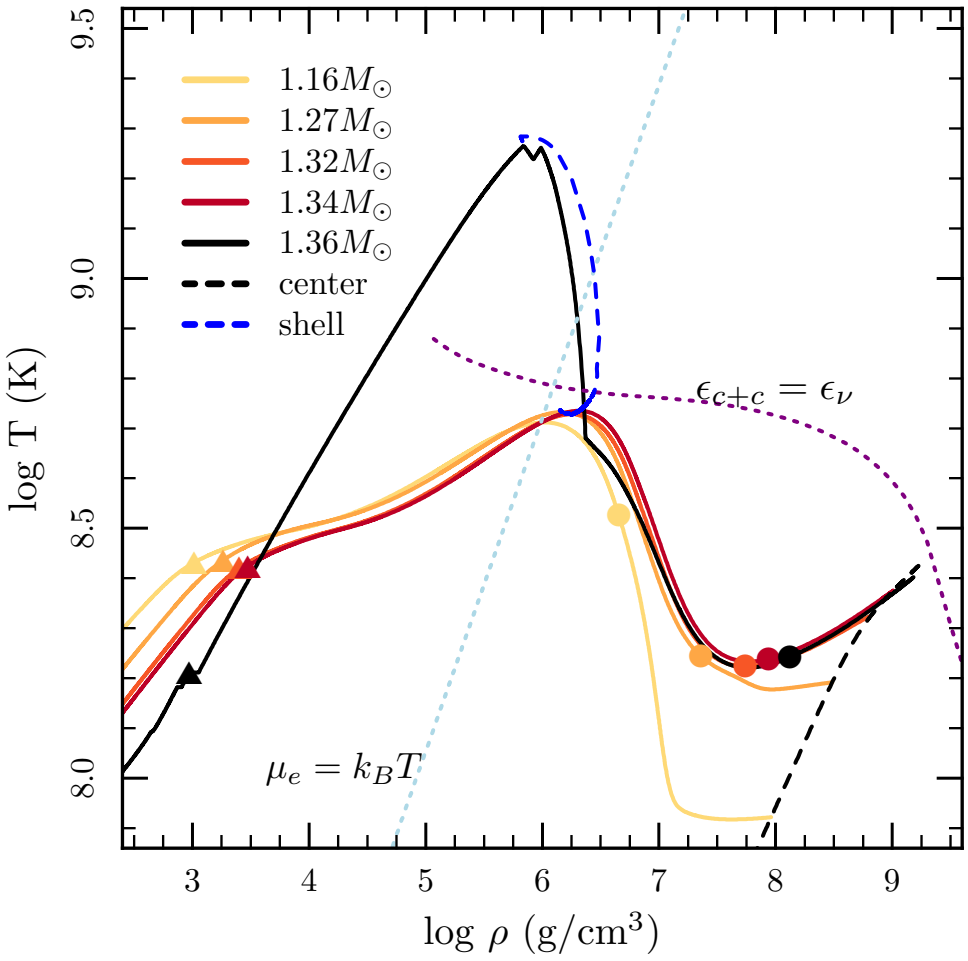

Figure 3.5 Binary system with $M_{\rm He} = 1.8M_\odot$. Solid lines show the profiles of the WD, labeled by the mass at that point in their evolution. They move in $\rho - T$ space towards the $\epsilon_{C+C} = \epsilon_\nu$ curve, but due to the high accretion rate the envelope crosses the curve first and the WD experiences a carbon shell ignition at the mass coordinate of $1.349M_\odot$, nearly at the surface. The triangles mark the helium burning zone, and the circles mark the mass coordinate $m_r = 1.0M_\odot$.

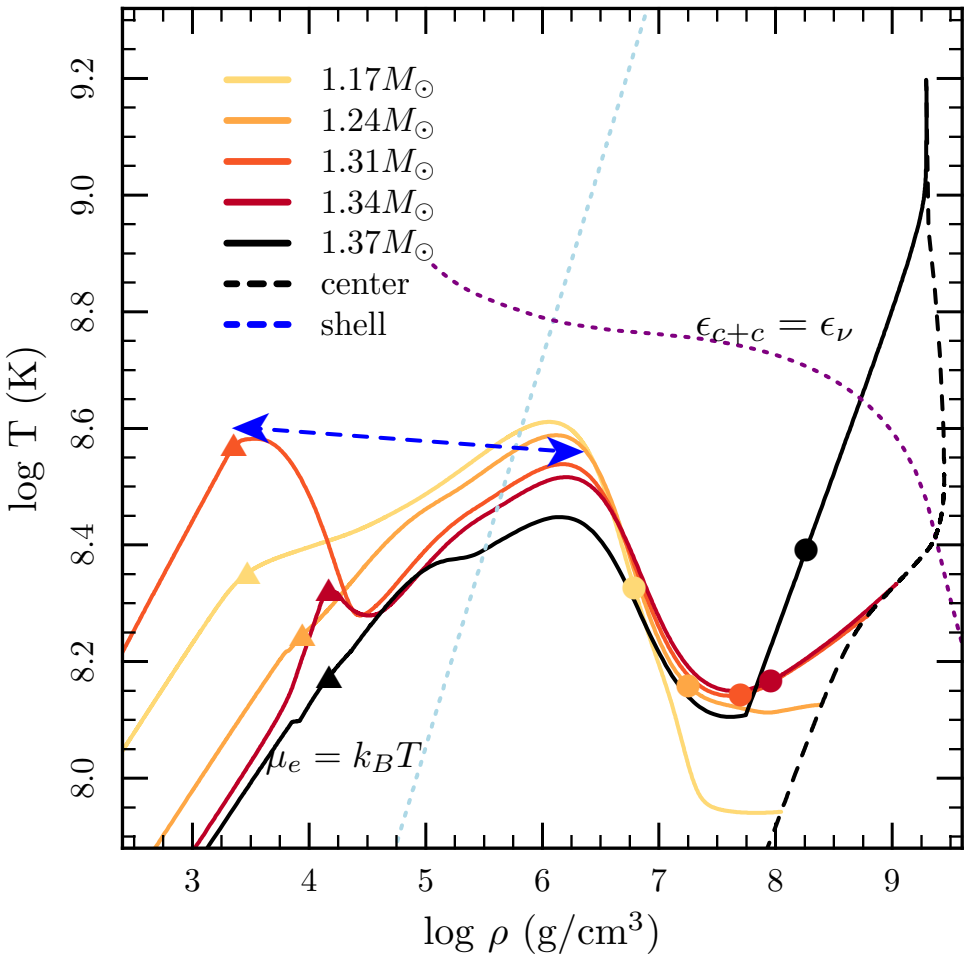

Figure 3.6 Profiles of the WD accretor model with $1.3M_\odot$ helium star donor. The triangles mark the helium burning zone, and the circles mark the mass coordinate $m_r = 1.0M_\odot$. The last few profiles show the envelope oscillating due to mass transfer rates falling below the steady He-burning regime.

We start with the case with the highest mass donor, and thus the highest accretion rates for the entire accretion lifetime. In Figure 3.5 we show the evolution of the core and the carbon shell (tracked by maximum temperature) of the model with initial donor mass $M_{\rm He} = 1.8M_\odot$. This case shows that high accretion rates dump more heat into the envelope than the compressionial heat in the core, and the shell crosses $\epsilon_{C+C} = \epsilon_\nu$ before the core. Shell carbon ignition occurs when the WD reaches a mass of $1.360M_\odot$ at a mass coordinate of $1.349M_\odot$, nearly at the surface.

On the low mass donor end, however, carbon may not ignite at all. The model with initial donor mass $M_{\rm He} = 1.3 M_\odot$ stays at lower accretion rates and falls far enough below the steady helum burning range that the mild helium oscillations become powerful enough to blow off mass. The blue dashed line shows how the maximum temperature in the shell will oscillate between the flashing helium burning shell and the hot, compressed C/O ashes below the burning layer. At these accretion rates, however, the accretion efficiency stays above 70%, allowing the WD to gain enough mass to trigger carbon ignition in the core. We compare our accreted mass retention efficiency calculated in the final stages of this model using super-Eddington winds to the analytical estimates of Kato & Hachisu (2004) and Wang et al. (2015) in Figure 3.7. Wang et al. (2015) used `MESA` (r3661) for their study, but used the default super-Eddington wind settings, whereas we triggered super-Eddington winds while the WD is still in a compact configuration in order to speed the computation. Systems with donor mass $M_{\rm He} \lesssim 1.3 M_\odot$, therefore, will fall to lower accretion rates and efficiencies, and ultimately lose contact before a core ignition occurs. The components, now both C/O WDs, will spiral in due to GWR and contribute to the double-degenerate channel for SNe Ia, as discussed in §3.5.

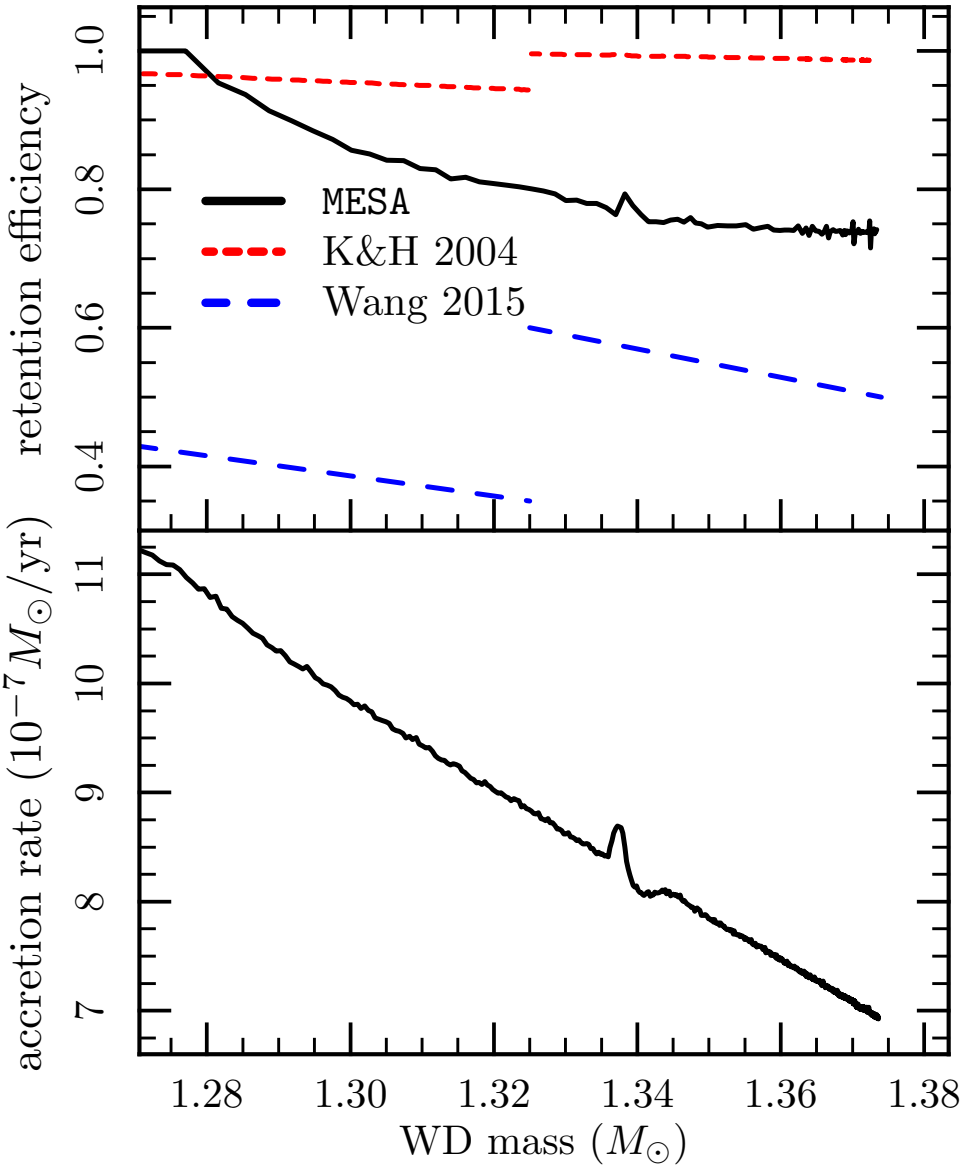

Figure 3.7 The top panel shows the accreted mass retention efficiency during the last stages of the system with the $1.3 M_\odot$ donor stars. The black line shows what we calculated by taking the ratio of the growth rate of the accretor and the mass loss rate of the donor. The red short-dashed lines show the retention efficiency given analytically by Kato & Hachisu (2004) for 1.3 and $1.35 M_\odot$ cores. The blue long-dashed lines show the retention efficiency given analytically by Wang et al. (2015) for 1.3 and $1.35 M_\odot$ cores. The bottom panel shows the mass transfer rate being donated to the WD.

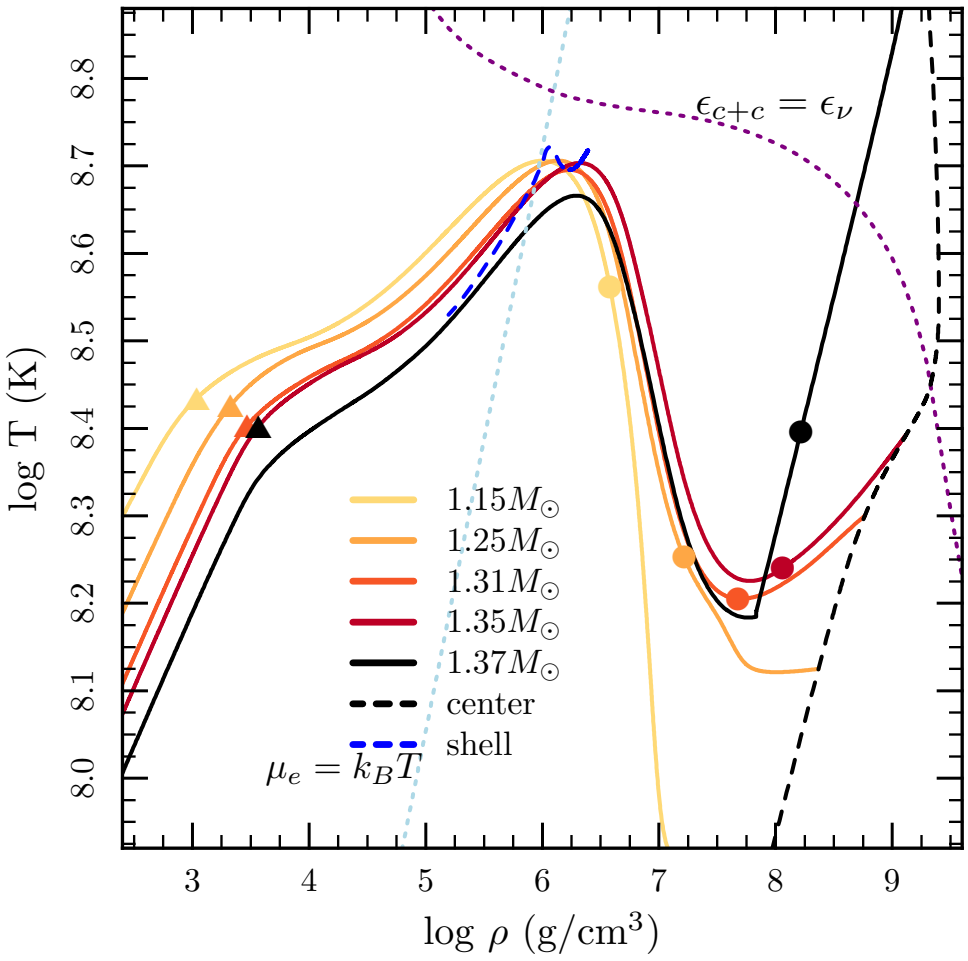

Figure 3.8 Profiles of $\rho - T$ of the WD in the binary system with $M_{\rm He} = 1.6M_\odot$. Markings have the same meaning as in Figure 3.6.

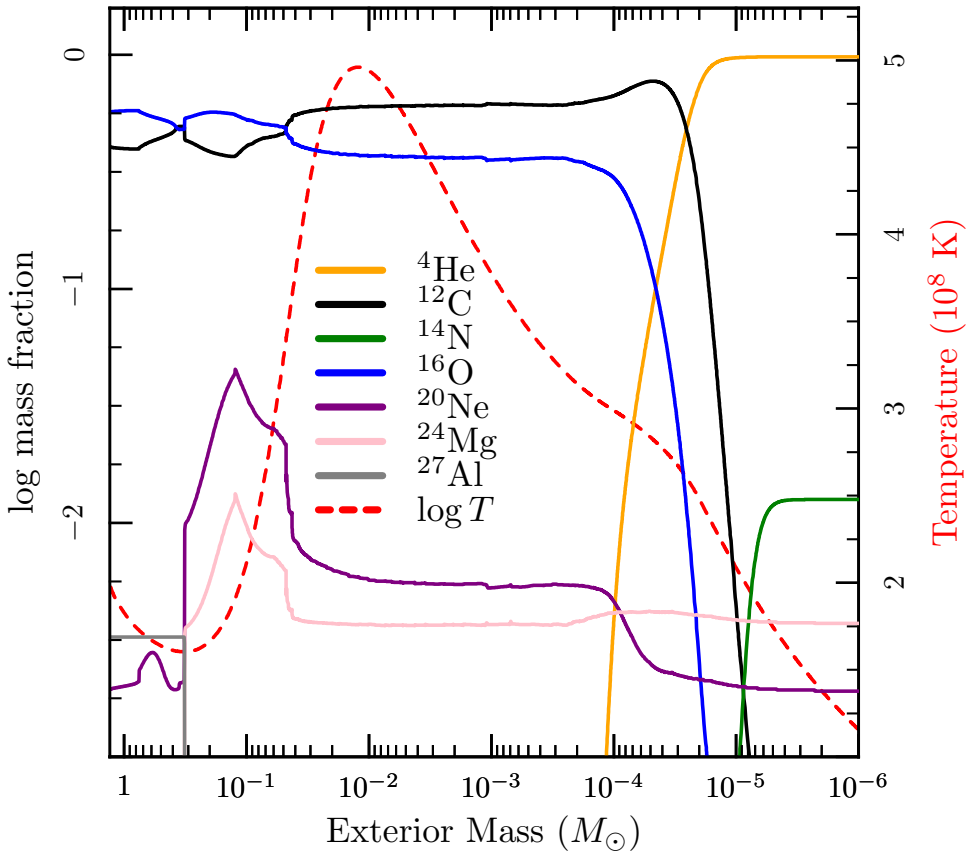

Figure 3.9 Profile of abundance on the left y-axis and temperature in units of 10^8 K on the right y-axis. This is from the WD in the binary system with $M_{\rm He} = 1.6M_\odot$, using the same profile as the middle profile in Figure 3.8, when $M_{\rm WD} = 1.31M_\odot$.

Between the high and low mass donor limits is the region where core carbon ignitions occur. This is where the donor mass is high enough that the accretion rates do not fall too far below the stability boundary before $M_{\rm Ch}$ is reached, but also low enough that it avoids a carbon shell ignition from long sustained high accretion rates. A clear example of this is shown in Figure 3.8, with the trajectories of the core and envelope shown with profiles in $\rho - T$ space for a system with $M_{\rm He} = 1.6M_\odot$. In Figure 3.9 we show the composition and temperature profile when this model has grown to $1.31M_\odot$, the same profile as that in Figure 3.8. As the C/O envelope is $0.31M_\odot$, this shows that the base

is at a temperature minimum, and the temperature maximum in the envelope is only $\approx 10^{-2} M_{\odot}$ deep. The core ignition in these models indicates that they are likely SN Ia progenitors.

3.3 Deviations From Adiabatic Core Compression

The black dashed lines in the previous figures (Figures 3.5, 3.6, 3.8) show the WD core trajectory, which, at $T_c \approx 2 \times 10^8$K, deviates from the adiabatic compression expected for such high $\dot{M}$'s. Since there is no time for heat transfer at these rapid accretion rates, it is the onset of neutrino cooling (Paczyski, 1971) at a rate ϵ_ν that leads to this deviation. This impacts the shell-core race to carbon ignition and also hints at a possible sensitivity to the initial WD core temperature, which depends on the WD age at the time accretion starts.

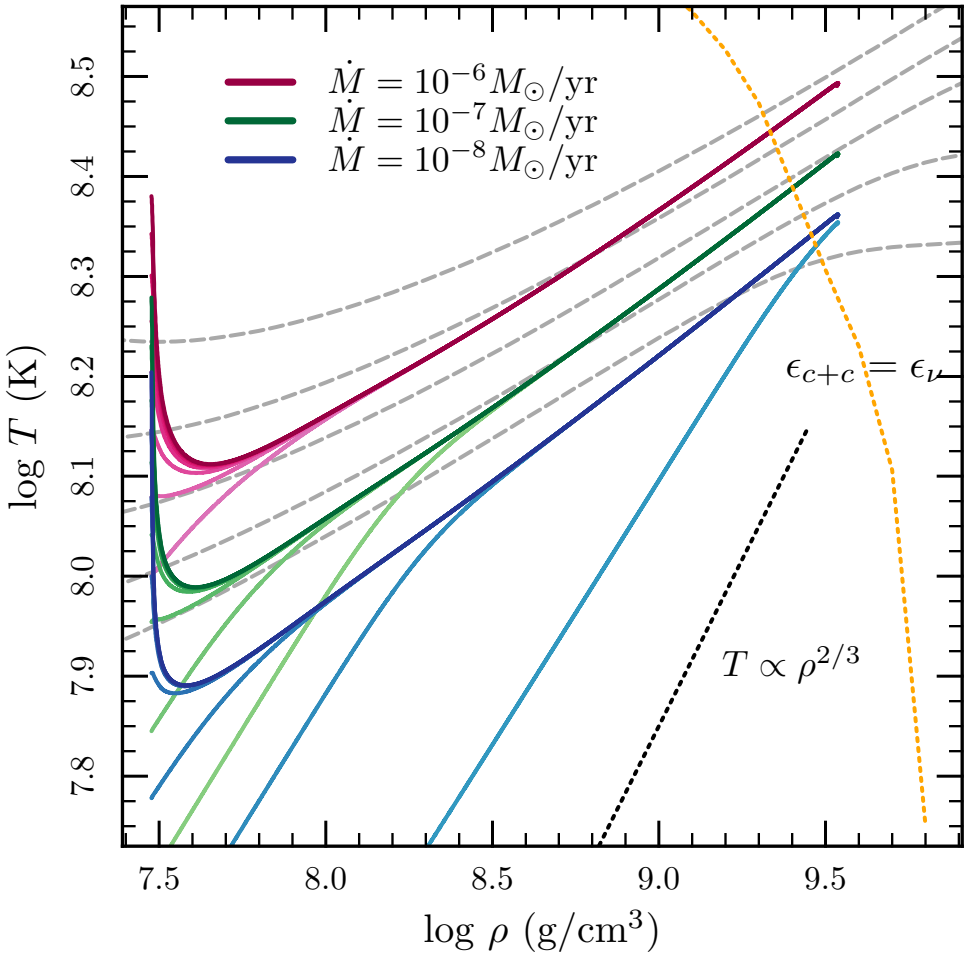

Figure 3.10 Evolution of core of WD given different $\dot{M}$'s and starting core temperatures. The grey dashed lines are lines of constant neutrino cooling timescales from 3×10^4 to 3×10^6 years, spaced logarithmically, from top to bottom. As always, the dotted line represents $\epsilon_{\mathrm{c+c}} = \epsilon_\nu$ for $\{X_{C12} = 0.5, X_{O16} = 0.5\}$.

It is when the the neutrino cooling timescale, $t_\nu = c_p T/\epsilon_\nu$, approaches the compressional timescale $t_{\mathrm{comp}} = (d \ln \rho/dt)^{-1}$ that the core no longer evolves adiabatically. To derive the resulting relations more rigorously, we start by writing the entropy change, ds, in the form of equation A6 of Townsley & Bildsten (2004),

$$ds = \frac{k_B}{\mu m_p}(a\, d\ln T - b\, d\ln \rho), \tag{3.3}$$

where k_B is Boltzmann's constant, μ is the mean molecular weight, m_p is the proton mass, $a = 1.22 + 0.41\Gamma^{1/3}$, $b = 0.91 + 0.14\Gamma^{1/3}$, and $\Gamma = (Ze)^2/akT$ where a is the ion separation, and we set $Z = 6.857$ for an equal (by mass) mix of carbon and oxygen. We divide each side by dt and multiply by T to obtain

$$-\epsilon_\nu(\rho, T) = T\frac{ds}{dt} = \frac{k_B T}{\mu m_p}\left(a\frac{d\ln T}{dt} - b\frac{d\ln \rho}{dt}\right), \tag{3.4}$$

and then expand the second term on the right as

$$\frac{d\ln \rho}{dt} = \frac{d\ln \rho}{d\ln M}\frac{d\ln M}{dt}. \tag{3.5}$$

We use `MESA` to compute the steeply rising value of $n = d\ln\rho/d\ln M$ as $M \to M_{\rm Ch}$. For a constant $\dot{M}$, we can then solve the resulting differential equation for $T(t)$ given an initial temperature.

This results in evolutionary trajectories in the $\rho - T$ plane that are shown in Figure 3.10 to converge to a common $\rho - T$ line when neutrino cooling is dominant. This common line is one where the neutrino cooling timescale equals that of compression (shown as light grey curves in Figure 3.10). Cold initial conditions adiabatically rise in temperature until meeting the $\dot{M}$-dependent trajectory, whereas hot initial conditions will cool to reach the attractor. Hence, a range of initial conditions will converge to the same trajectory given the same $\dot{M}$. The same convergence of the evolution of the central temperature and density was shown in Paczyski (1971) in the context of intermediate mass AGB stars. Paczyski (1971), however, only show one convergence line due to the core mass-luminosity relation. Much colder cores with lower accretion rates never reach regimes where neutrino cooling is strong enough to cause convergence, and so behave differently.

3.4 HR Diagrams

We now explore the observability of these systems by following their trajectories through the HR diagram. We show the evolution of the donors in Figure 3.11, starting from ignition of helium in the core in the lower right-hand corner, and evolving to higher temperatures and luminosities along the helium MS. Once helium in the core has been exhausted, shown by the left-most (hottest) point in the evolution, the envelopes of the helium donors begin to expand due to helium shell burning, causing $T_{\rm eff}$ to decrease and the luminosity to increase. The rise in luminosity is halted by the start of mass transfer as the helium stars' envelopes expand into their RLs. The position of the donors in the HR diagram when the carbon ignites falls right in the most heavily populated region of Figure 4 of Wang et al. (2014), which plots distribution of donor stars in systems that achieved a core ignition through the helium star channel.

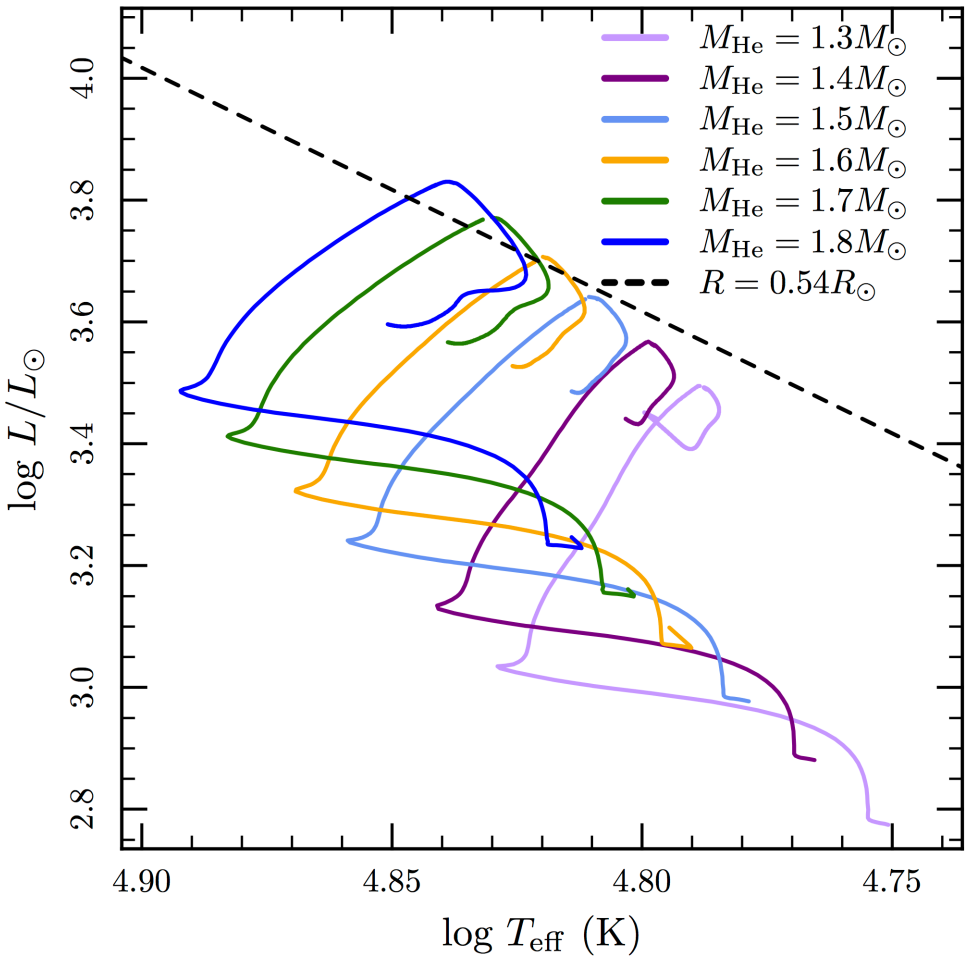

Figure 3.11 HR diagram of the donors of masses $1.3 - 1.8M_\odot$. Evolution starts with core helium ignition in the lower, right-hand corner, evolves through to core helium exhaustion at the left-most (hottest) point, then expands and brightens with shell helium burning, and reaches the brightest point when mass transfer starts. A line of constant radius near the initial Roche lobe radius for these systems, $R = 0.54R_\odot$, is shown by the black dashed line.

With initial orbital periods ($P_{\rm orb,0}$) that are longer (shorter), the donors will have more (less) time and room to expand their envelopes until RLOF, leading to donor stars that are redder (bluer) and brighter (dimmer) when carbon ignites in the WD. This suggests a diagonal patch in the HR diagram for the state of donors. Wang et al. (2009) and Liu et al. (2010) find systems in which the donor star donated enough helium that

the helium shell burning layer starts becoming exposed, leading to a rapid evolution to higher temperatures and luminosites. This requires systems with either lower mass donors, which will fall below the steady helium burning mass transfer rates, or lower mass WDs, which means that the WD will spend a longer time accreting and thus has a much higher likelihood of experiencing a carbon shell ignition before a core ignition.

We also show, in Figure 3.12, the evolution of the WD accretors in the HR diagram. Due to the steady helium burning on the surface of the WDs, they are hot and bright enough to be classified as supersoft X-ray sources (SSS) (Kahabka & van den Heuvel, 1997; Iben & Tutukov, 1994b). The WDs begin their evolution in the middle of Figure 3.12 at about $\log T_{\rm eff} = 5.75$ and $\log L/L_{\odot} = 4.4$, but will be obscured by an optically thick wind until they reach the red marker, where mass transfer rates have decreased below the upper steady helium burning boundary and the transfer efficiency reaches unity. For the systems with the lowest mass donors ($M_{\rm He} = 1.3 - 1.5 M_{\odot}$), the mass transfer rates drop below the steady helium burning range near the end of their evolution. The range of oscillations of $T_{\rm eff}$ during the mild helium oscillations is less than a factor of two. The luminosity, however, changes by about an order of magnitude, on the timescale of $\approx$5 years, so this should be visible to observers.

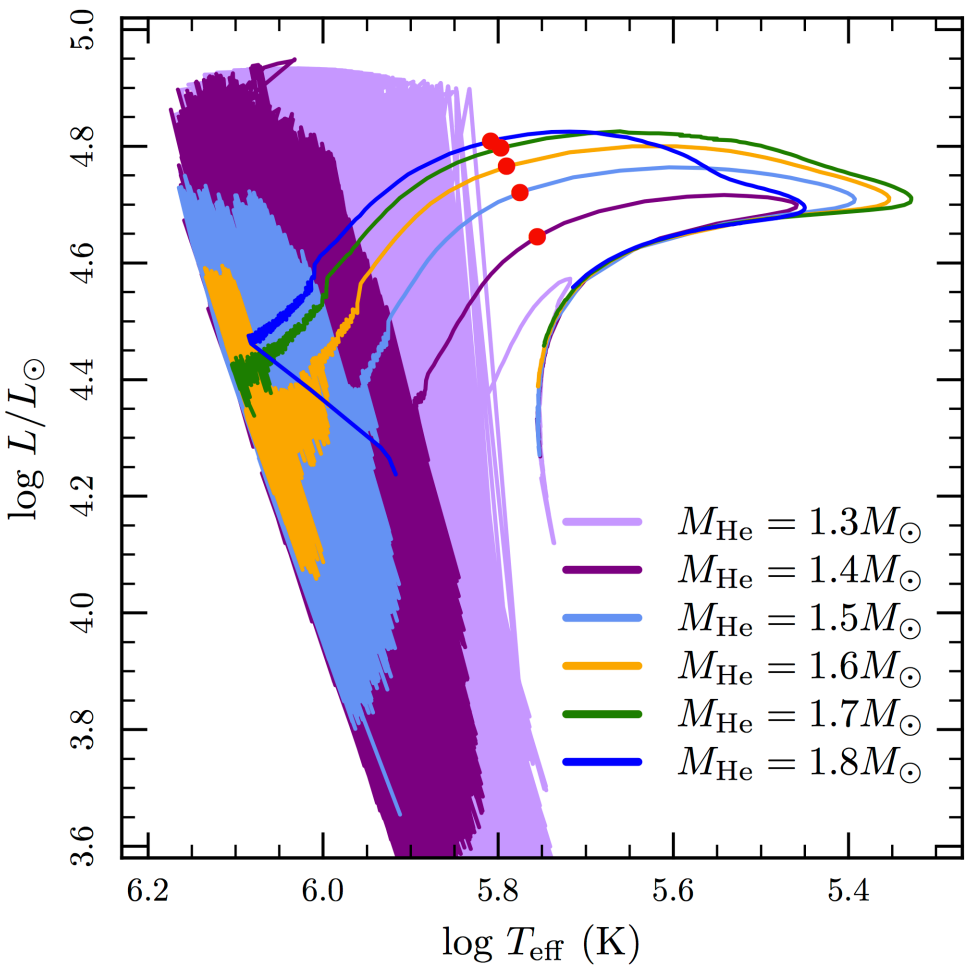

Figure 3.12 HR diagram of the WD accretors given six different donor masses, corresponding to the same colored lines in Figure 3.11. Evolution started in the middle of the plot, moves right (hotter) then left (cooler). The red markers denote where the optically thick wind phase ends. The WDs with the $1.5 - 1.6M_\odot$ helium star donors enter into mild helium oscillations (no mass loss) at the end of their evolution, while the WDs with the $1.3 - 1.4M_\odot$ helium star donors will experience oscillations strong enough to remove mass.

Note that in all six models, by the time the carbon ignites, the optically thick wind has been inactive for tens of thousands of years, meaning that there should be no nearby circumstellar material.

3.5 Lower Mass Binary Case Leading to WD Mergers

We now test our prescriptions against the calculations done by Ruiter et al. (2012) in their example case in section 2.3. They start with 5.65 and $4.32 M_{\odot}$ MS stars separated by 37 $R_{\odot}$. After the primary evolves to become a C/O WD and engages in a common envelope with the secondary as is exhausts core hydrogen, they are left with a $0.84 M_{\odot}$ WD and $1.25 M_{\odot}$ helium star separated by $1.74 R_{\odot}$. These are the parameters we initialize, with the mass transfer history shown in Figure 3.13. We model the system until the He star loses contact and the stars spiral inward due to GWR and begin to merge. When the mass of the helium layer on the donor decreases down to $7 \times 10^{-3} M_{\odot}$, the helium burning layer becomes too weak to support an extended convective envelope and the surface contracts below the RL. Compared to Ruiter et al. (2012), we calculate less system mass loss, resulting in slightly more massive components, $M_{\rm WD} = 1.21 M_{\odot}$, $M_{\rm He} = 0.81 M_{\odot}$, compared to $M_{\rm WD} = 1.19 M_{\odot}$, $M_{\rm He} = 0.77 M_{\odot}$ for Ruiter et al. (2012). This also leads to a shorter merger time, 625 Myr for our work and 1130 Myr for Ruiter et al. (2012), after loss of contact.

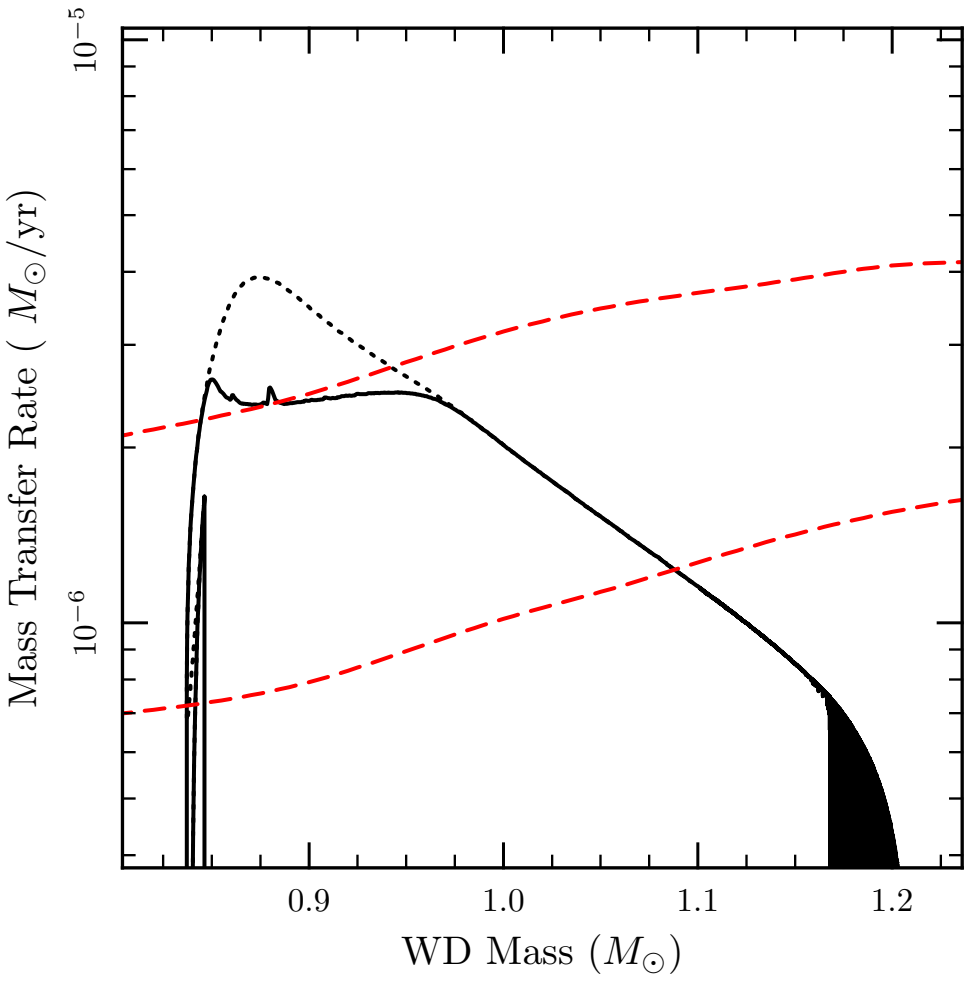

Figure 3.13 The mass transfer history for the low mass case. The WD accretes within the steady helium burning range until $M_{\rm WD} > 1.09 M_\odot$, but only stops conserving mass when $M_{\rm WD} > 1.16 M_\odot$, and grows to $M_{\rm WD} = 1.21 M_\odot$.

As Ruiter et al. (2012) used the accumulation efficiencies of Kato & Hachisu (2004) for helium accretion onto WDs, this serves as an additional comparison (along with Figure 3.7) to the mass transfer prescriptions of Kato & Hachisu (2004). This shows that for WDs in the $1.2 M_\odot$ range the Kato & Hachisu (2004) prescription match our ending masses to with a few per cent, but somewhat larger discrepancies appear for masses closer to $M_{\rm Ch}$ (Figure 3.7).

3.6 Conclusions

We ran binary simulations using `MESA` for WD + Helium star systems, calculating stellar structure equations for both stars simultaneously, along with the binary parameters that take into account their interaction through mass transfer. The systems we study include $1.0M_{\odot}$ C/O WDs in 3 hour orbital periods ($P_{\rm orb}$) with helium stars with masses $1.3M_{\odot} \leq M_{\rm He} \leq 1.8M_{\odot}$. This configuration allows the steady growth of the WD core mass via steady helium burning on the WD surface. At mass transfer rates above the steady helium burning range, we assume an optically thick wind that ejects all the donated mass above the maximum steady helium burning rate from the system. Below the steady helium burning range the WD begins mild helium oscillations.

During the initial turn-on of mass transfer, the WD surface is initially cold and must be heated through several helium flashes until steady helium burning can begin. Using Figure 10 of Shen & Moore (2014), we conclude that all the first bursts on the $1.0M_{\odot}$ WD models are well below the detonation threshold, but the first burst on the lower mass $0.84M_{\odot}$ WD may support a detonation.

We assume that the mass that is lost from the system takes with it the specific angular momentum of the accretor, which is justified as long as the wind speeds exceed $v_{\rm wind} \gtrsim 1000$km/s. We note here that some orbital angular momentum may be lost in spinning up the accreting WD, which we did not explore in this study. During the optically thick wind phase, however, the accretion stream coming through L1 may not be able to form a disk in the extended RG envelope around the WD, and may become part of that envelope once it reached a depth at which the surrounding density matches the stream density, thus preventing any angular momentum transfer to the WD. This way, the angular momentum of the accretion stream gets fed back into the orbit through tidal effects on the extended envelope. We leave this subject, as well as internal angular

momentum transport, to future studies.

The systems with the lowest mass donors ($M_{\rm He} = 1.3 - 1.4 M_{\odot}$) begin mild helium burning oscillations before the WD reaches $M_{\rm Ch}$. Systems with $1.3 M_{\odot} \lesssim M_{\rm He} \lesssim 1.7 M_{\odot}$ experience a core ignition in a $M_{\rm Ch}$ WD. Systems with $M_{\rm He} \gtrsim 1.8 M_{\odot}$ experience a shell ignition of carbon in the helium burning ashes. The corresponding maximum helium star donor mass for lower initial mass WDs might be even lower, given that they must spend more time accreting to grow to $M_{\rm Ch}$, but the birthrate from those systems, from Table 1 in Wang et al. (2009), is negligible compared to systems with higher mass WDs. This shell ignition is non-explosive and will lead to a thin carbon burning front that will propagate through the C/O WD all the way to the center, converting a C/O WD into an O/Ne WD (Nomoto & Iben, 1985; Saio & Nomoto, 1985; Timmes et al., 1994; Saio & Nomoto, 1998). Without any carbon in the center, when the WD mass nears $M_{\rm Ch}$, electron captures onto ^{24}Mg and ^{20}Ne will remove pressure support from the core, resulting in an accretion induce collapse (AIC), leaving behind a neutron star (Miyaji et al., 1980; Schwab et al., 2015). In future studies, we intend to run simulations over a large range of initial orbital periods and WD masses to determine the real upper boundary for the He star donor mass that allows a core ignition in the $\log P_{\rm orb,0} - M_{\rm He}$ plane in Figure 7 in Wang et al. (2009). In addition to changing the expected SN Ia rate, this would yield an AIC rate for this new channel (Brooks et al. 2016 in preparation). This would be in addition to the rate expected from the initially more massive, presumably O/Ne WD accretors.

Systems with $M_{\rm WD} \gtrsim 1.1 M_{\odot}$, although assigned a much higher contribution to the SNe Ia birthrate than their lower mass WD counterparts, are not likely to be C/O WDs (Nomoto, 1984; Timmes et al., 1994; Ritossa et al., 1996; García-Berro et al., 1997). Wang et al. (2014) explore systems with so-called "hydrid" C/O/Ne WDs that experience an off-center carbon ignition during WD formation that was quenched by convective boundary

mixing and left an unburnt carbon oxygen core of up to $0.3M_{\odot}$, surrounded by an O/Ne mantle of equal or greater mass (Denissenkov et al., 2013; Chen et al., 2014; Denissenkov et al., 2015) (This opens the possibility that carbon shell ignitions on C/O WDs may experience flame quenching before converting the entire core into O/Ne). This thick O/Ne mantle would prevent carbon flames that ignited in the ashes from steady helium burning from reaching the unburnt core carbon. Therefore, carbon shell ignitions, like the one experienced by the WD with the $M_{\rm He} = 1.8M_{\odot}$ in this study, will not prevent hybrid C/O/Ne WDs from achieving core carbon ignition. It is unlikely, however, that this sort of WD can lead to a normal SN Ia because a deflagration ignited in the C/O core cannot transition into a detonation in the O/Ne mantle easily because the critical mass for a detonation of an O/Ne mixture is much larger than that of carbon (Denissenkov et al., 2015). These hybrid C/O/Ne WDs are more likely to lead to the subclass SN Iax (Fink et al., 2013; Kromer et al., 2015).

We also found that, due to rapid neutrino cooling in warm and dense cores, evolution of the central temperature and density will converge to accretion-rate dependent trajectories until ignition, given a high enough initial central temperature.

Chapter 4

Convection Destroys the Core/Mantle Structure in Hybrid C/O/Ne White Dwarfs

A hybrid C/O/Ne white dwarf (WD) – an unburned C/O core surrounded by an O/Ne/Na mantle – can be formed if the carbon flame is quenched in a super-AGB (SAGB) star or white dwarf merger remnant. We show that this segregated hybrid structure becomes unstable to rapid mixing within 2,000 years of the onset of WD cooling. Carbon burning includes a weak reaction that removes electrons, resulting in a lower electron-to-baryon ratio ($Y_{\rm e}$) in the regions processed by carbon burning compared to the unburned C/O core, making the O/Ne mantle denser than the C/O core as the WD cools. This is unstable to efficient mixing. We use the results of `MESA` models with different size C/O cores to quantify the rate at which the cores mix with the mantle as they cool. In all cases, we find that the WDs undergo significant core/mantle mixing on timescales shorter than the time available to grow the WD to the Chandrasekhar mass ($M_{\rm Ch}$) by accretion. As a result, hybrid WDs that reach $M_{\rm Ch}$ due to later accretion will have lower central carbon

fractions than assumed thus far. We briefly discuss the implications of these results for the possibility of Type Ia supernovae from hybrid WDs.

In models of $M \gtrsim 7.2 M_{\odot}$ SAGB stars, carbon ignites off-center, triggering a carbon flame that can in principle propagate all the way to the center, converting the core into O/Ne/Na (Nomoto & Iben, 1985; Timmes et al., 1994; García-Berro et al., 1997; Saio & Nomoto, 1998). However, if mixing at convective boundaries is sufficiently effective, the carbon flame may be quenched a significant distance from the core, resulting in a hybrid C/O/Ne WD (Doherty et al. 2010; Denissenkov et al. 2013; Chen et al. 2014; Wang et al. 2014; Denissenkov et al. 2015; Farmer et al. 2015; see, however, Lecoanet et al., 2016). These hybrid C/O/Ne models consist of an unburned C/O core surrounded by a O/Ne/Na mantle. Hybrid models have been utilized in 2D and 3D hydrodynamic codes to study the thermonuclear SNe they produce and to compare synthesized light-curve and spectra to observations of peculiar SNe Ia (Kromer et al., 2015; Willcox et al., 2016; Bravo et al., 2016).

However, all of these authors assumed that the compositional structure was fixed as the WD cools. In this Letter, we show that there is significant mixing between the C/O core and the overlying O/Ne/Na mantle. The mixing is driven by the lower electron-to-baryon ratio, $Y_{\rm e}$, in the O/Ne/Na mantle that has been processed by carbon burning. This $Y_{\rm e}$ gradient corresponds to a heavy fluid on top of a light fluid and rapidly (over $\sim$ kyrs) becomes unstable to convection as the WD cools towards an isothermal configuration.

In §4.1 we discuss the nuclear reaction in carbon burning that reduces $Y_{\rm e}$. In §4.2 we derive the criterion for a $Y_{\rm e}$ gradient to be unstable to convection and compare to our numerical `MESA` models. We discuss our `MESA` models in §4.3 and explain our results in §4.4. We finish with our conclusions and implications in §4.5, highlighting that this mixing will be complete by the time any accreting WD reaches $M_{\rm Ch}$.

4.1 Carbon burning lowers $Y_{\rm e}$

Material processed by carbon burning will have a lower electron-to-baryon ratio, $Y_{\rm e}$. The change in $Y_{\rm e}$ has been previously discussed in the context of the carbon simmering phase in Type Ia supernova progenitors (Piro & Bildsten, 2008; Chamulak et al., 2008). Carbon burning proceeds via

$$^{12}{\rm C} + {}^{12}{\rm C} \rightarrow \begin{cases} {}^{20}{\rm Ne} + \alpha & (0.56) \\ {}^{23}{\rm Na} + p & (0.44) \ , \end{cases} \tag{4.1}$$

where the numbers in parentheses are the branching fractions for the relevant temperatures (Caughlan & Fowler, 1988). The free proton is then rapidly captured, with most captures occurring onto either ^{12}C or ^{23}Na.

When the proton is captured onto ^{12}C, the reaction ^{12}C(p,γ)^{13}N is followed by the beta-decay ^{13}N(e^-,ν_e)^{13}C, which reduces the electron fraction. The ^{13}C later captures the α-particle generated from carbon-burning, ^{13}C(α,n)^{16}O, producing a free neutron. This free neutron will capture onto ^{12}C, creating ^{13}C. Thus, the net result (approximating the branching fractions as equal) is that for every six ^{12}C nuclei burned, one proton is converted into a neutron (Piro & Bildsten, 2008). However, if the proton is captured onto ^{23}Na, the proton-capture reaction ^{23}Na(p,α)^{20}Ne is followed only by an α-capture. Since no weak reactions occur in this channel, the net result is no change in $Y_{\rm e}$.

The thermally-averaged cross-section for proton captures onto ^{23}Na is $\approx$2 times larger than that of ^{12}C (REACLIB; Cyburt et al., 2010). At the relevant densities of $\rho \approx 10^6$ g cm^{-3}, screening effects enhance the ratio of proton capture rates relative to those of ^{12}C by a factor of $\approx$1.5. To demonstrate that the competition of these two proton capture channels quantitatively explains our more detailed `MESA` results, we use a simple model that assumes equal branching fractions in equation (4.1) and assumes that when

$X_{\rm C12} > 3X_{^{23}\rm Na}$ all protons capture on to ^{12}C and when $X_{\rm C12} < 3X_{^{23}\rm Na}$ all protons capture on to ^{23}Na (meaning its consumption rate exactly matches its production rate). For complete carbon burning, this simple model gives values for the ^{23}Na abundance and total neutronization that agree with our `MESA` models. This results in a factor of $\approx$2 less neutronization than suggested by the counting arguments of Piro & Bildsten (2008), because approximately half of the protons produced in equation (4.1) are captured by ^{12}C and half by ^{23}Na when the burning is complete. Therefore, a change in the electron-to-baryon ratio due to complete burning is

$$\Delta Y_{\rm e} \approx 0.5 \left(\frac{\Delta X(^{12}{\rm C})}{72} \right) \quad . \tag{4.2}$$

In our models, the initial carbon mass fraction is 0.345 and the carbon burns completely. Consistent with equation (4.2), the difference in $Y_{\rm e}$ between burned and unburned material is $\Delta Y_e = -0.00235$.

4.2 Convective Instability Criterion

The reduction in $Y_{\rm e}$ due to carbon burning creates a sharp $Y_{\rm e}$ gradient between burned and unburned material. Since the ashes above are much hotter than the unburned material below, this configuration is stable against convection. However, if the flame is extinguished before reaching the center, the stabilizing thermal gradient vanishes under the action of neutrino cooling and electron conduction, while the $Y_{\rm e}$ gradient remains. By coincidence, the $\Delta Y_{\rm e}/Y_{\rm e}$ is the same order of magnitude as the ratio of thermal energy to the Fermi energy. Performing a simple buoyancy calculation by adiabatically perturbing a fluid element in an isothermal configuration of a degenerate, non-relativistic electron gas, and an ideal ion gas with average ion charge $\bar{Z}$ gives the convective instability criterion

as

$$\frac{d\ln Y_{\rm e}}{d\ln P} > \frac{k_B T}{\gamma \bar{Z} E_F} \ , \tag{4.3}$$

where E_F is the electron Fermi energy, and γ is the adiabatic exponent. Therefore, as the WD cools, the region with a $Y_{\rm e}$ gradient is destined to convect.

A more accurate convective stability criterion can be determined from the Brunt-Väisälä frequency, which is

$$N^2 = \frac{g^2 \rho}{P} \frac{\chi_T}{\chi_\rho} \left(\nabla_{\rm ad} - \nabla_T + B\right) \tag{4.4}$$

where ∇_T and $\nabla_{\rm ad}$ are the actual and adiabatic temperature gradients with respect to the pressure, B is the term that takes into account the effect of composition gradients (see eq. 6 in Paxton et al., 2013), g is the local gravitational acceleration, ρ and P are the density and total pressure, respectively, and $\chi_Q = \partial \ln P / \partial \ln Q$, where the choices for Q are $\rho, T, \bar{A}$, or $\bar{Z}$, and the remaining three variables are held fixed. For an equation of state where the influence of the composition can be fully specified by the mean ion weight, $\bar{A}$, and the mean ion charge, $\bar{Z}$,

$$B = -\frac{1}{\chi_T} \left[\chi_{\bar{A}} \frac{d\ln \bar{A}}{d\ln P} + \chi_{\bar{Z}} \frac{d\ln \bar{Z}}{d\ln P} \right] \ . \tag{4.5}$$

In order to analytically evaluate the partial derivatives in equation (4.5), we assume a simple form for the equation of state consisting of fully-degenerate electrons, an ideal gas of ions, and the Coulomb pressure in the Wigner-Seitz approximation. That is, we take $P_{\rm tot} = P_{\rm ele} + P_{\rm ion} + P_{\rm cou}$, where $P_{\rm ele} = P_0 \left(\rho Y_{\rm e}/\rho_0\right)^\gamma$, $P_{\rm ion} = \rho k_B T/(m_p \bar{A})$, and $P_{\rm cou} = -3\Gamma P_{\rm ion}/10$. The Coulomb coupling parameter $\Gamma = (\bar{Z}e)^2/(a_i k_B T)$ where $a_i = (4\pi\rho/3m_p\bar{A})^{-1/3}$.

Plugging in these definitions, equations (4.4) and (4.5) imply that the gradient in

electron fraction corresponding to the neutral stability condition, $N^2 = 0$, is

$$\frac{d\ln Y_{\rm e}}{d\ln P} = \frac{\chi_T\left(\nabla_{\rm ad} - \nabla_T\right)}{\gamma\left(1-\epsilon+\frac{3}{10}\Gamma\epsilon\right) - \frac{3}{5}\Gamma\epsilon - \left(1+\frac{1}{5}\Gamma\right)\epsilon\frac{d\ln\bar{A}}{d\ln Y_{\rm e}}} \ . \tag{4.6}$$

where for convenience we define $\epsilon = P_{\rm ion}/P_{\rm tot}$. Gradients steeper than equation (4.6) are unstable to convection. Note that the critical gradient corresponding to $N^2 = 0$ evolves as ∇_T evolves within the WD. We use equation (4.6) to compute the neutral stability lines shown in §4.3 and §4.4.

4.3 Rapid Onset and Modeling of Convection

We generated models of C/O/Ne hybrid WDs using the published set of controls from Farmer et al. (2015) and `MESA` version 8118 (Paxton et al., 2011, 2013; Paxton et al., 2015). These models have C/O cores of mass $0.24, 0.40$, and $0.55 M_\odot$ and total masses of $1.12, 1.09$, and $1.07 M_\odot$, respectively. The stars producing these WDs had zero-age main sequence masses of $7.2 - 7.5 M_\odot$. The H rich envelopes are removed once the inward-moving carbon flame dies, simulating a thermally pulsing AGB phase, or interaction with a binary companion. We then restart these models with all the same controls except all forms of overshooting and thermohaline mixing turned off.

We started by running a `MESA` simulation with the Schwarzschild criterion for convection, which ignores compositional gradients, to show that the square of the total Brunt-Väisälä frequency (equation 4.4) becomes negative as the WD cools (see Figure 4.1). The regions that become unstable to convection ($0.28 - 0.52 M_\odot$) coincide with the steepest portion of the $Y_{\rm e}$ profile, shown by the dotted green curve in Figure 4.1. Cooling erases the stabilizing temperature gradient, and hence mixing will begin, within a mere 1.6 kyr of the formation of the hybrid WD, as shown by the blue profile in Figure 4.1 at

$\log T_c = 8.294$. The cooling is dominated by neutrino emission until $\log T_c \approx 7.8$.

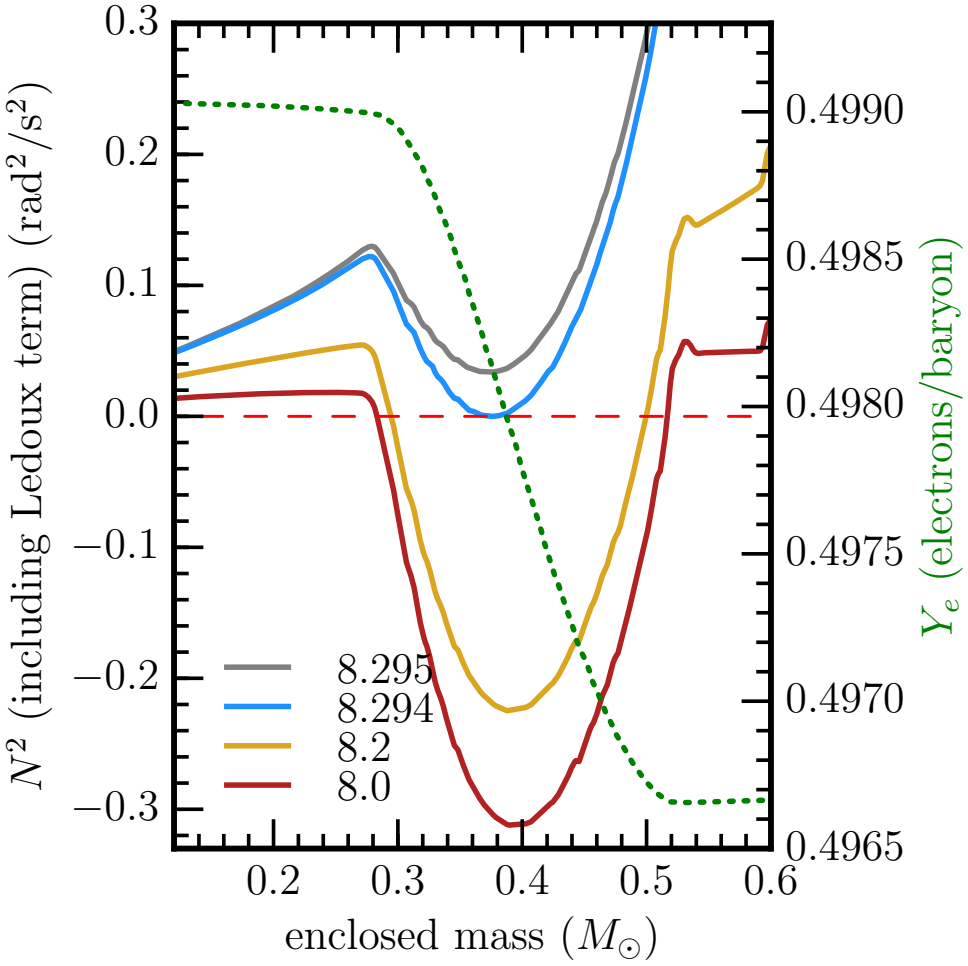

Figure 4.1 The Brunt-Väisälä frequency squared (left y-axis) and Y_e profile (right y-axis) for the `MESA` model with a $0.40 M_\odot$ C/O core ($1.09 M_\odot$ total mass) in which the Schwarzschild criterion for convection is used, so convection driven by the Y_e profile is inhibited. The plotted Brunt-Väisälä frequency includes the Ledoux term. The profiles are labelled by the log of their central temperatures. As the temperature decreases and the density increases, N^2 becomes more negative, and therefore more unstable to convection. The blue curve at $\log T_c = 8.294$ is the time at which convection would begin, only 1600 yrs after the formation of the hybrid WD. The cooling ages to $\log T_c = 8.2, 8.0$ are 13.5 kyr and 330 kyr, respectively.

Figure 4.1 highlights that the WD rapidly evolves towards convective instability, which can in principle mix material on the much shorter dynamical timescale. Given

that this dynamical mixing timescale is so much faster than the timescale on which the WD evolves due to cooling, we expect that convection will (as usual) lead to nearly zero Brunt-Väisälä frequency. Thus, for our assumed thermal evolution, we expect convection will mix the composition efficiently enough to keep the actual $Y_{\rm e}$ gradient extremely close to neutral stability at all times.

Evolving the hybrid WD models using the standard MESA MLT implementation leads to severe numerical difficulties. When taking a timestep, as the `MESA` solver iterates to find the next model, some zones alternate between being convective and non-convective. This corresponds to the temperature gradient (∇_T) at cell faces switching between the adiabatic temperature gradient ($\nabla_{\rm ad}$) and the radiative temperature gradient ($\nabla_{\rm rad}$). These are significantly different, since the temperature profile is highly stable against convection and only being destabilized by the $Y_{\rm e}$ gradient. As a result, the solver fails to find models that satisfy its "`dlnTdm`" equation (eq. 8 of Paxton et al. 2011). In order to circumvent this issue, we set the `MESA` control `mlt_gradT_fraction = 0`, which sets ∇_T in convective regions to $\nabla_{\rm rad}$ instead of $\nabla_{\rm ad}$. The choice to set the temperature gradient to the radiative gradient in convection zones is appropriate when the convection is thermally inefficient and the energy flux is dominated by conduction. Thus our choice assumes that the convection does not significantly modify the thermal evolution of the WD.

`MESA` treats mixing, including convective mixing, as a diffusive process (Paxton et al., 2011). When using standard MLT, `MESA` sets the diffusion coefficient to be $\frac{1}{3}v_{\rm c}\Lambda$, where $v_{\rm c}$ is the convective velocity and Λ is the mixing length. Our models consistently exhibit convective regions that span only a few cells and thus are much smaller than a pressure scale height. Using a mixing length of order the pressure scale height likely overestimates the mixing, but limiting the mixing length to the size of the convective region introduces an undesired dependence of the mixing on the numerical resolution. In order to circum-

vent this issue, we set the diffusive mixing coefficient in convectively unstable zones to be proportional to the thermal diffusion coefficient, that is $D_{\rm mix} = \beta D_{\rm thermal}$ with β a constant. The choice of $D_{\rm thermal}$ as the reference diffusivity allows us to ensure that the mixing remains more rapid than the thermal evolution. Physically, we expect values of $\beta \gg 1$ to approach the correct answer, representing the fact that convection can mix material on timescales much shorter than the thermal timescale (which is the timescale on which the convective regions are created; see Fig. 4.1).

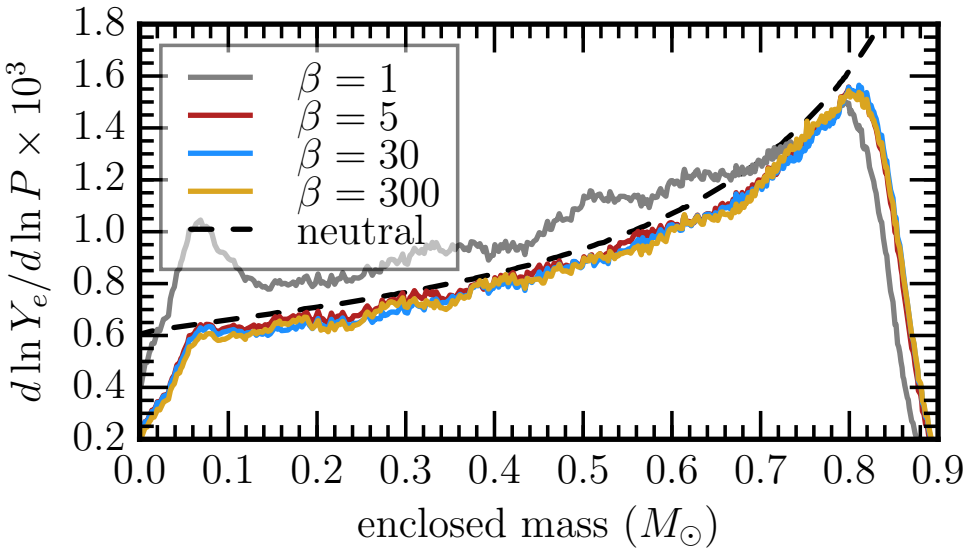

Figure 4.2 Profiles of $d \ln Y_e / d \ln P$ for $\log T_c = 8.2$, compared to the neutrally buoyant $Y_{\rm e}$ gradient (black dashed curve, eq. 4.6) for the `MESA` model with a $0.40 M_\odot$ C/O core ($1.09 M_\odot$ total mass). The solid curves show profiles for `MESA` models with the full Ledoux convection criterion and different choices of $\beta = D_{\rm mix}/D_{\rm thermal}$ (see §4.3). The profile for $\beta = 1$ underestimates mixing compared to the neutral buoyancy curve. The profiles for $\beta = 5, 30, 300$ are similar, and consistent with the expected neutral stability curve.

We compare the resulting composition profiles for different choices of β in Figure 4.2. While the choice of $\beta = 1$ underestimates the mixing compared to neutral buoyancy as expressed by equation (4.6), shown by the grey curve in Figure 4.2, the choices of $\beta = 5, 30$, and 300 yield nearly identical results and reach the neutral buoyancy condition

derived in §4.2. This supports our claim that the Y_e gradients should match those of neutral stability (eq. 4.6), as long as the mixing timescale is shorter than the thermal timescale. We also found comparable results using alternative ways of controlling the mixing in `MESA`, such as using a mixing length alpha parameter that varied in proportion to the thermal timescale of the WD. The rest of our results employ $D_{\rm mix} = \beta D_{\rm thermal}$ with $\beta = 5$.

4.4 Results for a range of Core Masses and Thermohaline Mixing

Figure 4.3 shows the composition evolution of our `MESA` model with an initial $0.4 M_\odot$ C/O core including the effects of convective mixing during the subsequent thermal evolution (but not including thermohaline mixing). As the WD cools, the Y_e gradients (solid lines) become shallower and shallower, comparable to what we analytically expect given the the neutral buoyancy gradients (dashed lines). Figure 4.4 shows the carbon mass fractions at these same times, demonstrating that the C/O core and O/Ne/Na mantle rapidly mix as the WD cools.

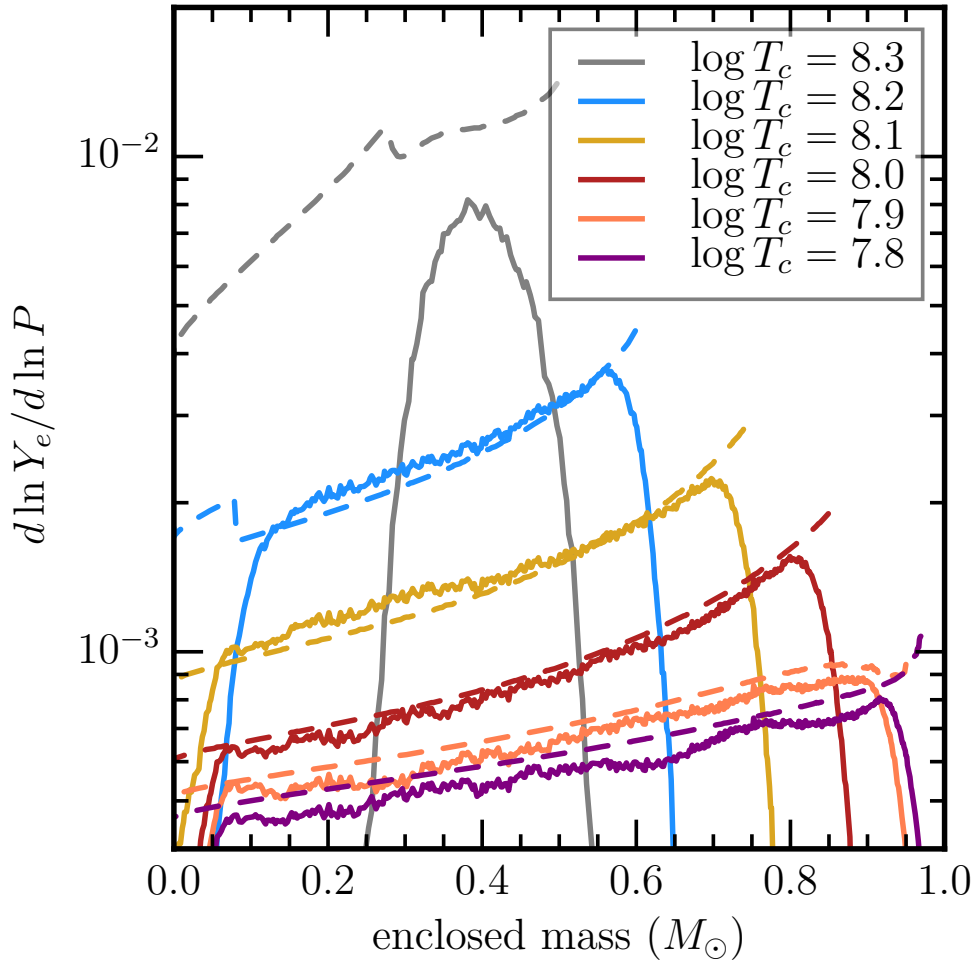

Figure 4.3 Profiles of $d \ln Y_e / d \ln P$ as a function of time (labeled by the central temperature) for the MESA model with an initial C/O core mass of $0.4 M_\odot$ (solid curves), compared to the neutrally buoyant Y_e gradient (dashed curve, eq. 4.6). The dashed neutral buoyancy lines are cropped to show only the regions where convective mixing has occurred. As the WD cools and becomes isothermal, the core becomes increasingly mixed by convection driven by the unstable composition gradient.

Figure 4.5 shows the ^{12}C mass fraction profiles of three models with different initial C/O core masses before any mixing (solid curves), when $\log T_c = 7.8$ (dotted curves), and when $\log T_c = 7.5$ (dashed curves).

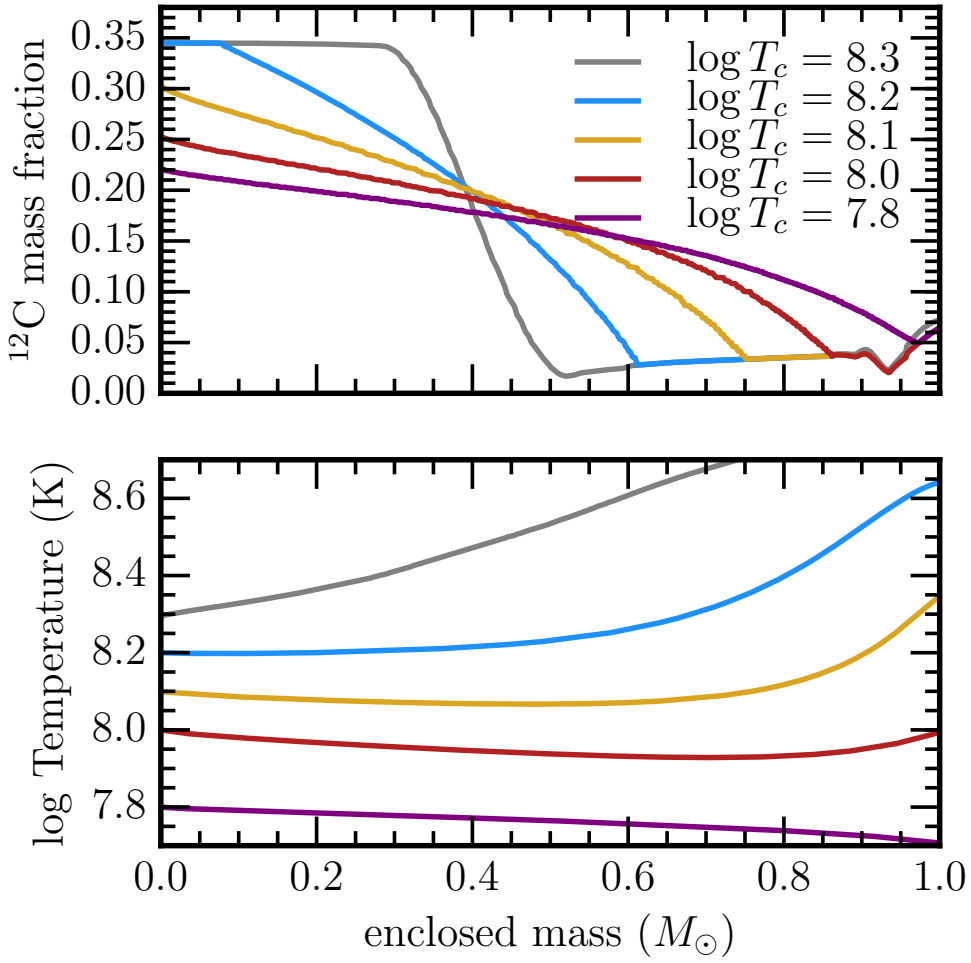

Figure 4.4 Top panel: Carbon mass fractions as a function of time (labeled by central temperature), for the `MESA` model with an initial C/O core mass of $0.4 M_\odot$. As the WD cools and becomes isothermal, the core becomes increasingly well mixed and the central carbon fraction decreases. Bottom panel: Temperature profiles at the same time as the profiles in the top panel.

All of the results discussed above are based on models run without including the effects of thermohaline mixing. As the WD evolves towards an approximately isothermal profile, mixing by convection alone would leave behind a finite Y_e gradient given by setting $\nabla_T = 0$ in equation (4.6). However, such a composition gradient is unstable to thermohaline convection. Therefore, additional mixing will continue to occur. Prescriptions for thermohaline mixing (Kippenhahn et al., 1980; Brown et al., 2013) remain

somewhat uncertain, however, leading to more substantial uncertainties in the resulting composition profile. As illustrative examples, we carried out `MESA` calculations with `thermohaline_option = 'Kippenhahn'` and `thermohaline_coeff = 1`. This diffusion coefficient proposed by Kippenhahn et al. (1980) as written in eq. (14) of Paxton et al. (2013), with a dimensionless, multiplicative efficiency factor of `thermohaline_coeff`, which we set to 1.

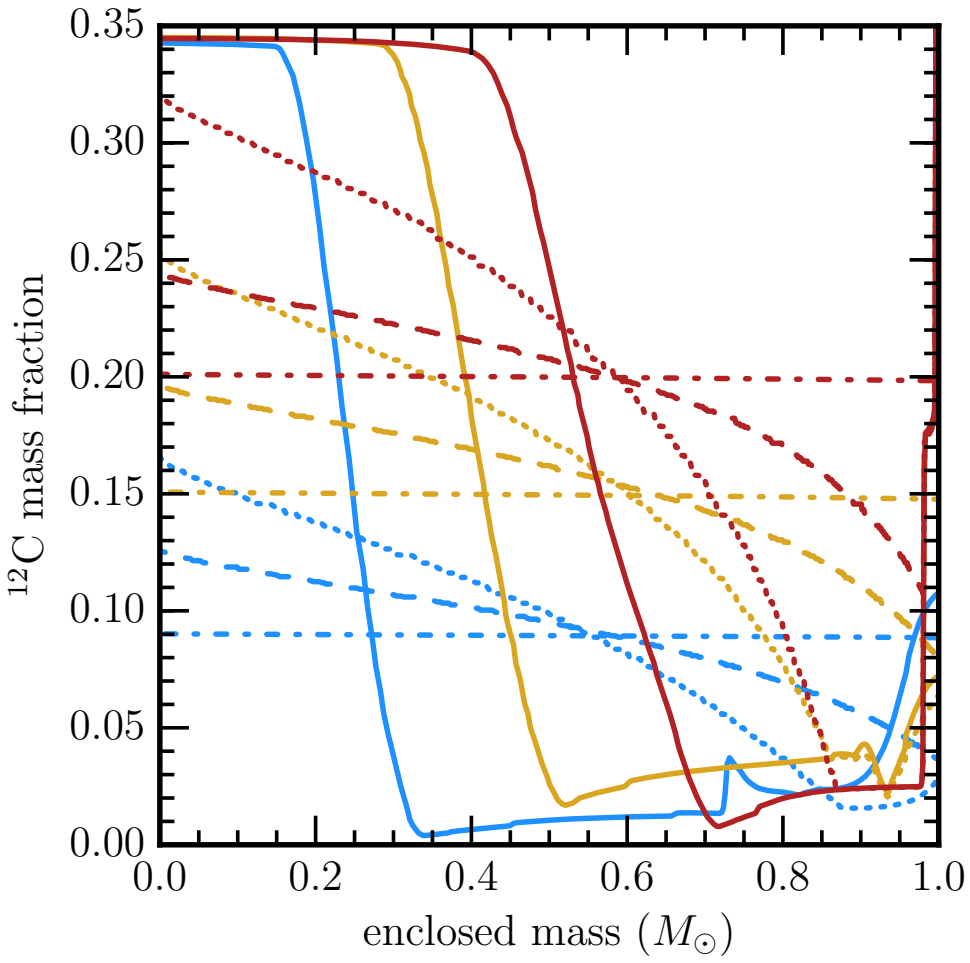

Figure 4.5 Carbon mass fractions as a function of time (labeled by central temperature). Red curves are for a hybrid WD with an initial $0.55M_\odot$ C/O core, orange curves a $0.40M_\odot$ C/O core, and blue curves a $0.24M_\odot$ C/O core. Solid curves show the carbon mass fraction before any mixing occurs, dotted when $\log T_c = 8.0$, and dashed when $\log T_c = 7.5$; the dot-dashed curve also at $\log T_c = 7.5$ includes thermohaline mixing.

Figure 4.5 includes the ^{12}C mass fraction profiles from all three models run with thermohaline mixing, at the time when $\log T_c = 7.5$ (dot-dashed lines). In this implementation, thermohaline mixing leads to fully mixed WDs at this time, with completely flat ^{12}C mass fraction profiles. Given the uncertainties in thermohaline mixing, however, the dashed (no thermohaline mixing) and dot-dashed (efficient thermohaline mixing) models in Figure 4.5 likely bracket the mass fraction profiles at this time.

4.5 Conclusions

We have shown that hybrid C/O/Ne WDs created from quenched carbon flames[1] are unstable to convective mixing as the WD cools. Weak reactions during carbon burning cause the O/Ne ash to have a lower Y_e than the C/O fuel. The configuration of a heavy O/Ne mantle above the cold C/O core is initially stable due to the higher temperatures of the freshly burned O/Ne mantle. However, as neutrino cooling and electron conduction reduce the temperature, the hybrid configuration becomes convectively unstable. Convective mixing rapidly leads to a much more uniform composition profile (Fig. 4.5).

Our modeling choices for this initial work lead to a profile that is very nearly neutrally buoyant (Figure 4.3). We did not explore the physics of thermohaline convection for this neutrino-cooled material, which remains an open question. However, at a minimum, neutral buoyancy would always be reached. We also do not allow the resulting convection to modify the thermal evolution of the WD (§4.3). This effect may be significant at the earliest times. Future work can address these questions and their impact on the compositional structure of hybrid WDs.

To understand the importance of this mixing for possible Type Ia scenarios, it is

[1] A recent multi-D study of the convectively-bounded carbon flames (Lecoanet et al., 2016) suggests that the bouyancy barrier accross the flame is too great to permit sufficient mixing to quench the flame, implying that hybrid C/O/Ne WDs are unlikely to form in the first place.

useful to compare the mixing times to the timescales for hybrid WDs to gain mass and approach the Chandrasekhar mass $M_{\rm Ch}$. The cooling times to the central temperatures of $\log T_c = 8.2, 8.0, 7.8,$ and 7.5 shown in Figures 4.3 & 4.4 are 13.5 kyr, 330 kyr, 6.4 Myr, and 77 Myr, respectively. For comparison, the time necessary to grow a $1.0 M_\odot$ WD to $M_{\rm Ch}$ at steady H and He burning rates is approximately 2 and 0.2 Myr, respectively. Furthermore, this does not take into account the time between WD formation and the start of mass transfer, which is often much longer than the growth time via accretion. Therefore, hybrid WDs in binary scenarios are likely to be even more mixed once they reach $M_{\rm Ch}$. Existing models of Type Ia SNe from hybrid WDs neglect this compositional mixing (Denissenkov et al., 2015; Kromer et al., 2015; Bravo et al., 2016).

If a mixed hybrid core can grow to $M_{\rm Ch}$, it is unclear whether its fate will be similar to that found in existing calculations of hybrid C/O/Ne WD explosions as candidate progenitors of some Type Ia SNe. When the core and mantle are fully mixed, the central carbon fraction is reduced significantly (see Figure 4.5). This implies that higher densities must be reached before carbon ignition and the subsequent carbon simmering phase can begin. The additional ^{23}Na and ^{25}Mg mixed into the core will increase the amount of Urca-process cooling that occurs (Denissenkov et al., 2015; Martínez-Rodríguez et al., 2016), potentially delaying carbon ignition to yet higher densities. Higher density ignition of carbon will change the nucleosynthetic signature of any resulting explosion (Townsley et al., 2009, 2016). In addition, the higher densities required for carbon ignition at low central carbon fractions can lead to exothermic electron-capture reactions on ^{24}Mg and ^{20}Ne setting in before carbon ignition densities are reached. This would give rise to qualitatively different evolution, potentially leading to accretion induced collapse of the white dwarf to a neutron star rather than a convective-core carbon burning runaway (e.g., Schwab et al. 2015).

Chapter 5

Accretion-Induced Collapse From Helium Star + White Dwarf Binaries

Accretion-induced collapse (AIC) occurs when an O/Ne white dwarf (WD) grows to nearly the Chandrasekhar mass ($M_{\rm Ch}$), reaching central densities that trigger electron captures in the core. Using Modules for Experiments in Stellar Astrophysics (`MESA`), we present the first true binary simulations of He star + O/Ne WD binaries, focusing on a $1.5 M_\odot$ He star in a 3 hour orbital period with $1.1 - 1.3 M_\odot$ O/Ne WDs. The helium star fills its Roche lobe after core helium burning is completed and donates helium on its thermal timescale to the WD, $\dot{M} \approx 3 \times 10^{-6} M_\odot$/yr, a rate high enough that the accreting helium burns stably on the WD. The accumulated carbon/oxygen ashes from the helium burning undergo an unstable shell flash that initiates an inwardly moving carbon burning flame. This flame is only quenched when it runs out of carbon at the surface of the original O/Ne core. Subsequent accumulation of fresh carbon/oxygen layers also undergo thermal instabilities, but no mass loss is triggered, allowing $M_{\rm WD} \rightarrow M_{\rm Ch}$, triggering the onset

of AIC. We also discuss the scenario of accreting C/O WDs that experience shell carbon ignitions to become O/Ne WDs, and then, under continuing mass transfer, lead to AIC. Studies of the AIC event rate using binary population synthesis should include all of these channels, especially this latter channel, which has been previously neglected but might dominate the rate.

White dwarfs (WDs) that are primarily composed of oxygen and neon (O/Ne) in their cores are expected to collapse to form neutron stars (NSs) as they approach the Chandrasekhar mass ($M_{\rm Ch}$). The collapse is triggered by the onset of electron capture reactions in the center of the star that occur above a critical density; this is the same trigger that gives rise to electron capture supernovae in single star evolution (Nomoto et al., 1979; Miyaji et al., 1980; Nomoto, 1984, 1987; Takahashi et al., 2013), with the key difference that the AIC scenario lacks an extended stellar envelope. When the WD grows in mass via accretion from a binary companion, this process is referred to as accretion-induced collapse (AIC; Canal et al., 1990; Nomoto & Kondo, 1991; Woosley & Baron, 1992; Ritossa et al., 1996; Dessart et al., 2006; Metzger et al., 2009; Darbha et al., 2010; Piro & Kulkarni, 2013; Tauris et al., 2013). AIC supernovae are predicted to be very fast and faint (Woosley & Baron, 1992; Dessart et al., 2006) and thus difficult to observe. The remnant NSs may, however, be detectable as low-mass binary pulsars (Nomoto & Kondo, 1991), or, if they are later spun up by accretion, millisecond pulsars (MSPs) (Tauris et al., 2013).

In this paper, we study AIC progenitor scenarios that involve a He burning star as the donor. The mass transfer rates of $\dot{M} \approx 3 \times 10^{-6} M_{\odot}$/yr experienced by these systems overlap with the steady helium burning rates for WDs, allowing for steady growth of the WD cores up to $M_{\rm Ch}$ (Yoon & Langer, 2003). We find that the C/O ashes from the steady helium burning shell ignite unstably in a shell flash, but that these carbon burning episodes do not significantly interrupt the growth of the WD, so that all models grow

to $M_{\rm Ch}$. This work presents the first modeling of the carbon shell flashes from steady helium burning in relation to growing the cores of O/Ne WDs.

In this work, we model the binary evolution of a He star + WD system by simultaneously modeling the evolution of the binary system, including the structure of both stars and their orbit. In addition to this more detailed model of the standard He star + O/Ne WD channel, we also speculate that He-star+C/O models that undergo carbon shell ignition before carbon core ignition can be a channel for AIC, as discussed in Brooks et al. (2016). A core ignition of a C/O WD would lead to a SN Ia, but a shell ignition non-explosively transforms the C/O WD into an O/Ne WD, which continues to accrete until AIC is achieved.

In §5.1 we discuss the initial parameter and modeling assumptions of our binary evolution `MESA` calculations. In §5.2 we follow the growth of an O/Ne WD through stable helium shell burning, and explain the physics of the unstable carbon shell burning episodes that occur. We explore the C/O WD carbon shell ignition to O/Ne WD AIC channel in §5.3, and discuss the structure of the WD leading up to the AIC event in §5.4. We conclude in §5.5 by highlighting the likely impact on expected rates.

5.1 Binary Evolution and Mass Transfer

We use `MESA` (r7624) (Paxton et al., 2011, 2013; Paxton et al., 2015) to model the full set of stellar structure equations for both stars simultaneously; we also model the evolution of the binary parameters taking into account their interaction through mass transfer. Both the He star and WD are created in `MESA` in single star evolution by starting with a zero-age main sequence (ZAMS) star. We generated models of O/Ne WDs using the same set of physical assumptions as Farmer et al. (2015) from initial masses of $11 - 12 M_{\odot}$ and removed the envelopes once carbon burning had ended. The

He star starts as an $8.5 M_{\odot}$ star and is evolved until just before He core ignition, at which point the H envelope is artificially removed. Both models had solar metallicity. After we remove the envelope from the WD, we let it cool for 10 Myr (roughly the difference in main-sequence lifetimes), then place it in a binary calculation with the He star.

We model the growth of the mass of the WD cores using the same method as growing the core mass of C/O WDs in Brooks et al. (2016), which calculates the fraction of the donated mass the accretor can retain based on its maximum rate of He-burning. While the system is in the regime for steady He-burning, the WD burns helium to carbon and oxygen at the same rate that it is accreting helium. As the mass transfer rates rise above the steady burning regime, the WD rapidly expands into its Roche lobe. We assume the the WD only accepts mass at the maximum steady burning rate and that the rest of the mass is lost from the system such that $\dot{M}_{\rm WD} + \dot{M}_{\rm wind} = \dot{M}_{\rm He}$, where $\dot{M}_{\rm wind}$ is the rate of mass loss from the binary, $\dot{M}_{\rm He}$ is the mass loss rate of the helium donor star, and $\dot{M}_{\rm WD}$ is the mass gain rate of the WD. We assume that the wind carries with it the specific angular momentum of the WD accretor. Figure 5.1 shows the resulting evolution for a range of initial orbital periods. This shows that as the initial orbital period increases, the mass transfer rates increase, and, thus, the mass loss and angular momentum loss rates from the system increase. If our prescription underestimates the specific angular momentum removed by the wind, the longer initial orbital period systems may be subject to mergers. Therefore, we choose 3 hours as our fiducial orbital period, as these short period systems have the lowest wind mass loss rates, and are the most likely to avoid mergers and be accurately modeled (given our assumptions) in the event that we underestimated the specific angular momentum of the wind. As the accretion rates (solid curves) do not vary much between the given range of orbital periods after gaining the first $0.02 M_{\odot}$, the structure of the WDs should be qualitatively similar as

$M_{\rm WD} \rightarrow M_{\rm Ch}$, relatively independent of the initial orbital period [1].

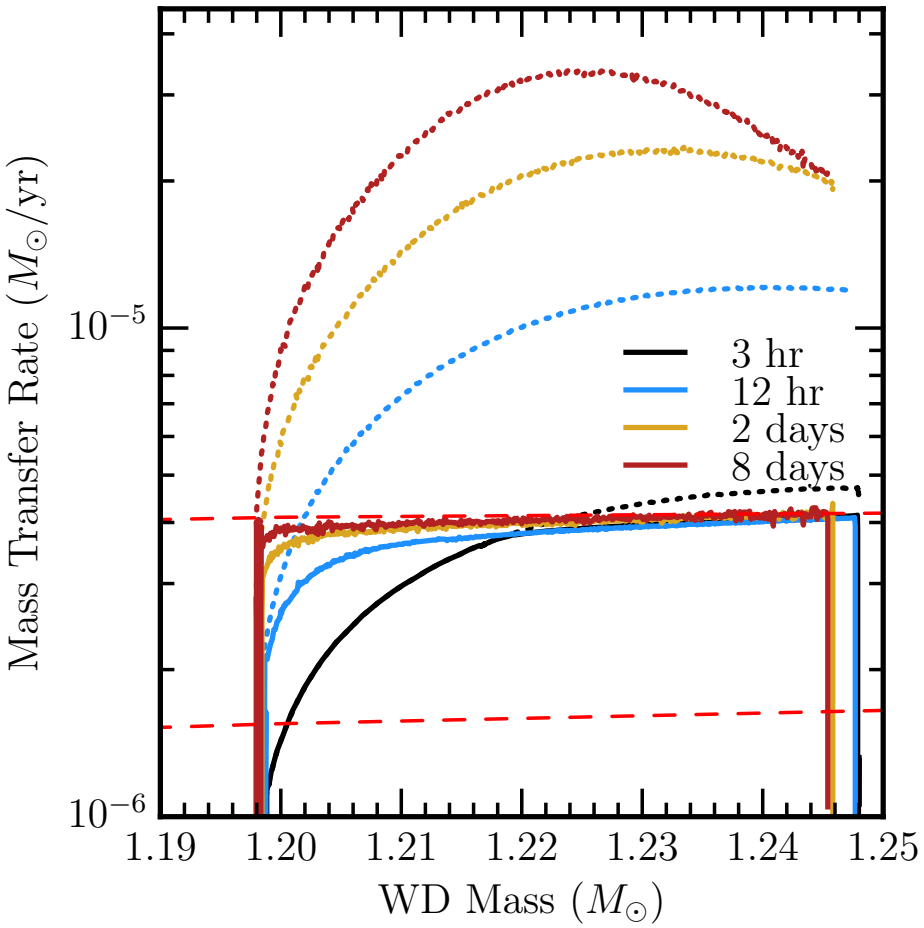

Figure 5.1 The mass transfer rates of $1.5 M_\odot$ He star + WD systems with a range of initial orbital periods from 3 hours to 8 days. The dotted lines show the rate at which mass is removed from the He star ($\dot{M}_{\rm He}$); the solid lines show the rate at which mass is accepted by the WD ($\dot{M}_{\rm WD}$). The difference is assumed to be lost from the system ($\dot{M}_{\rm wind}$), carrying the specific angular momentum of the WD accretor. The stable helium burning boundaries are shown by the dashed red lines. These simulations are only followed up to the first carbon shell ignition.

The high mass transfer rates and large core masses considered here lead to the ignition of carbon in the shell of helium burning ashes. Due to heat from the ashes leaking into

[1]The algorithm we use to determine the fraction of donated mass that stays on the WD leads to a small discrepancy for the 12 hour orbital period system, see Brooks et al. (2016) a discussion.

the colder core, the first unstable ignition in this shell occurs off-base. This leads to the formation of an inwardly-propagating carbon flame. In the case of an O/Ne WD accretor (see § 5.2), this carbon flame will propagate inwards until it runs out of carbon to burn at the edge of the O/Ne core. In the case of a C/O WD accretor (see § 5.3), since the whole WD is C/O, we expect that the carbon burning flame will propagate all the way to the center over about a year, converting the C/O WD to a O/Ne WD.

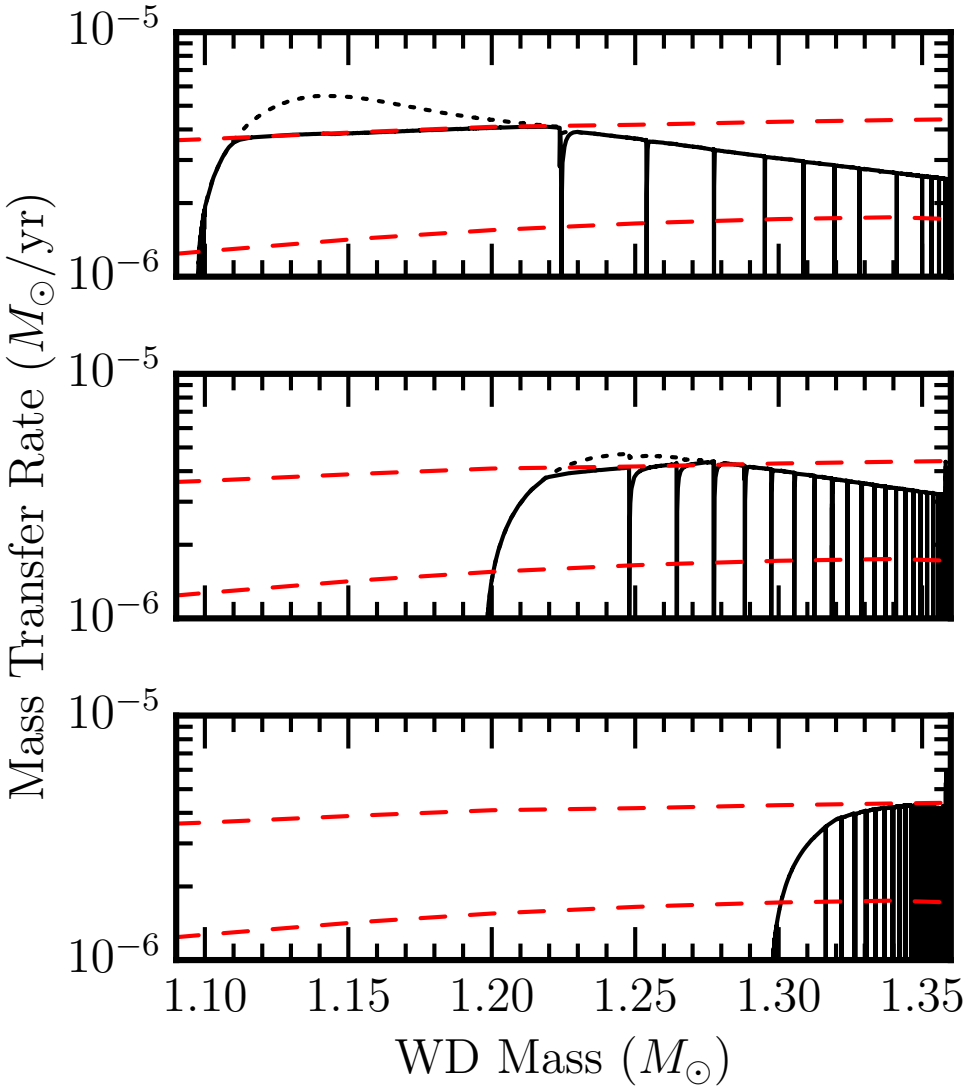

Figure 5.2 Mass transfer rates for O/Ne WDs with initial masses of $1.1, 1.2$, and $1.3 M_\odot$ in a binary system with a $1.5 M_\odot$ He star (solid black) at an initial orbital period of 3 hours. The mass transfer is punctuated by brief mass loss episodes caused by carbon shell flashes in the helium burning ashes. The solid tracks are the rate at which the WD is gaining mass; the dotted tracks are the rate at which the He star is losing mass. The difference between the dotted and solid tracks represent the mass that is lost from the system. The stable helium burning boundaries are shown by the dashed red lines.

In both cases, since we still have a massive WD core and high accretion rates, the WD will continue to build up C/O ashes from steady helium burning, and burn the

carbon in short shell flash episodes. All subsequent C/O layers ignite at the base of the freshly accumulated carbon. This is analogous to thermally pulsing AGB stars, where the hydrogen burning layer supplies helium ashes at below the steady helium burning rate, so the underlying helium burning shell is thermally unstable and will thus pulse. An important difference is that for these carbon burning episodes, most of their energy output is balanced by thermal neutrinos emitted in the convective regions above the burning layer (Timmes et al., 1994), meaning that negligible mass is lost ($\lesssim 10^{-5} M_\odot$) per carbon shell flash. This leads to a punctuated mass transfer history, as shown in Figure 5.2, where steady mass accretion is repeatedly interrupted during the brief carbon flashes. The duty cycle of these carbon flashes is about 0.001.

As we are only interested in showing the binary conditions needed to reach AIC, we halt evolution of all models when $\log \rho > 9.6$. At this point electron capture reactions in the center of the star begin to significantly remove pressure support (Schwab et al., 2015), and the timescale to collapse becomes hundreds of years.

5.2 O/Ne WD Accretors

We now discuss the details of the evolution of an initially $1.2 M_\odot$ O/Ne WD as it experiences its first carbon shell flash, an ingoing carbon flame, and then subsequent carbon flashes. The model starts with $0.025 M_\odot$ of C/O above a $1.175 M_\odot$ O/Ne core, which results from helium shell burning during the progenitor's AGB phase (Gil-Pons & García-Berro, 2001).

5.2.1 First carbon shell flash

Figure 5.3 shows the evolution of the density and

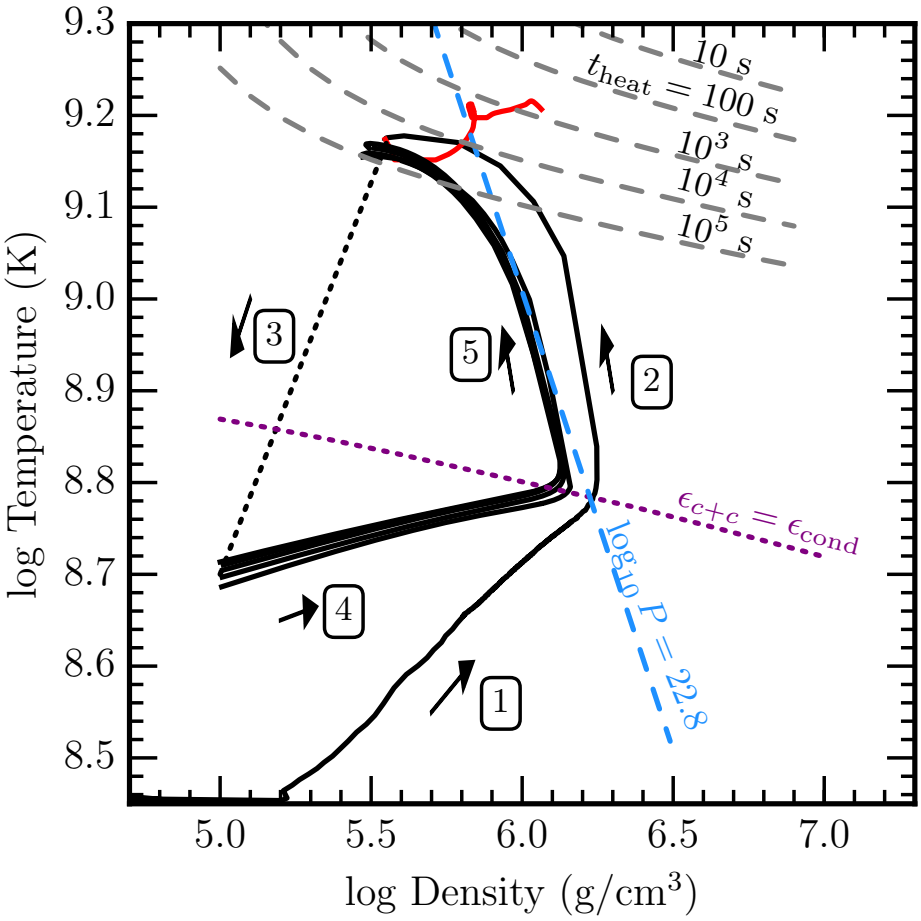

Figure 5.3 The evolution of the density and temperature at the mass coordinate of maximum temperature in the carbon layer. As accretion starts, this begins in the bottom-left corner and evolves along arrow 1. After crossing the purple dotted $\epsilon_{C+C} = \epsilon_{cond}$ line, carbon burning is ignited and it evolves along arrow 2. The evolution during the carbon flame phase (§5.2.2) is colored red. When carbon burning is quenched and the carbon layer is no longer well defined, we schematically represent the evolution with arrow 3. We begin to visualize the new carbon layer when $\log \rho = 5$. Then, as helium burning deposits more mass in the C/O layer, evolution proceeds along arrow 4 until carbon is ignited, at which point the evolution proceeds along arrow 5 until carbon burning quenches, and then the cycle repeats. The upper dashed lines represent locations where the heating time is a fixed value.

temperature at the mass coordinate of the maximum temperature in the carbon layer. This begins in the bottom-left corner and evolves (along arrow 1) towards higher temper-

atures and densities as accretion and steady helium burning increase the mass of the C/O layer. The carbon will unstably ignite when the C+C energy generation rate exceeds the rate at which conduction can remove the heat from a region with a local thickness of a scale height($\epsilon_{\rm C+C} > \epsilon_{\rm cond}$, Cumming & Bildsten 2001; above the purple dotted line). The first ignition starts in the middle (as opposed to the base) of the upper carbon layer (the ashes), as the compressional heat and leftover heat from helium burning in the C/O layer leaks through to the colder material below. The first shell flash starts at a mass coordinate of $M_r = 1.220 M_\odot$ with a $0.045 M_\odot$ layer of C/O below it, as shown in Figure 5.4.

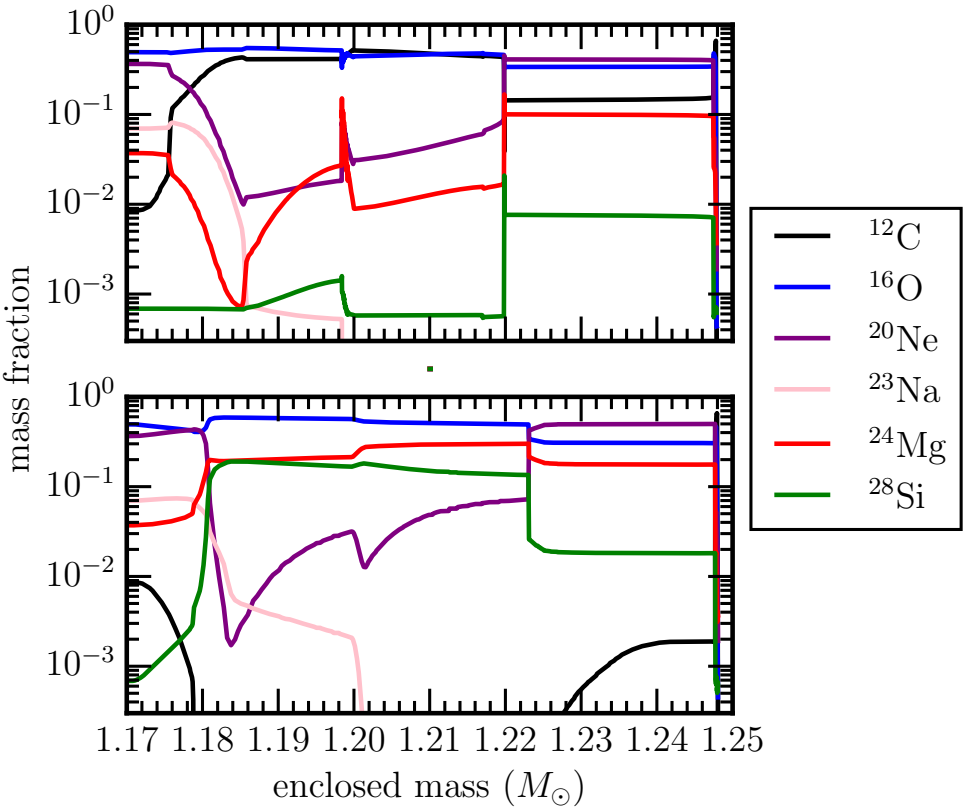

Figure 5.4 Top panel: Composition profile at minimum $t_{\rm heat}$ of the first carbon shell flash. The starting model has a mass of $1.20M_\odot$, with $0.025M_\odot$ of C/O on top of a $1.175M_\odot$ O/Ne core. Additional C/O is deposited from steady helium burning ashes until the mass of the WD reaches $1.247M_\odot$. The ignition of carbon burning starts at the mass coordinate $M_r = 1.220M_\odot$. Bottom panel: Composition profile after the carbon burning flame is quenched.

Once the carbon burning at the ignition location is generating heat faster than conduction can remove the heat, a thermonuclear runaway results. Since the ignition of carbon burning occurs in a thin shell, the thermonuclear runaway proceeds initially at roughly constant pressure (along arrow 2 in Fig. 5.3). The deviation from constant pressure occurs when the shell becomes radially extended so that continued entropy production mostly leads to density reduction. This keeps the runaway mostly hydrostatic, as evidenced by the fact that the heating time ($t_{\rm heat} = c_p T/\epsilon_{C+C}$) remains substantially

below the local dynamic time, $t_{\rm dyn} = H/C_s$, where H is the local pressure scale height and C_s is the sound speed; $t_{\rm dyn}$ never gets much greater that 0.1 seconds. About a day after the ignition, the carbon above the ignition location is depleted to a mass fraction $\approx$0.001.

5.2.2 The carbon flame

The layer directly beneath the burning layer heats up, primarily via electron conduction from the burning layer above, until it is hot enough to sustain its own carbon burning. In turn, it heats the underlying layer, and a slow, inwardly-propagating deflagration wave results. The temperature and density of the burning front are shown in Figure 5.3 in the red part of the curve that starts at $\log \rho = 5.6$, $\log T = 9.2$ and ends at $\log \rho = 6.45$, $\log T = 9.2$. The minimum heating timescale reaches $t_{\rm heat} \approx 100$ seconds during the flame duration. Therefore, the burning is always hydrostatic. The flame is thin (on the order of a kilometer or less) with a steep temperature gradient due to the high temperature sensitivity of carbon burning.

Ahead of the flame front, about two-thirds of the energy absorbed by unburned material goes into heating, and the other one-third is used for expanding. In the convective region behind the flame, energy release from carbon burning is mostly balanced by neutrino emission (Timmes et al., 1994). Some energy in this region raises the entropy of the material, leaving very little energy available to emerge from the C/O core (García-Berro et al., 1997).

We can roughly estimate a speed by $v \sim l/t_{\rm heat}$. We have the heating timescale, $t_{\rm heat}$, in the burning front, and define a geometrical thickness of the shell, l, by,

$$\epsilon_{\rm C+C} \approx \frac{D}{\rho}\frac{\partial^2 T}{\partial r^2} \approx \frac{D}{\rho}\frac{T_b}{l^2}, \tag{5.1}$$

where D is the thermal diffusion coefficient and T_b is the temperature at the base of the burning layer. Plugging in these values at the time when the flame is at a mass coordinate of about $1.21 M_\odot$ yields a flame speed within an order of magnitude of the numerical flame speed given by the model. Following the more rigorous approach of Timmes et al. (1994) gives,

$$v \approx 0.25 \left(\frac{c \epsilon_{\rm C+C}}{\kappa \rho_{\rm cold} E} \right)^{1/2}, \tag{5.2}$$

where 0.25 is derived from a rough fit to the numerical results, c is the speed of light, κ is the opacity at the flame front, $\rho_{\rm cold}$ is the density on the cold (inner) side of the flame front, and $E(= c_p T)$ is the internal thermal energy per gram. Using the values recorded at the location of maximum $\epsilon_{\rm C+C}$, we plot the flame speeds predicted by equation 5.2, along with the numerical flame speed in the model given by $v = \dot{M}/(4\pi r^2 \rho)$ for the $M_{\rm WD} = 1.2 M_\odot$ case in Figure 5.5. We use the Lagrangian speed $\dot{M}/(4\pi r^2 \rho)$ because the Eulerian speed, $dR_{\rm max}/dt$, where $R_{\rm max}$ is the radius of the maximum burning location, is impacted by the underlying core expansion. This Lagrangian speed is shown in solid black, and the theoretical flame speed from Timmes et al. (1994) is shown in blue. The flame speed steadily increases from a few cm s^{-1} to a few dozen cm s^{-1} in the first 65 days due to an increase in the temperature and carbon mass fraction at the burning front. After 65 days, the flame reaches $M_r = 1.20 M_\odot$ and the carbon mass fraction drops from 0.52 to 0.41, which reduces the energy generation rate, $\epsilon_{\rm C+C}$, by a factor of $\approx$1/4, which in turn lowers the flame speed by a factor of ($\Delta v_{\rm flame} \sim (\Delta \epsilon_{\rm C+C})^{1/2}$)$\approx$ 0.4. The shapes of the two curves match, meaning that the theoretical and numerical flame speed differ by a constant factor of less than order unity, which we set to 0.25.

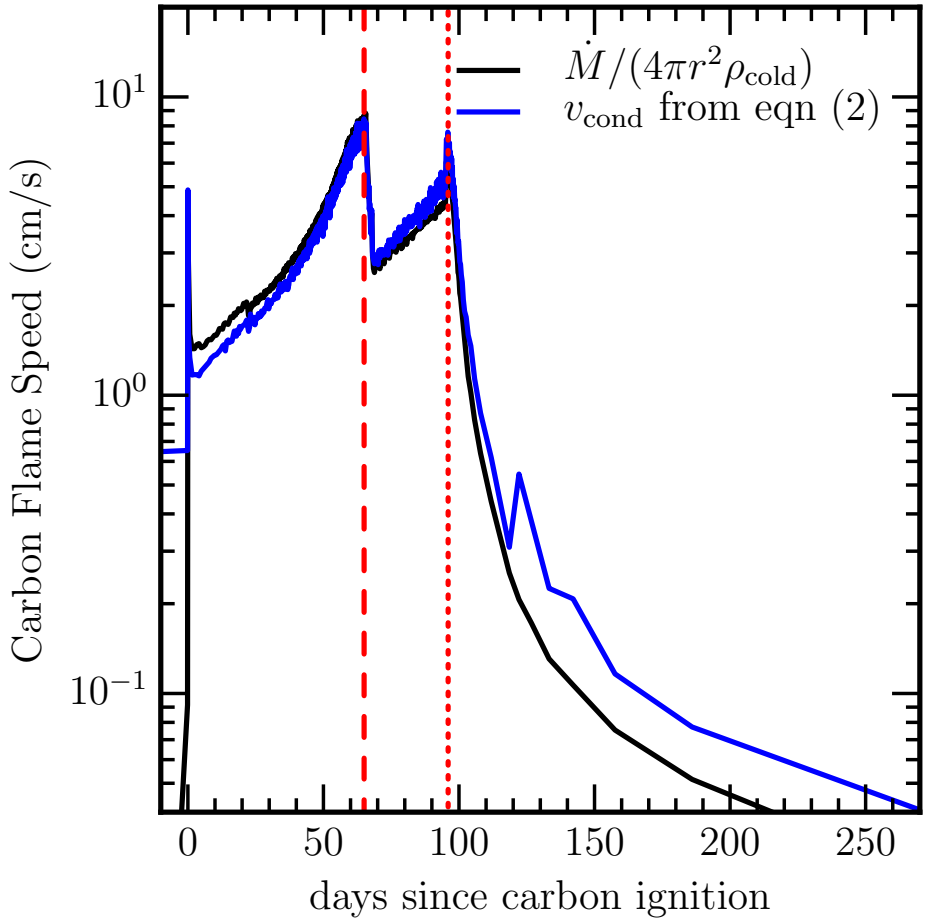

Figure 5.5 The numerical Lagrangian flame speed for the $M_{\rm WD} = 1.2M_\odot$ case is shown by the black solid line, and the theoretical flame speed, using equation 5.2 and the relevant local quantities, including the fitted prefactor of 0.25, is shown by the solid blue line. The vertical dashed red line labels the time when the flame has propagated all the way through the C/O ashes deposited from steady helium burning and enters into the C/O layer that existed on top of the O/Ne left over from formation. The flame speed slows slightly because this material is colder and denser than the C/O above it. The vertical dotted red line labels the time when the flame has propagated through the WDs original C/O layer and begins to quench as it runs out of carbon to burn within the O/Ne WD.

The flame takes about 100 days to reach the mass coordinate $M_r = 1.175M_\odot$, where the carbon mass fraction drops from 0.4 to <0.01. The carbon flame only fully quenches

after 200 years, which is not shown in Figure 5.5. The composition profile after the carbon flame has been quenched is shown in Figure 5.4. We can discern three separate regions processed by carbon burning. The outermost region, starting at $M_r = 1.223 M_\odot$, was burned in one week and is dominated by ^{20}Ne ($X_{^{20}\mathrm{Ne}} = 0.50$, $X_{^{16}\mathrm{O}} = 0.30$, $X_{^{24}\mathrm{Mg}} = 0.08$). This is due to the fact that the carbon in this region burns hot ($T_b \approx 1.6 \times 10^9$ K) and fast (only about a day). The shell processed by the (relatively) fast carbon flame ($1.20 M_\odot < M_r < 1.223 M_\odot$) is dominated by ^{16}O ($X_{^{16}\mathrm{O}} = 0.55$, $X_{^{24}\mathrm{Mg}} = 0.30$, $X_{^{28}\mathrm{Si}} = 0.15$, $X_{^{20}\mathrm{Ne}} = 0.05$). This region burns at a comparable temperature ($1.6 \times 10^9 < T_b < 2.0 \times 10^9$ K), but the burning happens over a longer timescale, enough for the reactions $^{20}\mathrm{Ne}(\gamma,\alpha)^{16}\mathrm{O}$ and $^{20}\mathrm{Ne}(\alpha,\gamma)^{24}\mathrm{Mg}(\alpha,\gamma)^{28}\mathrm{Si}$ to deplete $\sim$3/4 of the ^{20}Ne produced in carbon burning. The inner shell ($1.175 M_\odot < M_r < 1.20 M_\odot$) is processed by the (relatively) slow carbon flame and is dominated by ^{16}O (similar composition to layer above).

5.2.3 Subsequent Carbon Shell Flashes

After the carbon burning flame is quenched, the energy that was absorbed begins radiating outwards. As it reaches and expands the helium shell, the helium burning is shut off. During this transition, the base of the carbon layer and the maximum carbon burning location are not well defined, as all the existing carbon is consumed, so in Figure 5.3 the evolution is schematically represented by the dotted line in the direction of arrow 3. The model then resumes helium accretion, which increases the mass of the helium layer until steady helium burning reignites, which builds a new C/O layer. We catch up with the evolution of the new C/O layer once its density reaches 10^5 g cm^{-3} (arrow 4). The O/Ne layer beneath the C/O layer is still hot, so that compressional heat generated in the C/O layer cannot effectively radiate inwards. This means that the C/O layer will ignite at its base (arrow 5), preventing any more inwardly-propagating carbon flames.

The resulting pulsing behavior is analogous to the carbon flashes that occur on the surface of accreting neutron stars (Cumming & Bildsten, 2001). Each subsequent carbon shell flash ignites on a more massive core, leading to lower ignition masses and somewhat lower minimum $t_{\rm heat}$. The changes in radius and luminosity during these shell flashes are of order unity, meaning they are difficult to observe and do not lead to appreciable mass loss.

5.3 C/O WD accretors as AIC Progenitors

In order to estimate the full contribution of the AIC channel with He star donors, one must include not only WDs that begin the accretion stage as O/Ne WDs, but also those C/O WDs that transform into O/Ne WDs *during* the accretion stage. This can occur, as described in Brooks et al. (2016), if the donor is massive enough to sustain high accretion rates such that the hot carbon ashes near the surface of the accretor ignite before a carbon core ignition occurs. As discussed in §5.2.2, this shell ignition of carbon is non-explosive and initiates an inwardly propagating carbon flame much like that found in WD merger scenarios (Nomoto & Iben, 1985; Saio & Nomoto, 1985, 1998; Schwab et al., 2016).

An important contrast from the merger scenarios is that the C/O WDs in our scenario are more massive ($M > 1.2 M_\odot$) This means that they have much larger core densities and the flames have higher bounding temperatures. This leads to thin flames of initial width $\sim 10^2$ cm, agreeing with Timmes et al. (1994) for the same conditions ($\rho \approx 10^7$ g/cm^3, $T \approx 1.5 \times 10^9$ K). Using the flame speed at the start of the flame, we expect the entire core will be converted to O/Ne on a timescale of years. However, propagating such an initially thin flame all the way to the center of a massive C/O WD requires $\gtrsim$ 100x more timesteps than the other flames studied in this work.

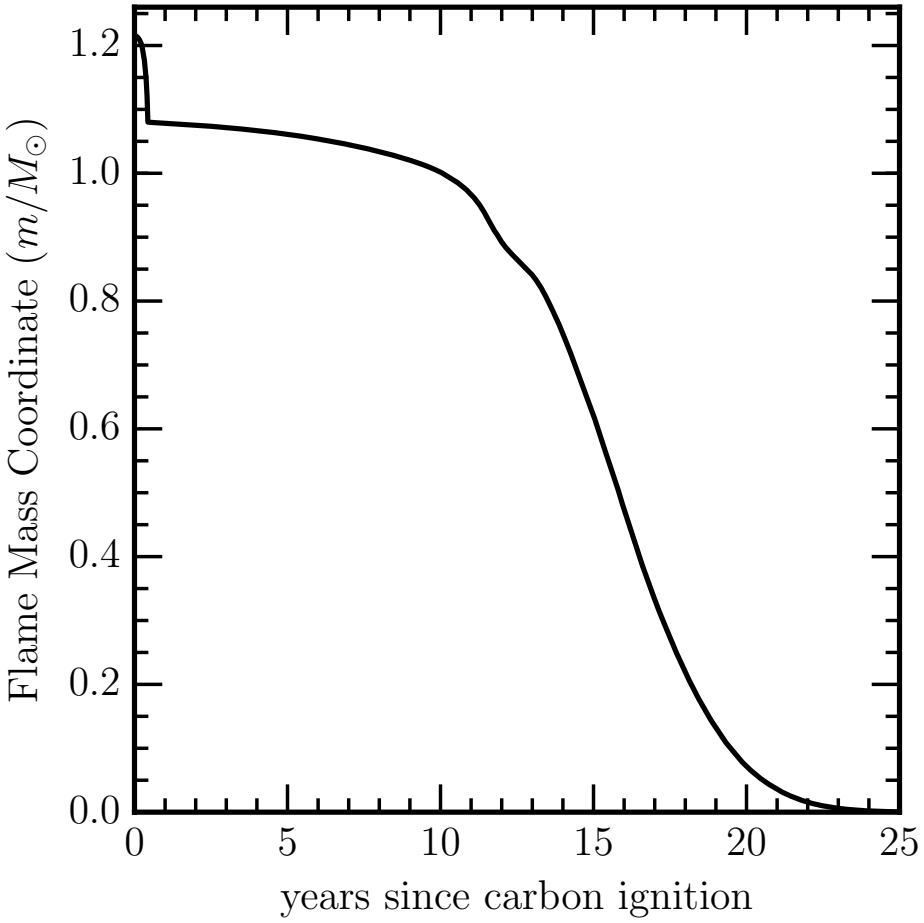

Figure 5.6 The mass coordinate of the inwardly-propagating carbon flame in a mixed hybrid C/O/Ne WD model. The flame speed is faster in the hot C/O ashes from steady helium burning, then it slows as it enters the mixed core which is colder and has a lower mass fraction of carbon, but then speeds up as it reaches higher temperatures and densities below the mass coordinate of $0.8M_\odot$.

The complications above make it prohibitive to fully follow the flame calculations all the way to the center of C/O WDs.[2] Therefore, we show here an illustrative example

[2]An additional complication is the suggestion for normal carbon flames that convective boundary mixing would quench the carbon flame and prevent the full conversion of any C/O WD to O/Ne (Denissenkov et al., 2013), resulting in a WD with a cold C/O core and a hot O/Ne mantle (Doherty et al., 2010; Denissenkov et al., 2013; Chen et al., 2014; Wang et al., 2014; Denissenkov et al., 2015; Farmer et al., 2015). A recent multi-D study of convectively-bounded carbon flames suggests that the buoyancy barrier across the flame is too great to permit sufficient mixing to quench the flame (Lecoanet et al., 2016). If future work shows that these flames do quench before reaching the center, then these models

that contains much of the same physics of carbon flames. We start with a $1.1M_{\odot}$ WD that, due to convective boundary mixing, had a $0.4M_{\odot}$ cold C/O core beneath a hot O/Ne mantle. As in Brooks et al. (2017c), we then allowed for complete mixing over 10 Myr and then placed this WD in a 3 hr orbital period binary with a $1.5M_{\odot}$ helium star. When the WD reaches $1.25M_{\odot}$ via accretion and steady helium burning, a carbon flame in the hot C/O ashes ignites and propagates into the star, as shown in Figure 5.6. When the flame finishes burning through the hot C/O ashes and meets the colder, mixed hybrid core ($X_{^{12}C} \approx 0.15$) the flame speed slows by almost two orders of magnitude, but continues propagating all the way to the core, converting the mixed hybrid C/O/Ne into a hot O/Ne WD in about 25 years. This is much faster than the $\approx 2 \times 10^4$ years for carbon flames in SAGB stars (Timmes et al., 1994; Farmer et al., 2015), due to the higher density of our WD interiors. However, even this calculation still took approximately 15,000 CPU-hours (corresponding to a wall time of months). Since there is negligible mass loss from this event, the system will continue with mass transfer onto the newly created O/Ne WD, experience additional carbon flashes as described in §5.2.3, and eventually approach $M_{\rm Ch}$ and reach AIC conditions. It appears likely that this fate will be generic for a range of C/O WDs accreting from sufficiently massive He star donors.

5.4 Structure at AIC

The carbon burning episodes that lead up to AIC in He star channels are important for understanding the structure of the outer layers of the WD just before AIC begins. The observational signatures of a collapse are strongly dependent on the amount of mass

would not evolve towards AIC. In Brooks et al. (2017c), we showed that such a 'hybrid' WD is in fact unstable to convection as it cools. However, in the accretion scenario considered in this paper, the relatively short timescale to grow to $M_{\rm Ch}$ ($\lesssim$ Myr) means that the WD would not be fully mixed at the time it nears $M_{\rm Ch}$. A partially mixed model may experience core carbon ignition yielding a peculiar thermonuclear explosion.

ejected, and both Darbha et al. (2010) and Woosley & Baron (1992) use fiducial ejected masses of $10^{-2}M_{\odot}$. Figure 5.7 shows the radius versus mass and density profiles of three AIC progenitors: the model that starts as a $1.2M_{\odot}$ O/Ne WD when $\log \rho_c = 9.6$ (solid black), a model from Schwab et al. (2015) that was created as a $1.325M_{\odot}$ O/Ne WD that artificially accreted the same O/Ne mixture onto the surface at a constant rate of $10^{-6}M_{\odot}$/yr until $\log \rho_c = 9.6$ (blue dashed), and the evolved remnant of the merger of two C/O WDs of masses $0.6M_{\odot}$ and $0.9M_{\odot}$ that is also approaching AIC (red dotted); this profile is taken from late in the evolution after carbon burning and neon-oxygen burning flames have reached the center and off-center Si ignition has occured (see Schwab et al., 2016, for details of this model and its evolution). The density profiles are similar in the core implying that the resulting accretion onto the newly formed NS and the initiation of explosion are likely to be similar. The merger model, however, has a larger envelope of $\approx 0.2M_{\odot}$ that may be ejected in the explosion, leading to a more visible electromagnetic source. Detailed calculations of explosions and lightcurves for both the WD merger and binary evolution AIC models would be valuable in providing insight into whether/how the observational outcome of AIC depends on the progenitor.

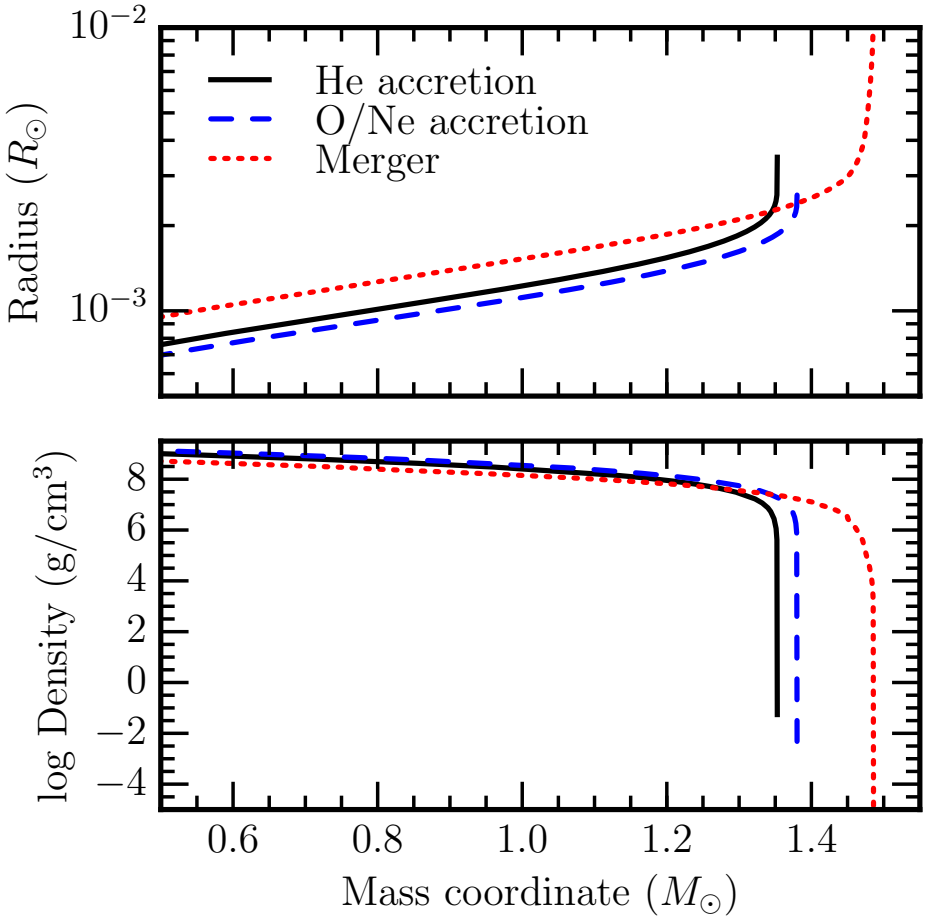

Figure 5.7 The solid black profile is from the model that starts at $1.1M_\odot$ and has $\log \rho_c = 9.6$. The blue dashed profile is from Schwab et al. (2015) that was created as a $1.325M_\odot$ O/Ne WD that accreted the same O/Ne mixture onto the surface until $\log \rho_c = 9.6$. The red dotted profile is from Schwab et al. (2016) which is the result of a merger between two C/O WDs of masses $0.6M_\odot$ and $0.9M_\odot$. This model never reached a central density of $\log \rho_c = 9.6$, and is instead taken after the Ne-flame has reached the center and off-center Si burning has started.

We find that for all of the models in this paper, the outer $10^{-2}M_\odot$ is extremely similar, due to being built up by steady helium burning on very similar core masses. The central region should also be almost identical (shown in Figure 5.8). Initially, the cores of these WDs are being adiabatically compressed on a timescale faster than the neutrino cooling

timescale, leading to evolution where $T \propto \rho^{1/2}$ (as shown by the light blue dotted line), but along different adiabats. However, at higher densities, neutrino cooling from the (^{25}Mg, ^{25}Na) and (^{23}Na,^{23}Ne) Urca pairs (Paczyński, 1973) causes the models to evolve to the same temperature before electron captures on ^{24}Mg begin. The similarity of our different models, independent of initial WD mass, implies that any resulting explosion from the AIC is likely to appear very similar observationally.

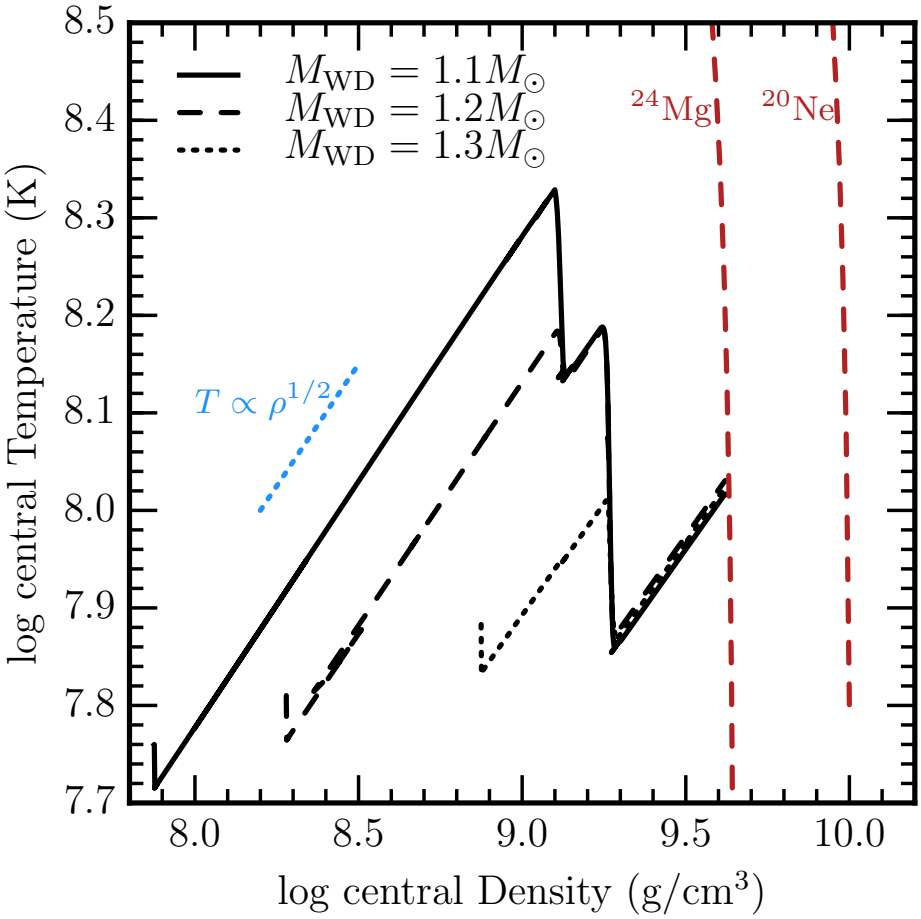

Figure 5.8 The black solid, dashed, and dotted lines show the evolution of the central density and temperature of the initially 1.1, 1.2, and 1.3$M_\odot$ WD models. The dark red dashed lines are the ignition curves for ^{24}Mg and ^{20}Ne electron captures. All models have similar temperatures at the onset of ^{24}Mg electron captures (see text for discussion of the temperature evolution).

5.5 Conclusions

We have presented the first full binary simulations of He star + WD systems that lead to AIC. We followed the standard scenario of an O/Ne WD that grows to $M_{\rm Ch}$, as well as discussing the scenario suggested by Brooks et al. (2016) in which a C/O WD accreting He experiences a carbon shell ignition, quiescently transforms into an O/Ne WD, and subsequently grows to $M_{\rm Ch}$. Both scenarios involve helium accretion onto the WD at rates that allow steady helium burning into hot C/O ashes, a shell ignition carbon flame that propagates inwards until all the star's carbon is exhausted, followed by a series of smaller carbon shell flashes as the WD core grows in mass. Computational limitations prevented us from propagating the carbon flames fully through our C/O WD accretors, though the work of Timmes et al. (1994) suggests that they will reach the center. Future work could more directly model this conversion process.

The carbon burning flames and flashes are non-explosive and radiate a significant portion of their energy in neutrinos. The flashes cause the radius and luminosity of the WD to increase by 25-100%, but are separated by at least hundreds of years, so they may be difficult to observe.

We evolve our models until they reach central densities at which electron captures will begin to occur, but do not follow them to collapse.[3] The capability to evolve realistic models up to the onset of the hydrodynamic collapse of the WD is still under active development in `MESA` and is therefore left for a future study. The current electron capture physics employed in `MESA` is covered in Schwab et al. (2015) for idealized models (simple compositions, steady accretion rate, no surface burning).

As shown in Figures 5.1 and 5.8, as long as the donor has enough helium for the WD to grow to $M_{\rm Ch}$ (taking into account wind losses), the conditions of the models at AIC

[3]Recently, using multi-dimensional simulations of the oxygen deflagration, Jones et al. (2016) suggested that collapse to a NS may not be assured.

are very similar over a wide range of initial orbital periods and WD masses.

There have been no direct observations of AICs. They are predicted to be faint and very short lived (Woosley & Baron, 1992; Dessart et al., 2006) and so they may be very difficult to observe. Unusual NSs provide the best evidence for AIC to date, although it is rather indirect. For example, we may see evidence for these events in the form of recycled MSPs (Tauris et al., 2013). In addition, if NS formation via AIC does not cause a kick, then they could explain the large numbers of NSs in globular clusters, and the subsequent spin-up from accretion could make them look young (Boyles et al., 2011; Antoniadis et al., 2016). In our calculation, the model with the $1.1M_{\odot}$ WD undergoes AIC when the donor only has $0.5M_{\odot}$ of helium left, most of which will be ejected due to the fact that the mass loss rate from the donor is a few orders of magnitude higher than the Eddington limit for NSs. This leaves little mass for spin-up accretion post-AIC, meaning systems like this may be the progenitors to high B-field, slow spinning NSs that are seen in globular clusters (Tauris et al., 2013). Bailyn & Grindlay (1990) show that their population study suggest that NSs born via AIC may resolve discrepancies in calculated birthrates.

Yungelson & Livio (1998) and Kwiatkowski (2015) give AIC rates from He star systems in spiral galaxies as a few $\times 10^{-5}$ per year, which should be significantly increased if our newly revealed C/O to O/Ne to AIC channel proves effective. Furthermore, Kwiatkowski (2015) show that the Helium star channel rate is comparable to the channels with Hertzsprung gap star, Red Giant star, AGB star, and WD donors. The inclusion of the C/O to O/Ne AIC channel may therefore significantly increase the predicted AIC rate due to the fact that lower mass C/O WDs are inherently more common than higher mass O/Ne WDs.

Chapter 6

Model Comparisons to Helium Star Donors: Checking Observations

We have the capability to model observed He star + WD binaries in `MESA` and check the claims of their detections, just as we did in §2.3.2. In this chapter we discuss the observations of three short orbital period binary stars with He star or He WD donors with compact objects.

In §6.1 we study HD 49798, a binary with a bright subdwarf-O star that has been studied since the 1960's. Different authors have disagreed as to the nature of the compact companion, whether it is a NS or WD. We give our interpretation of the compact companion, constrain its past evolution, and predict its possible futures.

Our collaborators at Cal Tech have observed some short period He star or He WD binaries and have asked us for model comparisons to their observed systems to make predictions. In §6.2 we discuss an 87 minute orbital period system with an sdB star and make predictions as to whether the sdB star will overflow its RL before or after nuclear burning has ceased, which significantly changes the stability of mass transfer. Then in §6.3 we study a much tighter binary system with a 44 minute orbital period with a hot,

newly formed He WD. Again, we predict from our models whether or not the eventual mass transfer will be stable.

Finally, in §6.4 we discuss the possible origins of an observed hypervelocity He star that may derive its high velocity from a tight orbit with a WD that exploded.

6.1 HD 49798: Its History of Binary Interaction and Future Evolution

The bright subdwarf-O star (sdO), HD 49798, is in a 1.55 day orbit with a compact companion that is spinning at 13.2 seconds. Using the measurements of the effective temperature ($T_{\rm eff}$), surface gravity ($\log g$), and surface abundances of the sdO, we construct models to study the evolution of this binary system using Modules for Experiments in Stellar Astrophysics (`MESA`). Previous studies of the compact companion have disagreed on whether it is a white dwarf (WD) or a neutron star (NS). From the published measurements of the companion's spin and spin-up rate, we agree with Mereghetti and collaborators that a NS companion is more likely. However, since there remains the possibility of a WD companion, we use our constructed `MESA` models to run simulations with both WD and NS companions that help us constrain the past and future evolution of this system. If it presently contains a NS, the immediate mass transfer evolution upon Roche lobe (RL) filling will lead to mass transfer rates comparable to that implied in ultraluminous X-ray sources (ULXs). Depending on the rate of angular momentum extraction via a wind, the fate of this system is either a wide ($P_{\rm orb}\approx$3 day) intermediate mass binary pulsar (IMPB) with a relatively rapidly spinning NS ($\approx$0.3 s) and a high mass WD ($\approx 0.9 M_{\odot}$), or a solitary millisecond pulsar (MSP).

HD 49798 is a binary system consisting of a hot and bright subdwarf in a 1.55 day

orbit with a compact companion. At the time of its discovery and classification it was the brightest hot subdwarf known (Jaschek & Jaschek, 1963), and remains one of the brightest today (Mereghetti et al., 2011). It was initially known to be a binary system, but Thackeray (1970) was the first to give a spectroscopic orbital period of 1.5477 days and to suggest that the compact companion may be a WD. Just two years later Dufton (1972) performed a non-LTE analysis to derive estimates on the effective temperature ($T_{\rm eff}$) and the surface gravity ($\log g$) of the sdO star, and Kudritzki & Simon (1978) improved upon these measurements; based on non-LTE modeling they found $\mathrm{T_{eff}}$=47 500±2000 K, $\log g$=4.25±0.2, $y = 50^{+10}_{-7}$ %, where $y = n(\mathrm{He})/n$, as well as a projected rotational velocity $v_{\rm rot} \sin$ i=45±5˙km s^{-1}for the hot subdwarf. This result was confirmed by an independent non-LTE analysis based on high-resolution VLT/UVES spectra (Müller, 2009). He found $\mathrm{T_{eff}}$=46 500±500 K, $\log g$=4.35±0.1, $y = 50$ % as well as a projected rotational velocity $v_{\rm rot} \sin i = 42$±5˙km s^{-1}which agrees with Kudritzki & Simon (1978). Additionally, Bisscheroux et al. (1997) also did analysis on the subdwarf and via a common envelope (CE) ejection efficiency parameterization concluded that an intermediate mass star that entered into a CE while on the early-AGB (EAGB) is the most likely progenitor to HD 49798.

This system was also detected in X-rays. Israel et al. (1995, 1996) published a detection of a 13.2 second period X-ray pulse which is interpreted as the spin period of a magnetic compact companion accreting from the subdwarf wind. The estimates of the mass loss rates from the subdwarf and the capture rate onto the companion and the associated accretion luminosity were compared to the observed X-ray luminosity by Israel et al. (1996) and led to their suggestion that a NS was more likely than a WD.

The layout of this paper is as follows. We continue a short review of previous studies of this binary system and confirm that our sdO stellar model matches the observations in §6.1.1. Then in §6.1.2 we give our arguments for a NS companion and show results

of binary modelling to give predictions on the future of the binary system. We also show results for binary modelling assuming a WD companion in §6.1.3. We explore the outcomes of a merger caused by a high rate of angular momentum loss via the system wind in §6.1.4, and finish with our conclusions in §6.1.5.

6.1.1 Observational Analysis

In this study, we build stellar models that match the measured values of $T_{\rm eff}$, $\log g$, mass, and surface abundances of the sdO star and constrain the past and future evolution of this system using `MESA` version 8118 (Paxton et al., 2011, 2013; Paxton et al., 2015).

Previous Compact Object Interpretation

Bisscheroux et al. (1997) looked at the same X-ray data from ROSAT as Israel et al. (1996), but used different estimates for the wind mass loss rates from the sdO star and concluded that a WD is more likely, but, a NS cannot be ruled out. One of their arguments against a NS companion has to do with their low birthrate and the small likelihood of seeing such a system. This argument does not hold because in the alternative scenario, a WD companion would accrete enough to reach $M_{\rm Ch}$ and undergo AIC, leaving a subdwarf and a NS.

Several papers from the same group have been published on this system in the past few years (Mereghetti et al., 2009, 2011, 2013, 2016). Mereghetti et al. (2009) detected an eclipse in the X-ray light curve with a period coincident with the spectroscopic period. This allowed them to derive the inclination of the system and a much more precise measurement of the masses in the system and found $M_{\rm sdO} = 1.50 \pm 0.05$, $M_{\rm CC} = 1.28 \pm 0.05$, where $M_{\rm CC}$ is the mass of the compact companion. They also use the eclipse duration to measure the size of the X-ray emitting region to be $\approx 10^4$ km, which is more

that two orders of magnitude larger than the blackbody radius they derive from the X-ray spectrum. Just as in previous studies, the authors use wind-capture accretion rates and compare to the X-ray luminosity to help distinguish between a NS or WD companion. Mereghetti et al. (2009, 2011, 2013) all favor a WD over a NS companion, but the new angular momentum and magnetic field analysis in Mereghetti et al. (2016) suggests that a NS companion is more likely.

sdO Modelling

Using `MESA`, we took the $1.5 M_{\odot}$ measurement of the mass of the subdwarf derived from combination of the X-ray mass function and the optical mass function by Mereghetti et al. (2009) and constructed a model by starting with a $7.15 M_{\odot}$ zero age main sequence (ZAMS) model, and started mass loss on the EAGB, just before the second dredge-up, and ended mass loss when the surface helium mass fraction of the model matches the observed value.

When the effective temperature ($T_{\rm eff}$) of the subdwarf model reaches the observed $47,500$ K, the $\log g$ measurement and derived radius and luminosity all agree with the model within the given error bars, as shown in Table 6.1. We also show this in the $T_{\rm eff} - \log g$ diagram of Figure 6.1.

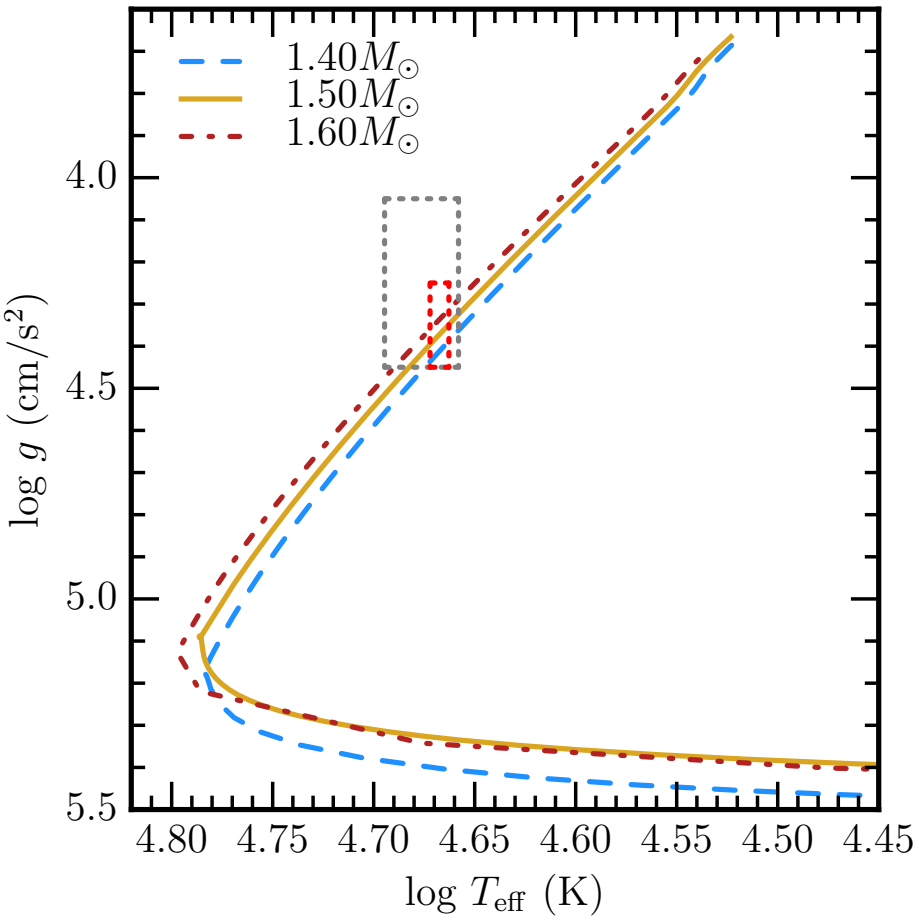

Figure 6.1 The dotted gray square represents the error box of the measurements of the $T_{\rm eff}$ and $\log g$ of HD 49798 from Mereghetti et al. (2009), and the dotted red box is from Müller (2009). The curves show the evolution of Helium cores of different masses evolving from the bottom of figure and move towards lower $T_{\rm eff}$ and $\log g$ and are cut off as RLOF begins in the upper right of the plot.

At the time when the measurements match the model, the carbon core has grown to $0.71 M_\odot$, and the surface is blowing off a wind at $6 \times 10^{-9} M_\odot$/yr, using the wind prescription from Bloecker (1995) and a scaling factor of 0.05. According to the model, the star will fill its RL approximately 65,000 years from now.

Table 6.1. Comparing to observations of the sdO

Observable	Observed	$1.50 M_\odot$ model
$T_{\rm eff}$ (K)	47,500 ± 2000	47,500
$\log g$ (cm s^{-2})	4.25 ± 0.2	4.41
Radius ($R_\odot$)	1.45 ± 0.25	1.25
log Lum. ($L_\odot$)	3.90 ± 0.15	3.85
$X_{\rm He,surf}$	0.78±0.07	0.78

6.1.2 Neutron Star companion

The measured spin-up rate of $\dot{P} = -2.15 \times 10^{-15}$ s s^{-1} given in Mereghetti et al. (2016) is high for a WD, requiring a relatively large accretion rate. At the maximum wind mass loss rate from the donor of $10^{-8} M_\odot$/yr (Hamann et al., 1981; Mereghetti et al., 2011), the companion would need to capture all the wind that crosses its RL to cause the measured spin up (see eq. 14 in Mereghetti et al., 2016), which is likely an overestimate of the wind capture rate. Therefore, we consider a NS interpretation of the compact companion to be much more likely.

If the companion is indeed a NS, there are two ways it could have formed: via a core collapse supernova (CCSN) from a star with a ZAMS mass of $\gtrsim 10 M_\odot$, or via AIC where the initially more massive star must have formed a O/Ne WD and subsequently accreted enough mass to reach $M_{\rm Ch}$. For the AIC progenitor scenario, the sdO star must have been RL filling at the moment of AIC, and must be less than half-RL filling just after the AIC to match the observations. Our calculations, based off the geometry of the system and the fact that the ejected mass from the AIC event (via neutrinos) takes with it the specific angular momentum of the WD, find that the change in the RL radius from that mass and angular momentum loss would only be about 4%. We ran models such that the donor was RL filling just before an AIC and is 4% below RL filling just after the

AIC, with a 1.55 day orbital period. Since the donor had a deeply convective envelope and was therefore responding adiabatically to mass loss, the sudden shut-off of mass loss causes the star to shrink, but only to 16% below its RL before expanding to refill its RL, whereas we now observe it as about half RL filling. If, however, the claimed distance of 650 pc is an underestimate, the radius of the sdO star would need to be significantly larger to match the measured $T_{\rm eff}$ and luminosity simultaneously. The problems with this scenario is that the $T_{\rm eff}$, $\log g$, and luminosity are already simultaneously matched for the model discussed in §6.1.2, implying that the radius is very near to what we show in Table 6.1 (Kudritzki & Simon, 1978), and this RL-filling progenitor model discussed here never matches the measured $T_{\rm eff}$ and $\log g$.

Additionally, although small eccentricities are expected for most post-AIC systems, this applies to systems with orbital periods in the range from 10 to 50 days (Tauris, 2015), whereas systems with periods of ∼a day end up in highly eccentric orbits (Chen et al., 2011). Given the uncertainties in tidal circularization timescales for these unusual binaries, however, we cannot say whether the absence of an eccentricity provides any constraint on the origin of the compact object (Stickland & Lloyd, 1994; Mereghetti et al., 2011).

Furthermore, to achieve the measured surface H fraction in this scenario would require the fine tuning of having the AIC occur just as the last bit of the H-rich envelope was being transferred to the WD, whereas a CE removing only the H-rich envelope and leaving just a little bit of surface H is a much more likely explanation. Therefore, if the companion is a NS, it was most likely formed via CCSN and not AIC.

MESA modelling of binary

We use `MESA`'s binary module to evolve the model in a 1.55 day orbit with a $1.28 M_{\odot}$ point mass. In our calculations, we assume that the system wind takes with it the

specific angular momentum of the companion. The high system wind rates during the RLOF phase will be optically thick, assuming spherical symmetry, and reprocess any high-temperature accretion luminosity. If, however, our system-wind angular momentum assumption is a significant underestimate, then the high mass transfer rate experienced when the subdwarf begins Roche lobe overflow (RLOF) could lead to a merger. We briefly explore the possible outcomes of a merger between the He star and a WD or NS companion in §6.1.4.

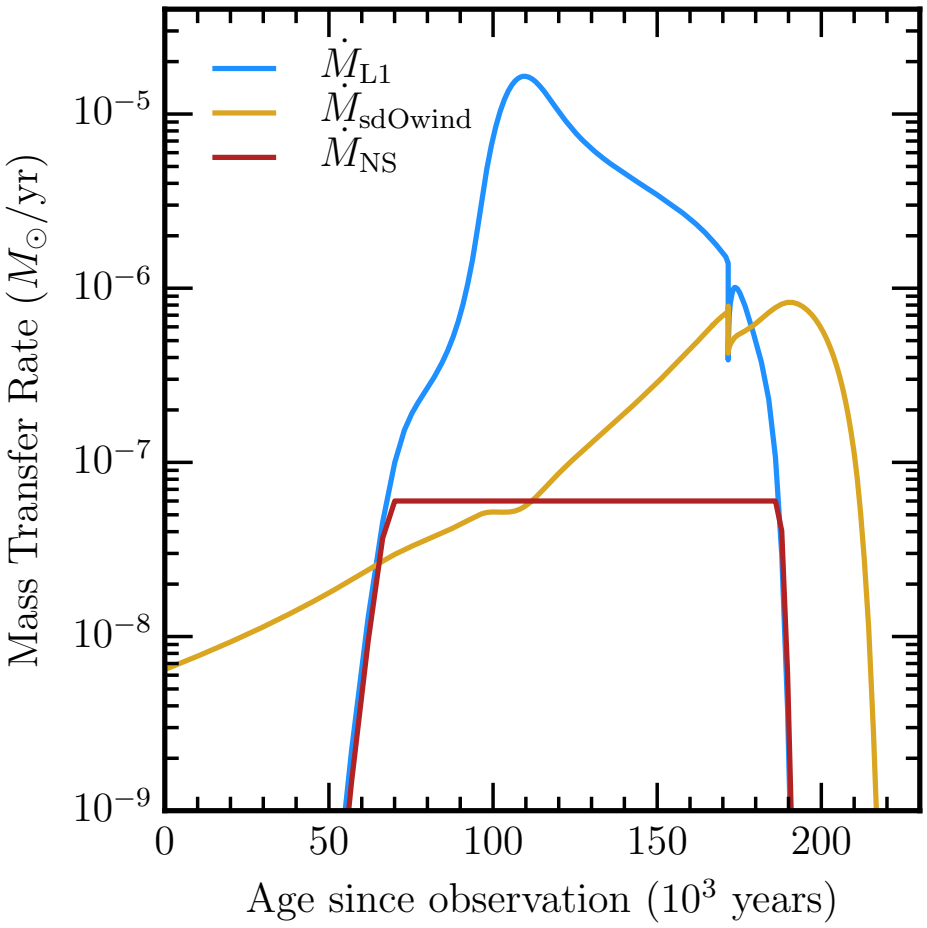

Figure 6.2 The blue line shows the rate of mass transfer via RLOF. The orange line shows the mass loss rate from the donor via winds. The dark red line shows the Eddington-limited mass gain rate of the NS.

At Roche lobe overflow (RLOF) the mass transfer rate through L1 quickly grows to $\approx 2 \times 10^{-5} M_{\odot}$/yr, almost all of which is lost from the system due to the Eddington limited accretion rate of the NS of $6 \times 10^{-8} M_{\odot}$/yr, meaning that the NS only gains $7.4 \times 10^{-3} M_{\odot}$ during this phase, which spins up the NS to a 33 ms spin period.

The system loses mass at such a high rate during RLOF that the wind becomes optically thick for $\approx 10^4$ yrs. We compute the radius at which the optical depth of the wind reaches unity assuming a spherically-symmetric wind, a wind speed of the escape velocity of the companion's RL, and electron scattering opacity, then use that radius and Eddington luminosity of the NS to compute the $T_{\rm eff}$ that will be observed during the RLOF stage. As shown in Figure 6.3, the observed $T_{\rm eff}$ from the wind decreases to $\approx 2.6 \times 10^4$ K at the highest mass loss rate.

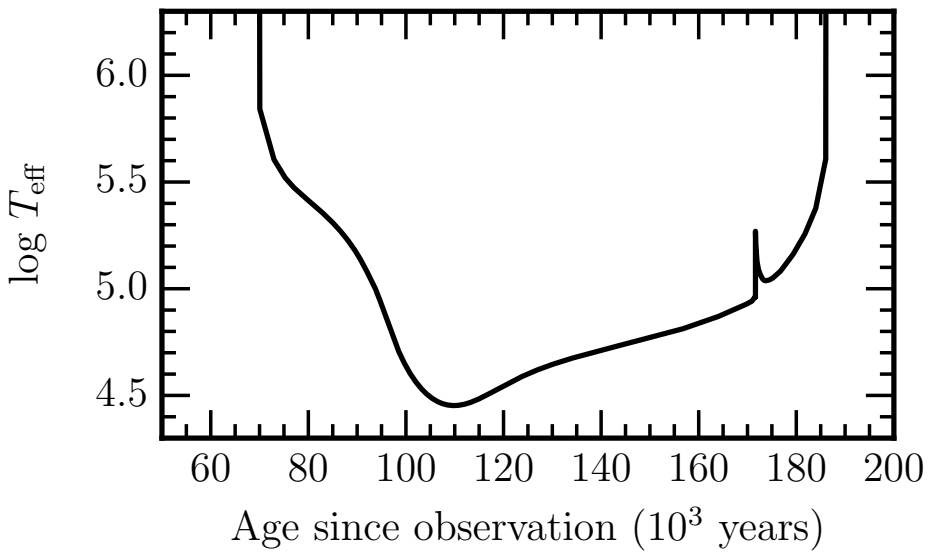

Figure 6.3 Effective temperature of the optically thick wind from the NS, assuming spherical symmetry, that reprocesses the thermal X-ray radiation to lower temperatures. We assume electron scattering opacity, a wind speed of the escape velocity of the NS's RL, and Eddington luminosity from the NS.

When mass transfer completes and the donor star radius drops below the RL, the

mass of the donor is $0.91 M_\odot$ and the orbital period is 2.7 days. At that orbital period, the inspiral time is much longer than the Hubble time, so the fate of this system is to be a IMBP with the $0.91 M_\odot$ C/O WD made from the He star.

Possible ULX Source

Ultraluminous X-rays (ULX) sources are powered by accreting NSs or stellar mass black holes at rates of $\approx 10^{-6} M_\odot$/yr (King et al., 2017). Recent detections of persistent pulsations (see Walton et al. 2017 for a summary) from many of these systems have proven that they often harbor a NS, implying that the accretion rate is $\gtrsim 10^2$ higher than the Eddington accretion rate. The binary evolution just described is a remarkable match for these ULX systems, as it stably provides accretion rates well above $10^{-6} M_\odot$/yr for a non-negligible amount of time ($\approx 80,000$ years) with an orbital period of 1.5 days. To explore the outcome of this type of ULX system, we ran a NS case where we set the maximum accretion rate of the NS to $\dot{M}_{\rm max} = 10^{-6} M_\odot$/yr. This does not qualitatively change the fate of the system (final donor star mass and orbital period after end of mass transfer are roughly the same) but the NS would reach an even more rapid rotation rate, up to 3 ms (rather than 33 ms), due to the additional accreted material. This is a reasonable scenario for this accretion rate, as the estimated maximum magnetic field strength of $B_s \lesssim 8.9 \times 10^9$ G (Mereghetti et al., 2016) would not allow for a magnetosphere to form outside the neutron star.

6.1.3 WD companion

If we model the compact companion as a massive WD instead of a NS, the evolution of the He star is identical up until the start of RLOF, and extremely similar afterwards due to the mostly negligible difference in mass retention rates between the given scenarios.

The maximum accretion rate of WDs is a few orders of magnitude higher than that for a NS, so a larger fraction of the mass donated by the He star remains in the system, but still more than half the mass is ejected (see Figure 6.4), taking with it the specific orbital angular momentum of the WD, as in Brooks et al. (2016). The WD steadily burns He on the surface to C/O, building up hot C/O layers that become unstable to runaway burning. The majority of energy released from carbon burning goes into neutrinos (which free stream out of the system) and increasing the entropy of the material, lifting the degeneracy of the C/O layer and expanding the surface of the WD by a factor of ≈ 2. This mild expansion is not enough to power mass loss, but is enough to temporarily prevent surface accretion. This can be seen in Figure 6.4, which shows the mass transfer rate by the dotted black line and the WD mass accretion rate by the solid black line, which has sharp dips caused by the carbon burning flashes (Brooks et al., 2017b).

The WD grows in mass up to $1.36 M_\odot$ when electron captures at the center begin to remove pressure support, leading to a collapse of the WD into a NS (Nomoto, 1987; Nomoto & Kondo, 1991; Woosley & Baron, 1992; Dessart et al., 2006; Schwab et al., 2015). At this stage, the He star has decreased in mass to $1.206 M_\odot$ and the period has increased to 1.9 days. The orbital period increases because although the ejected mass carries away angular momentum, the conservation of angular momentum of the transferred mass from the donor to the accretor has the net effect of increasing the orbital period. The WD loses a significant amount of mass to neutrinos during the collapse to a NS, causing a sudden increase in the RL of the He star. The He star quickly refills its RL due to He shell burning, and the system closely resembles that of the start of the NS case (§6.1.2), with a smaller He star mass and a longer orbital period. When the mass transfer completes and the newly formed WD drops below the RL, the mass of the WD is $0.91 M_\odot$, same as the NS scenario is §6.1.2, and the NS has gained $4.5 \times 10^{-3} M_\odot$. The final orbital period after mass transfer completes is about 2.7 days, same as the NS scenario: the inspiral

time is much longer than the Hubble time, leaving this system as an IMBP.

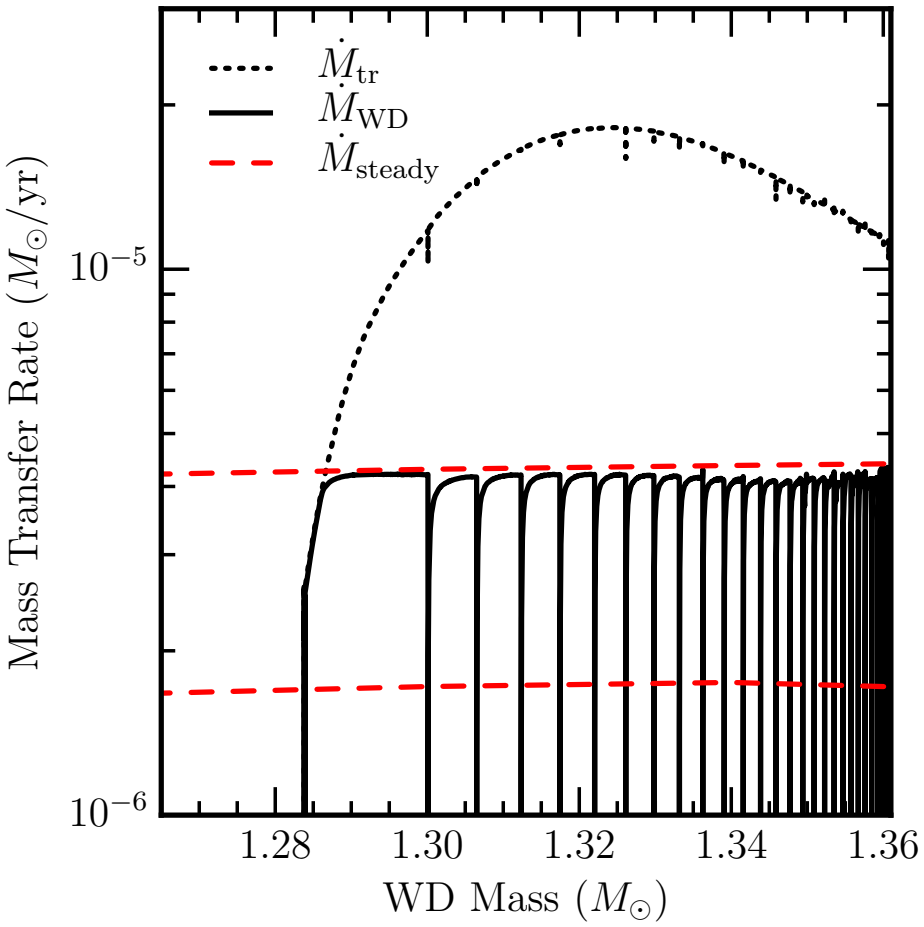

Figure 6.4 Mass transfer rate of a $1.28M_\odot$ O/Ne WD in a 1.55 day orbital period binary system with a $1.5M_\odot$ He star shown in solid black, which is punctuated by brief mass loss episodes caused by carbon flashes in the helium burning ashes. The solid tracks are the rate at which the WD is gaining mass; the dotted tracks are the rate at which the He star is losing mass. The difference between the dotted and solid track represents the mass that is lost from the system. The stable helium burning boundaries are shown by the dashed red lines from Brooks et al. (2016).

Just as in the NS scenario in §6.1.2, the donor transfers mass much faster than the companion can accept it, so the system wind is optically thick and reprocesses the thermal X-ray radiation from the WD at $T_{\rm eff} \gtrsim 10^6$ K to about 4×10^4 K at peak mass transfer

rates.

6.1.4 Merger Scenarios at RLOF

For the simulations shown in §6.1.2, the system mass loss reaches $2 \times 10^{-5} M_{\odot}$/yr. Since we assume that the system wind takes with it the specific angular momentum of the compact companion, the mass transfer is stable and leads to an overall increase in the orbital period and the binary separation. If, however, this is an underestimate of specific angular momentum of the system wind, the large system mass loss rates and, thus, the large angular momentum loss rates could lead to a merger.

As mass transfer rates rise due to helium shell burning in the donor causing the star to rapidly expand into its RL, a large angular momentum loss rate will cause the size of the RL to shrink, increasing the mass loss rate, causing even faster angular momentum loss, resulting in runaway mass transfer. The helium from the donor would form a CE, leading to a merger between the compact companion and the $0.71 M_{\odot}$ C/O core of the donor.

If the compact companion is a NS, we can use the results from Metzger (2012) to predict the general outcome of such a merger. We use his model NS_C-O_1, as its parameters are similar to HD 49798. Using the wind rate and velocity from the disk and the total mass of the disrupted C/O core ($0.71 M_{\odot}$), we can estimate the total kinetic energy deposited by this disk wind. Comparing this to the binding energy of the helium, now in a CE, we find that the energy from the disk wind is certainly large enough to eject all of the helium from the system. Most of the disk mass from the disrupted C/O core is blown off in the disk wind, and only $\approx 0.11 M_{\odot}$ is deposited on the NS, according to estimates from the NS_C-O_1 model from Metzger (2012). This results in a NS of mass $M \approx 1.39 M_{\odot}$ with a spin period of $P_{\rm spin} \approx 2.4$ ms, making this a millisecond pulsar of

average NS mass.

If the compact companion is a WD, there would be a similar lead up to the disruption of the C/O core of the donor, but the remnant would last much longer. The disrupted C/O sitting on top of the $1.28 M_{\odot}$ O/Ne core would go through a viscous phase and a carbon burning flame as outlined in Schwab et al. (2016), but since the WD would be primarily O/Ne, the flame would quench once it reached the O/Ne core, preventing the lifting of degeneracy of the core. After the C/O burns to O/Ne and becomes part of the degenerate core, the core mass grows above $M_{\rm Ch}$ and electron captures start to relieve pressure in the center (before reaching conditions for neon burning, see Schwab et al., 2016), leading to an AIC.

6.1.5 Conclusions

We have shown that the observations of the sdO star HD 49798 are well fit by a star born with a $7.15 M_{\odot}$ ZAMS mass that enters into a CE just before the second dredge-up on the early AGB to become a $1.50 M_{\odot}$ He star with a $10^{-2} M_{\odot}$ H-rich envelope. Furthermore, the observations of the compact companion's X-ray pulsations suggest that a NS interpretation is more likely, but that a WD interpretation cannot be ruled out. We used `MESA` to simulate the evolution of this system, and predict that, for either a NS or WD companion, the fate of this system is to become a wide IMBP with a high mass ($\approx 0.9 M_{\odot}$) WD and relatively rapidly spinning NS. This result assumes that the system wind takes with it the specific angular momentum of the compact companion. If, however, the system wind extracts extra angular momentum, the high mass transfer rates ($2 \times 10^{-5} M_{\odot}$/yr) can lead to mergers (see §6.1.4). In the event of a merger, whether the companion is a WD or NS, the predicted fate is to become a solitary NS, which would be a MSP in the case of a NS companion. In the case of a WD companion going into a

merger, the resulting spin period after an AIC inside of an extended helium envelope is uncertain.

If the companion is a NS we have shown that, during accretion, the system may have properties consistent with an ULX. So far only two ULX systems have a confirmed companion. P13 has a confirmed blue supergiant donor of spectral type B9Ia (Motch et al., 2014). The accretor in P13 shows a ≈0.42 s slowly spinning up period which demonstrates that the accretor in P13 is a neutron star (Fürst et al., 2016; Israel et al., 2017). The second known system, M101 ULX-1, has a Wolf-Rayet star donor in an 8.2 day orbit. The accretor is most likely a stellar mass black hole (Liu et al., 2013). Because of the lack of confirmed donor stars in ULX an sdO donor cannot be excluded in other ULXs. Therefore, we conclude that HD 49798 is a plausible progenitor binary to a ULX.

6.2 PTF1 J082340.04+081936.5: A hot subdwarf B star with a low mass white dwarf companion in an 87 minute orbit

We collaborated with observers from the Palomar Transient Factory (PTF; Law et al. 2009; Rau et al. 2009) who discovered the hot subdwarf B star (sdB) binary PTF1 J082340.04+081936.5. The system has an orbital period $P_{\rm orb}$=87.49668(1) min (0.060761584(10) days), making it the second-most compact sdB binary known. The lightcurve shows ellipsoidal variations. Under the assumption that the sdB primary is synchronized with the orbit, we find a mass $M_{\rm sdB} = 0.45^{+0.09}_{-0.07}\,{\rm M}_{\odot}$, a companion white dwarf mass $M_{\rm WD} = 0.46^{+0.12}_{-0.09}\,{\rm M}_{\odot}$ and a mass ratio $q = \frac{M_{\rm WD}}{M_{\rm sdB}} = 1.03^{+0.10}_{-0.08}$.

The future evolution was calculated using the `MESA` stellar evolution code. Adopting

a canonical sdB mass of $M_{\rm sdB} = 0.47\,{\rm M}_\odot$ we find that the sdB still burns helium at the time it will fill its Roche lobe if the orbital period was less than 106 min at the exit from the last common envelope phase. For longer common envelope exit periods the sdB will have stopped burning helium and turned into a C/O white dwarf at the time of contact. Comparing the spectroscopically derived $\log g$ and $T_{\rm eff}$ with our `MESA` models, we find that an sdB model with a hydrogen envelope mass of $5 \times 10^{-4}\,M_\odot$ matches the measurements at a post-common envelope age of 94 Myr, corresponding to a post-common envelope orbital period of 109 min which is close to the limit to start accretion while the sdB is still burning helium.

6.2.1 Evolutionary History

In the standard formation scenario, the so-called 2nd common envelope channel, the system starts as a low mass binary with $\approx$1 $\rm M_\odot$ components. The initially more massive star first evolves to become a WD. Subsequently, the sdB progenitor fills its Roche lobe at the tip of the red-giant branch (RGB), forming an sdB with a canonical mass of $M_{\rm WD} = 0.47\,{\rm M}_\odot$, set by the helium core flash, with a WD companion (Han et al., 2002, 2003). Han et al. (2002) showed that the binding energy of the envelope is very small at the tip of the RGB for a $1\,{\rm M}_\odot$ star and therefore the orbital shrinkage in the CE phase is not significant. They predict that sdB+WD binaries are formed with orbital periods longer than found in PTF1 J0823.

In a different picture an ultracompact sdB+WD binary can also be formed from a more massive main-sequence binary where the sdB progenitor is $> 2{\rm M}_\odot$. This sdB progenitor ignites helium non-degenerately in the core and fills its Roche lobe during the Hertzsprung gap or at the base of the RGB, resulting in an sdB with either a lower or higher mass compared to the tip of the RGB (Nelemans, 2010; Geier et al., 2013). In

such systems, the envelope is more tightly bound and the orbital shrinkage required to eject the CE becomes higher (Nelemans, 2010; Geier et al., 2013). Geier et al. (2013) showed that CD−30°11223 evolved most likely from a $2\,M_\odot$ progenitor for the sdB with a 3 - $4\,M_\odot$ companion for the WD progenitor. The WD companion in PTF1 J0823 is, with an upper mass limit of $M_{\rm WD} = 0.58\,M_\odot$, less massive than in CD−30°11223 .

Perhaps the most similar system is KPD 0422+5421 (Koen et al., 1998). However, its orbital period is $P_{\rm orb}$=129.6 min and therefore about 42 min longer than PTF1 J0823. Due to the longer period in KPD 0422+5421, this system is easier to explain by the 2nd common envelope channel from Han et al. (2002).

6.2.2 Future evolution

To understand the future evolution of the system, we used the code `MESA` (Paxton et al., 2011, 2013; Paxton et al., 2015). For the model we assumed an sdB with a canonical mass $M_{\rm sdB} = 0.47\,M_\odot$ with a white dwarf companion of $M_{\rm WD} = 0.49\,M_\odot$. Using release version 8118, we construct binary simulations that model the full stellar structure equations for the sdB and treat the WD as a point mass. We ran a set of simulations with periods, when the system exits the CE (post-CE orbital period), ranging from 87 to 120 minutes. The evolution of the system is governed by the loss of angular momentum due to radiation of gravitational waves. We record the post-CE age at which the orbital periods match the observed period of 87 minutes, shown by the dotted blue curve in Fig. 6.5, and the age at which the stars make contact, shown by the dashed-dotted red curve. Recent modeling of asteroseismic observations of sdB stars (Constantino et al., 2015) points to convective cores much larger than found with the Schwarzschild condition. At present, there is no clear consensus on the physics needed to achieve these larger cores, which prolongs the lifetime of the He burning phase. To accommodate such an outcome,

we performed runs with element diffusion active (Michaud et al., 2007; Schindler et al., 2015), doubling the convective core mass (from $0.109 M_{\odot}$ to $0.218 M_{\odot}$) and the core-burning lifetime (from 80 Myr to 152 Myr). The data from these runs are shown in Figures 6.5 and 6.6.

If contact is made after core and shell He burning have finished (dashed grey and dashed-dotted black curves in Fig. 6.5) and the sdB has become a C/O WD with a $0.41 M_{\odot}$ core and $0.06 M_{\odot}$ He envelope, the component that used to be the sdB will overflow its Roche lobe at an orbital period of less than 2 minutes, leading to a prompt merger and formation of an R CrB type star and subsequent evolution into a massive single WD. Figure 6.5 shows that the post-CE orbital period lower limit for this outcome is 106 min.

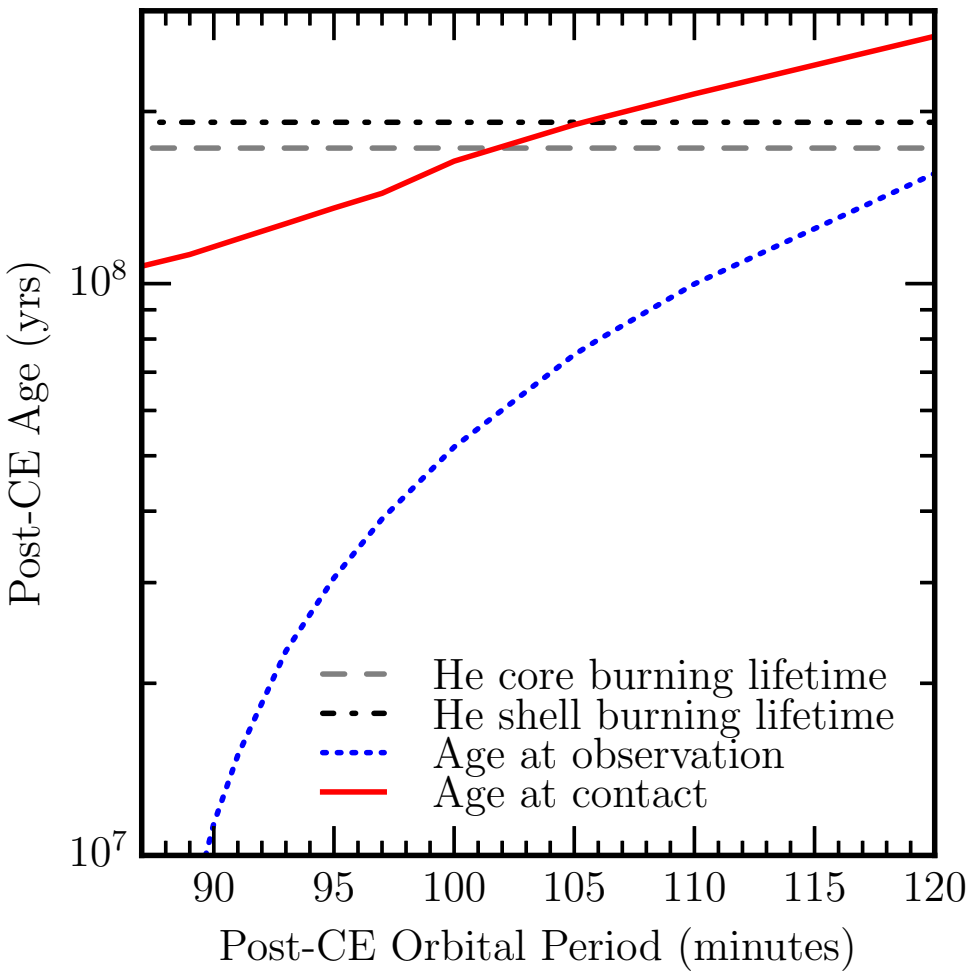

Figure 6.5 The model post-CE orbital period is shown on the x-axis, with the post-CE age on the y-axis. The dashed grey and dashed-dotted black lines show the core and shell He burning lifetimes of the sdB, respectively. The dotted blue curve shows the ages of the models when the orbital period matches the period that we observed for this system. The red curve shows the ages at which the stars make contact. Systems with initial orbital periods longer than 106 minutes will make contact after the sdB finishes He burning.

On the other hand, if the post-CE orbital period is less than 106 minutes, contact is made during the He burning phase, a merger may be avoided and the sdB will donate its remaining helium in an AM CVn type system (Brooks et al., 2015).

6.2.3 Current age

Figure 6.6 shows the position of PTF1 J0823 in the $T_{\rm eff}$ – $\log g$ diagram overplotted with the confirmed sdB+white dwarf systems in compact orbits as well as theoretical evolutionary tracks. The sdBs with WD companions populate the full extreme horizontal branch (EHB) band homogeneously with a small fraction of sdBs having evolved off the EHB. The values of $T_{\rm eff}$ and $\log g$ for PTF1 J0823 are consistent with an sdB on the EHB in the core helium burning stage.

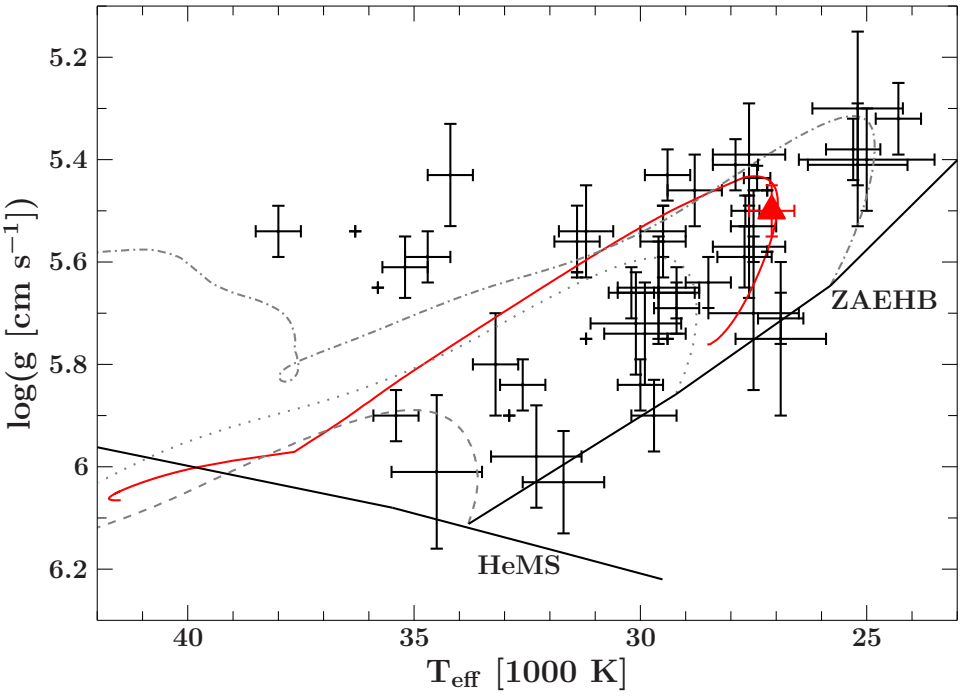

Figure 6.6 $T_{\rm eff}$ – $\log g$ diagram of the compact binary sdB stars with confirmed white dwarf companions (Kupfer et al., 2015). The red triangle marks PTF1 J0823. The helium main sequence (HeMS), the zero-age EHB (ZAEHB) and the terminal-age EHB (TAEHB) are superimposed with EHB evolutionary tracks by Han et al. (2002) (dashed lines: $m_{\rm env} = 0.000\,{\rm M}_\odot$, dotted lines: $m_{\rm env} = 0.001\,{\rm M}_\odot$, dashed-dotted lines: $m_{\rm env} = 0.005\,{\rm M}_\odot$ using $0.45\,{\rm M}_\odot$ models). The red solid line shows the EHB evolutionary track calculated with `MESA` using a $0.47\,{\rm M}_\odot$ model with $m_{\rm env} = 5 \times 10^{-4}\,{\rm M}_\odot$.

In a comparison of the spectroscopically derived $T_{\rm eff}$ and $\log g$ with our `MESA` models,

we find that an sdB model with a $5\times10^{-4}\,M_{\odot}$ hydrogen envelope matches the atmospheric parameter at a post-CE age of 94 Myr (Fig. 6.6), corresponding to a post-CE orbital period of 109 min which is close to the limit where the sdB still burns helium when filling its Roche lobe.

6.3 The OmegaWhite survey for short-period variable stars - V. Discovery of an ultracompact hot subdwarf binary with a compact companion in a 44 min orbit

We report the discovery of the ultracompact hot subdwarf (sdOB) binary OW J074106.0-294811.0 with an orbital period of P_{orb}=44.66279 ± 0.00011 min, making it the most compact hot subdwarf binary known. Spectroscopic observations using the VLT, Gemini and Keck telescopes revealed a He-sdOB primary with an intermediate helium abundance, T_{eff}=39 400 ± 500 K and $\log g$=5.74 ± 0.09. High signal-to-noise ratio lightcurves show strong ellipsoidal modulation resulting in a derived sdOB mass $M_{\rm sdOB} = 0.35 \pm 0.07\,M_{\odot}$ with a massive WD companion ($M_{\rm WD} = 0.90 \pm 0.08\,M_{\odot}$). The mass ratio was found to be $q = M_{\rm sdOB}/M_{\rm WD} = 0.38 \pm 0.06$.

To put constraints on the structure and evolutionary history of the sdOB star we compared the derived T_{eff}, $\log g$and sdOB mass to evolutionary tracks of helium stars and helium white dwarfs calculated with Modules for Experiments in Stellar Astrophysics (`MESA`). We find that only a helium white dwarf model with a mass of $0.320\,M_{\odot}$, which left the common envelope ≈1.1 Myr ago, is consistent with the observations. As a helium white dwarf with a massive white dwarf companion the object will reach contact in

17.6 Myr at an orbital period of 5 min. Depending on the spin-orbit synchronization timescale the object will either merge to form an R CrB star or end up as a stably accreting AM CVn type system with a helium white dwarf donor.

Using the constraints from the observations outlined above, we use the stellar evolution code `MESA` (Paxton et al., 2011, 2013; Paxton et al., 2015) to put constraints on the nature of the sdOB star. We then take the most likely model and evolve it forward in time to generate predictions about the future of this system.

Table 6.2 Overview of the derived parameter for OW J0741.

Right ascension	RA [hrs]	07:41:06.1
Declination	Dec [°]	–29:48:11.0
Visual magnitude	$m_{\rm g}$	20.02±0.11
Atmospheric parameter of the sdOB		
Effective temperature	$T_{\rm eff}$ [K]	39 400±500
Surface gravity	$\log g$	5.74±0.09
Helium abundance	$\log y$	–0.14±0.06
Orbital parameter		
	T_0 [MHJD]	$57695.611284 \pm 1.66 \times 10^{-4}$
Orbital period	$P_{\rm orb}$ [min]	$44.66279 \pm 1.1 \times 10^{-4}$
RV semi-amplitude	K [km s^{-1}]	422.5 ± 21.5
System velocity	γ [km s^{-1}]	-14.0±11.5
Binary mass function	$f_{\rm m}$ [$M_\odot$]	0.242±0.020
Derived parameter		
Mass ratio	$q = \frac{M_{\rm sdOB}}{M_{\rm WD}}$	0.38 ± 0.06
sdOB mass	$M_{\rm sdOB}$ [$M_\odot$]	0.35 ± 0.07
sdOB radius	$R_{\rm sdOB}$ [$R_\odot$]	0.13 ± 0.01
WD mass	$M_{\rm WD}$ [$M_\odot$]	0.90 ± 0.08
Orbital inclination	i [°]	54.7 ± 2.8
Separation	a [$R_\odot$]	0.44 ± 0.02
Distance	d [kpc]	8.2 ± 1.7

6.3.1 He-star model

We first test a model with the canonical sdOB mass of $0.462 M_\odot$ with a hydrogen envelope mass of $2.5 \times 10^{-4} M_\odot$. We find that after core He burning and during shell

He burning, this model spends ≈4 Myr in crossing the observation box (see dot-dashed purple line in Fig. 6.7). There are, a few problems with the system being in this state. First, given the $\log g$, orbital period, and mass ratio, this model fills its Roche lobe (RL) at orbital periods > 50 minutes, meaning that the higher mass (compared to the derived mass from observations) implies a radius larger than the current RL [1]. Second, the derived mass ratio from observations implies that if the He star had a mass of $0.46 M_{\odot}$, the compact companion must be super-Chandrasekhar as well as that the derived mass from the observations is inconsistent with the canonical sdOB mass.

We also tested models between $0.325 M_{\odot}$ and $0.462 M_{\odot}$ that experienced He core burning, and found that during the He core burning stage, $T_{\rm eff}$ was too low and $\log g$ was too high to match the measurements. If the models were massive enough to experience He shell burning, this stage reached higher $T_{\rm eff}$ values, but with similar $\log g$ values to the He core burning stage. Therefore, only He shell burning models near $0.462 M_{\odot}$ were able to match the $T_{\rm eff}$ and $\log g$ measurements.

6.3.2 He white dwarf model

In a second scenario, we consider the 'sdOB' star is a helium white dwarf (He WD) which did not start helium burning. If we assume that the star is a He WD that is just coming out of a CE event, then the $T_{\rm eff}$ and $\log g$ observation box gives a solution of a unique mass (Althaus et al., 2013). Figure 6.7 shows that this mass must be $0.320 M_{\odot}$, shown by the middle solid curve. This model spends ≈220,000 years in the observation box and has a post CE age of ≈1.1 Myr.

He WDs of this mass range experience diffusion-induced H novae (Althaus et al., 2001), and the tracks of these novae pass through the same $\log g$ values, but at higher

[1] Given the length of the He core burning phase, this system would have a wider orbit during He core burning and avoid Roche Lobe overflow at that phase of evolution

$T_{eff}$for a given stellar mass. Therefore, we can construct a lower mass He WD model ($0.242 M_{\odot}$) that has a too low T_{eff}just out of the CE but passes through the observation box after the first diffusion-induced H-nova. This is shown by the orange dashed curve in Figure 6.7. This model spends ≈66,000 years in the observation box and has a post CE age of ≈11 Myr. Since the $0.320 M_{\odot}$ He WD model is closer in mass to the derived mass from the observations, and spends more than a factor of 3 longer in the observation box, we conclude that the $0.320 M_{\odot}$ model is the most likely fit to our observations.

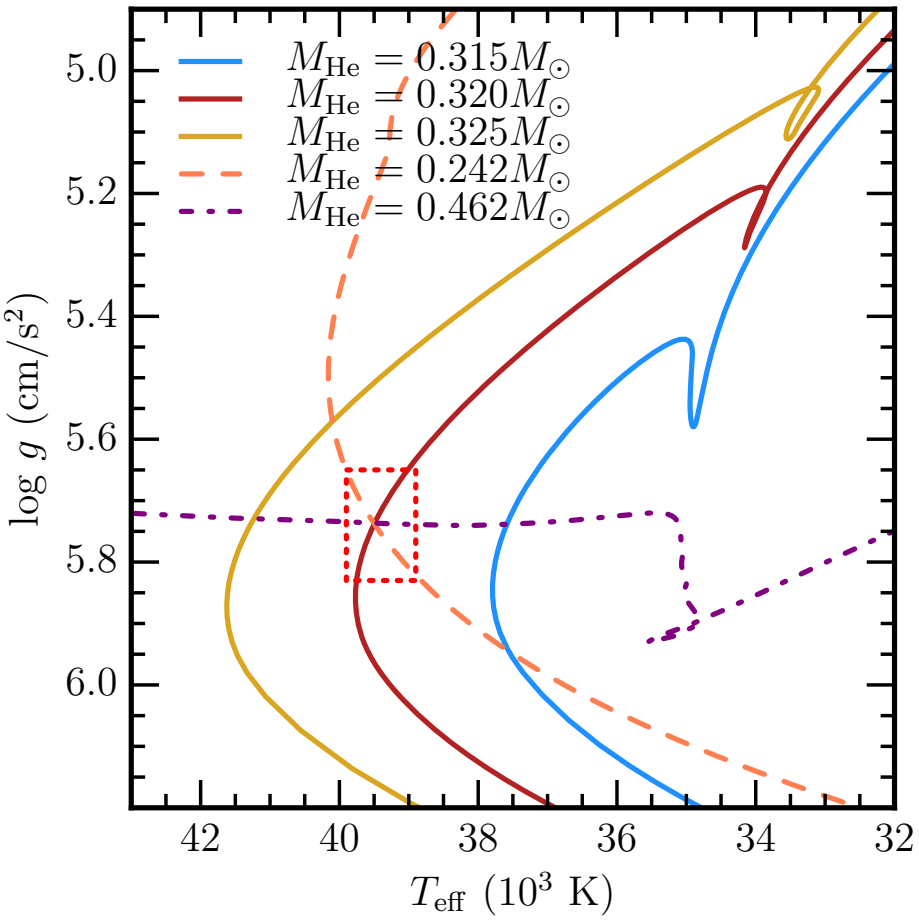

Figure 6.7 The red dotted line marks the observation box from the measurements and error bars given in Table 6.2. The three solid tracks are from He WD models of mass $0.315, 0.320$, and $0.325 M_\odot$ (right to left), where the $0.320 M_\odot$ model spends $\approx$220,000 years in the observation box and has a post CE age of $\approx$1.1 Myr. The orange dashed curve is from the $0.242 M_\odot$ model, which starts at the top of the plot, and spends $\approx$66,000 years in the observation box and has a post CE age of $\approx$11 Myr. The purple dot-dashed curve is from the $0.462 M_\odot$ model, which starts at the right of this plot and spends $\approx$4 Myr in the observation box and has a post CE age of $\approx$130 Myr.

6.3.3 Future Predictions

To predict the future of OW J0741, we use our best fit model for the sdOB, a $0.320 M_\odot$ He WD, and, given the mass ratio, a $0.85 M_\odot$ WD companion. As mentioned above, WDs

in the mass range considered for the sdOB experience diffusion-induced hydrogen novae. This model experiences its first H-nova 4.1 Myr after passing through the observation box and expands to fill its RL at an orbital period of 40.6 minutes. Depending on the amount mass loss through Roche Lobe overflow (RLOF) during this hydrogen nova, the model may experience a second hydrogen nova.

The subsequent evolution is governed by gravitational wave (GW) radiation which shrinks the orbit. Because the WD contraction occurs faster than the orbital decay the He WD begins RLOF after 17.6 Myr, at an orbital period of 5 minutes. For the given mass ratio, OW J0741 is definitely stable according to the dynamical instability (Nelemans et al., 2001), but definitely unstable according to the mass ratio criterion for direct impact accretion. Therefore, whether or not this system will be stable to mass transfer depends on the spin-orbit synchronization timescale, τ_s (Marsh et al., 2004) of the accreting WD. The physics that determine the value of τ_s is uncertain and previous estimates for systems of this type differ by more than 10 orders of magnitude (Campbell, 1983, 1984; Fuller & Lai, 2014).

According to the figures 1 and 5 from Marsh et al. (2004), the stability of this system requires a synchronization timescale of $\tau_s \lesssim 10$ yr. If the synchronization timescale is longer than this, then the WD accretor will extract enough of the orbital angular momentum into its spin angular momentum to cause a merger, leading to an R CrB configuration. If instead the synchronization timescale is short enough, the spin of the accreting WD can couple to the orbit and feed back enough angular momentum to avoid a merger, leading to a stable mass transferring system. In this case, the He WD itself will begin transferring degenerate helium at an orbital period of 3 minutes leading to mass transfer rates of $\approx 3 \times 10^{-6} M_\odot$/yr. The accreting WD experiences two small He novae before transitioning to steady He shell burning, leading to the growth of the C/O core. The mass transfer rate during this phase exceeds the stable burning rate (Brooks

et al., 2016), implying mass loss from the binary and an RL filling accretor. An intriguing possibility in this phase is the inhibition of direct impact accretion due to the accretor fully filling its RL. This may enhance the likelihood of stable mass transfer for these systems. As more mass is transferred, the orbital period increases and the mass transfer rate drops below the minimum steady burning rate and begins mild He flashes that are eventually strong enough to remove mass via RLOF in short ejection episodes. The last and largest of these flashes (Shen et al., 2010) involves only $10^{-2}M_{\odot}$ and unambiguously remains hydrostatic. After the last flash, the accreting WD quiescently grows to $1.04M_{\odot}$, with a $0.94M_{\odot}$ C/O core.

6.4 US 708: Hypervelocity He-rich subdwarf O-star

The hypervelocity star (HVS) US 708 is the only HVS that is not a normal main-sequence star (Geier et al., 2015). Instead, this star is a He-rich subdwarf O-star (He sdO), which are known to be formed by binary interaction stripping off the H-rich envelope. Furthermore, most HVSs are presumed to be accelerated by the Hills mechanism (Hills, 1988) during an encounter with the supermassive black hole at the center of the galaxy, whereas the galaxy center can be excluded from US 708's origin given the velocity vector measurements.

The mechanism that Geier et al. (2015) propose suggests that US 708 is the ejected donor remnant of a thermonuclear SN Ia (Wang et al., 2009; Justham et al., 2009), where the progenitor scenario is likely a $0.3M_{\odot}$ He star with a massive C/O WD ($1.0-1.2M_{\odot}$) in a 10 minute orbital period. In this scenario, the He star donates helium slowly enough that a large enough helium layer builds up on the accreting WD such that when it ignites, it triggers a detonation (Bildsten et al., 2007a; Shen & Bildsten, 2009; Shen et al., 2010) that in turn triggers a second detonation in the C/O core center, leading to a SN Ia

(Woosley & Kasen, 2011; Shen & Bildsten, 2014). The high orbital velocity and sudden unbinding of the companion give the He sdO its velocity.

We constructed several `MESA` models (Paxton et al., 2011, 2013; Paxton et al., 2015) to test this scenario, with the first criterion of finding a model that passes through the given $\log g$, $T_{\rm eff}$ observation box, $T_{\rm eff} = 47200 \pm 400$, $\log g = 5.69 \pm 0.09$. For He stars near this mass, they only reach effective temperatures after He core burning finishes, but the He shell burning is too weak to expand the radius to the low $\log g$ values observed. He stars of mass $\approx 0.8 M_\odot$ pass through observation box during the He core burning phase, but we were unable to find any He star model that passes through the observation box after donating $\gtrsim 0.05 M_\odot$ of helium, whether the mass loss happened before, during, or after He core burning.

We were, however, able to construct low mass helium WDs with surface hydrogen that pass through the observation box (Althaus et al., 2013). These He WDs contract after they are stripped of the H envelopes, but reach the observed $\log g$ values only $\approx$1 Myr post C.E., much shorter than the elapsed time since the calculated last pass through the galactic disk, 14.0 ± 3.1 Myr ago. Low mass He WDs with sufficient surface H experience diffusion-induced H novae (Althaus et al., 2001), and the tracks of these novae pass through the same $\log g$ values, but at higher $T_{\rm eff}$ for a given stellar mass. The first of these flashes brings the model back to the observed $\log g$ values, but only $\approx$10 Myr post C.E.. The max $T_{\rm eff}$ that these flashes experience is very sensitive to the mass of the H envelope, so we constructed models with He core masses of $0.255, 0.270$, and $0.285 M_\odot$ that pass through the observation box $40, 29$, and 14 Myr post C.E., respectively, after their second diffusion induced H-flash. These models show roughly equal amount of surface H and He by mass.

If we take the radius of the $0.285 M_\odot$ model just after stripping the H envelope and say that it is RL filling with a $1.2 M_\odot$ WD companion, we calculate an orbital period

of ≈36 minutes and orbital velocity of ≈700km/s. At that separation, given a kinetic energy from the SN of 10^{51} ergs, there is more than enough energy impacting the surface of the He WD to accelerate the He star to the observed velocities. Since the donor still has significant H surface layer, it must have been donating solar material to the massive WD, instead of He rich matter, as suggested by Geier et al. (2015). The biggest problem with this scenario is the ability of accretion of solar material to trigger a SN Ia. Prialnik & Kovetz (1995) and Yaron et al. (2005) show that accretion of solar material onto WDs, at the rates appropriate for this sort of binary configuration, produces no significant net growth of the WD mass, and therefore, could not grow to $M_{\rm Ch}$ or build He layers big enough to detonate when ignited. The lack of a known trigger for a SN Ia is the biggest caveat for the scenario we propose here.

Chapter 7

Fast and Luminous Transients from the Explosions of Long Lived Massive White Dwarf Merger Remnants

We study the evolution and final outcome of long-lived ($\approx 10^5$ years) remnants from the merger of a He white dwarf (WD) with a more massive C/O or O/Ne WD. Using Modules for Experiments in Stellar Astrophysics (`MESA`), we show that these remnants have a red giant configuration supported by steady helium burning, adding mass to the WD core until it reaches $M_{\rm core} \approx 1.12 - 1.20 M_{\odot}$. At that point, the base of the surface convection zone extends into the burning layer, leading to mixing of the helium burning products (primarily carbon and magnesium) throughout the convective envelope. Further evolution depletes the convective envelope of helium, and dramatically slows the mass increase of the underlying WD core. The WD core mass growth re-initiates after helium depletion, as then an uncoupled carbon burning shell is ignited and proceeds to burn

the fuel from the remaining metal-rich extended envelope. For large enough initial total merger masses, O/Ne WD cores would experience electron-capture triggered collapse to neutron stars (NSs) after growing to near Chandrasekhar mass ($M_{\rm Ch}$). Massive C/O WD cores could suffer the same fate after a carbon-burning flame converts them to ONe. The NS formation would release $\approx 10^{50}$ ergs into the remaining extended low mass envelope. Using the STELLA radiative transfer code, we predict the resulting optical light curves from these exploded envelopes. Reaching absolute magnitudes of $M_V \approx -17$, these transients are bright for about one week, and have many features of the class of luminous, rapidly evolving transients studied by Drout and collaborators.

The merger of two WDs is thought to have a wide range of possible outcomes depending on the mass and composition of the WDs (e.g., Webbink, 1984; Iben & Tutukov, 1984; Dan et al., 2014; Shen, 2015). In this work, we study the outcome of the merger of a He WD with a massive C/O or O/Ne WD. While such binary systems necessarily have lower mass ratios ($M_{\rm donor}/M_{\rm accretor} \lesssim 2/3$), they may still merge on contact due to weak spin-orbit coupling during the direct impact accretion phase (Marsh et al., 2004; Brown et al., 2016) or due to dynamical friction within the expanding ejected shell from a H nova (Shen, 2015). The mergers of He WDs with C/O WDs of mass $\approx 0.6 M_\odot$ are believed to form the hydrogen-deficient, carbon-rich supergiant R Coronae Borealis (RCB) stars (Clayton, 2012, 2013); in this scenario, the merger leads to a stably burning helium shell on top of the more massive WD core and this configuration endures for the timescale over which the burning shell consumes the massive He envelope ($\approx 3 \times 10^5$ yr).

In the case of higher mass C/O WDs, many have investigated the possibility of a helium detonation occurring during the merger and leading to a subsequent detonation of the C/O core (Guillochon et al., 2010; Woosley & Kasen, 2011; Pakmor et al., 2013; Shen & Moore, 2014; Dan et al., 2015). We are considering an alternative evolution where the large mass of helium forms a giant envelope surrounding the massive (C/O or

O/Ne) WD core that burns for $\approx 10^5$ years. Our calculations show the possibility of an unusual explosive outcome upon reaching a near Chandradeskhar mass ($M_{\rm Ch}$) core.

Models of stars with helium-burning shells on top of cold, degenerate (WD-like) cores have been previously constructed. Evolutionary calculations have focused on modeling the lower mass RCB stars and so have not considered massive O/Ne cores (Weiss, 1987; Saio & Jeffery, 2002; Zhang & Jeffery, 2012; Menon et al., 2013; Zhang et al., 2014). Static models have been used to explore helium-shell burning configurations at higher core masses (Biermann & Kippenhahn, 1971; Jeffery, 1988; Saio, 1988), but models with significant envelopes and core masses $\gtrsim 1.1 - 1.2 M_\odot$ were reported to be difficult to construct. This paper is the first to study the evolution of the merger remnants of double WDs that have total masses close to or greater than the Chandrasekhar mass ($M_{\rm Ch}$) and whose degenerate cores can grow to $M_{\rm Ch}$ via stable helium shell burning and later C shell burning. We focus on O/Ne ($1.10 - 1.20 M_\odot$) WDs merging with $0.40 M_\odot$ He WDs. We additionally evolve merger remnants of He WDs with massive C/O ($0.86 - 1.0 M_\odot$) WDs as a means to further study the He shell burning process on massive WD cores.

In models with O/Ne WD cores that reach core masses near $M_{\rm Ch}$, electron captures in the center will lead to a collapse of the core to a neutron star (NS) in a process very similar to accretion induced collapse (AIC) and electron-capture supernovae (ECSNe) (Nomoto et al., 1979; Miyaji et al., 1980; Nomoto, 1987; Canal et al., 1990; Nomoto & Kondo, 1991; Woosley & Baron, 1992; Ritossa et al., 1996; Dessart et al., 2006; Metzger et al., 2009; Darbha et al., 2010; Piro & Kulkarni, 2013; Takahashi et al., 2013; Tauris et al., 2013). We show here that the expected explosion energies of $\approx 10^{50}$ ergs (Kitaura et al., 2006; Dessart et al., 2006) and envelope masses $\approx 0.1 M_\odot$ imply that the resulting transients should be luminous ($L > 10^{43}$ erg s^{-1}) and rapidly evolving, similar to the class of rapidly evolving transients identified by Drout et al. (2014). Other possible members of this class are 2002bj (Poznanski et al., 2010) and 2010X (Kasliwal et al., 2010). We

use the recent MESA integration (Paxton et al. in preparation) of STELLA to generate light curves from our more massive models and compare them to the objects in Drout et al. (2014).

In §7.1, we discuss the growth of massive WD cores and show that the He burning layer eventually couples to the convection zone. We explore the post-coupling evolution and uncoupled C shell burning in §7.2. Then in §7.3 we use STELLA to generate light curves from our more massive models and compare them to the objects in Drout et al. (2014). We discuss the future of simulations and observations of these types of objects in §7.4.

7.1 Growth of the Degenerate Core

Using the stellar evolution code MESA (r9793) (Paxton et al., 2011, 2013; Paxton et al., 2015), we constructed idealized models of WD merger remnants by creating C/O WDs of masses $0.86, 0.92$, and $1.00 M_{\odot}$ and O/Ne WDs of masses 1.10 and $1.20 M_{\odot}$ through the same methods as in Brooks et al. (2016, 2017b). We add a $0.40 M_{\odot}$ envelope composed of 98% ^{4}He, 1% ^{14}N, and 1% other metals, corresponding to the approximate core compositon of a solar metallicity He WD of this mass. We then relax the envelope to a constant entropy of 10^{9} erg cm^{-3} K^{-1}, and the core to a constant temperature equal to the center temperature after 10 Myr (for consistency between models) of cooling after WD formation, typically $T_{c} = 3 - 7 \times 10^{7}$ K. This envelope entropy and core temperature prescription approximates a configuration immediately following a merger (Benz et al., 1990; Dan et al., 2014; Schwab et al., 2016). We then evolve the models forward in time. Due to the initially compact configuration, the models start with a nuclear burning flash at the base of the core/envelope interface that expands the envelope into a red giant. After this initial flash, the models steadily burn He and deposit the C/O ashes onto

the core. Much like a H shell burning red giant branch star, this helium burning layer powers an overlying convection zone that extends out to the surface. Our calculations make use of low-temperature opacities ($\log T/\mathrm{K} < 4.5$) that include the effects of carbon enhancement. We generate a set of tables with X = 0, Z = 0.02, and a range carbon enhancement factors (varying from 1 to 100) using the ÆSOPUS web interface (Marigo & Aringer, 2009). We incorporate these tables in `MESA` using its `other_kap` hook.

7.1.1 `MESA` Models

Since the He burning shell is being fed by the large He envelope, instead of accretion from a binary companion, the He shell burns at the maximum rate allowed by the core mass-luminosity relation (Kippenhahn, 1981; Jeffery, 1988), which coincides with the maximum steady helium

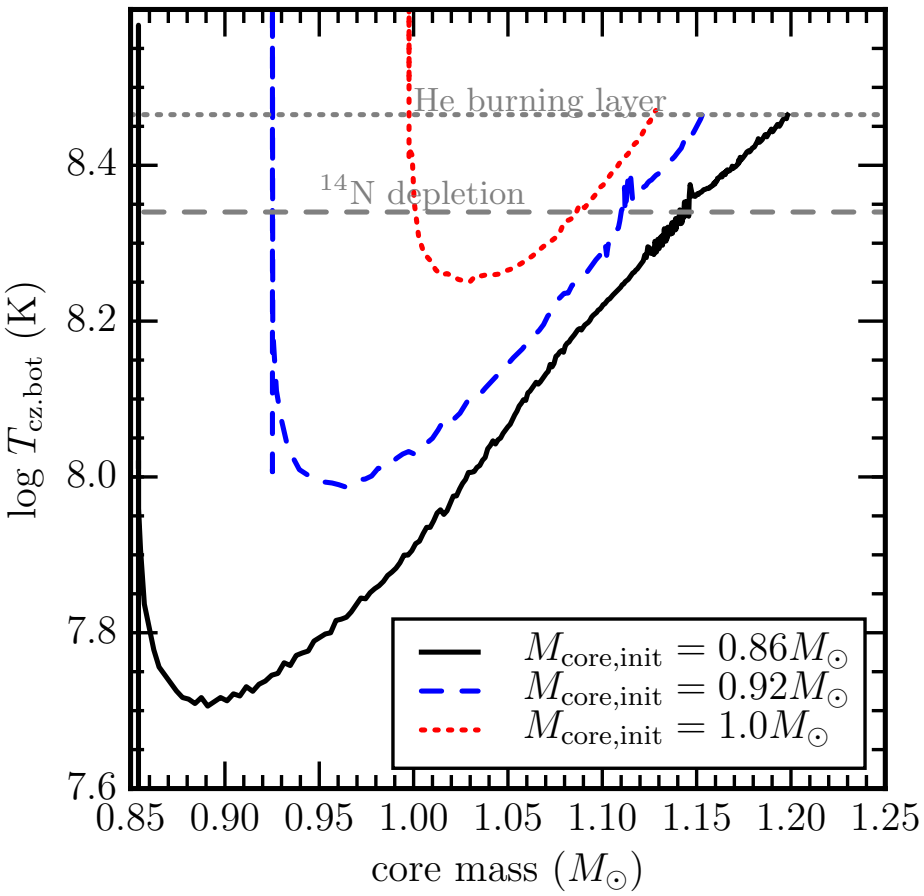

Figure 7.1 Temperature at the base of the convection zone as a function of core mass for three models with initial core masses of $0.86, 0.92$, and $1.00 M_\odot$. The temperature at which ^{14}N is depleted from the envelope is shown by the grey dashed line. The temperature of the helium burning layer is shown by the grey dotted line. The burning layer and convective zone effectively couple when the $T_{\rm cz,bot} = T_{\rm He\,burn}$.

burning rate (Piersanti et al., 2014; Brooks et al., 2016, $\approx 3 - 4 \times 10^{-6} M_\odot$/yr). For the model that starts with a core mass of $0.86 M_\odot$, the burning has settled from the initial flash and becomes steady when the core has grown to $0.90 M_\odot$ (black solid line in Figure 7.1). At that point, the model has a surface luminosity of $L_{\rm surf} = 37,600 L_\odot$ compared to a burning luminosity of $L_{\rm burn} = 31,300 L_\odot$, with an effective temperature of $T_{\rm eff} = 13,500$ K, radius of $35 R_\odot$, and surface opacity of $\kappa_{\rm surf} = 0.16$ cm^2/g, which agree well with the

models from Saio & Jeffery (1988); Jeffery (1988). As the core mass grows, the convection zone extends deeper in to higher temperatures. In 10^5 years this model reaches a core mass of $M_{\rm core} = 1.20 M_\odot$, with $T_{\rm eff} = 12,800$ K and a radius of $63 R_\odot$.

In Figure 7.1 we show the temperature at which ^{14}N is depleted from the envelope. We derive this temperature by integrating the rate of alpha captures onto ^{14}N over the entire convective envelope and finding the temperature at which the timescale of ^{14}N depletion from the envelope is 10^4 yr, approximately 5% of the lifetimes of these stars. The ^{14}N depletion timescale is calculated via

$$\frac{1}{t_{14}} \equiv \frac{d \ln X_{14}}{dt} = \frac{Y}{4 m_p M_{\rm conv}} \int_{M_{\rm conv}}^{M_*} \rho \langle \sigma v \rangle dM. \tag{7.1}$$

Performing the same calculation for ^{18}O shows that its depletion temperature is only 5% higher than that for ^{14}N, so there is negligible time to see an enhancement of ^{18}O through this mechanism.

During this phase of helium shell burning, the models studied in this paper share similarities to R Coronae Borealis (RCB) stars (Clayton, 2012). Several RCB stars have been observed to have significantly enhanced amounts of ^{18}O on their surfaces, which favors the double WD merger scenario (Clayton et al., 2007; Menon et al., 2013). The number of known RCB stars then implies a WD merger rate of 1 per 100 years in our galaxy, consistent with population synthesis expectations and observed double degenerate binaries (Alcock et al., 2001; Jeffery et al., 2011; Zhang & Jeffery, 2012; Zhang et al., 2014; Karakas et al., 2015; Brown et al., 2016). By measuring the semi-regular stellar pulsations from RCB stars, their masses are derived to be in the range of $\sim 0.8 - 0.9 M_\odot$ (Saio, 2008), which agrees well with the binary population synthesis from Han (1998).

Due to their higher core masses, the models shown here are at least a factor of a few more luminous than the typical RCB star. The higher $T_{\rm eff}$ of the models means they

would likely be better observationally classified as extreme He stars (Jeffery, 2008a,b). As indicated in Fig. 7.1 and the related discussion, the higher temperatures at the base of the convective envelope would lead them to appear depleted in ^{14}N and ^{18}O for core masses $\gtrsim 1.05 M_{\odot}$.

The hot C/O ashes of He burning settle onto the core at such a high rate that a shell ignition of carbon occurs in the freshly accreted C/O ash layer at core masses of $1.2 - 1.3 M_{\odot}$ (Brooks et al., 2016), depending on the starting core mass and temperature. The ignited carbon develops into a flame that propagates inwards, which we do not follow. But this presumably converts the entire C/O core into O/Ne (Nomoto & Iben, 1985; Lecoanet et al., 2016). For an initially O/Ne core, this flame converts the C/O shell to O/Ne (Brooks et al., 2017b).

Hence, the cores of all massive WD merger remnants will be devoid of central carbon when the core mass grows to $M_{\rm Ch}$. For systems that start with a C/O WD primary, only the most massive systems have total masses $\gtrsim M_{\rm Ch}$, with the most massive case studied here having a total mass of $1.40 M_{\odot}$. The carbon flames in models with C/O cores will lift the core degeneracy upon reaching the center. Merger remnants with masses $\lesssim M_{\rm Ch}$ may complete nuclear burning at this stage and end up as cooling O/Ne WDs. Although these models, and those of lower mass, do not lead to the types of explosions we are interested in for this paper, they are useful in helping us describe the peculiar behavior of He burning shells on WD cores of masses $M_{\rm core} \approx 1.12 - 1.20 M_{\odot}$. Merger remnants with initially C/O cores and total masses $\gtrsim M_{\rm Ch}$ will grow cores massive enough that during Kelvin Helmholtz (KH) contraction they will ignite Ne off-center and follow the evolution described in Schwab et al. (2016). This involves the formation of a low mass Fe core, but still ends with the collapse to a NS.

7.1.2 Core Masses $> 1.1 M_\odot$

We find that as the degenerate cores of our models grow in mass, the base of the convection zone extends deeper into the model (see Figure 7.1) until it overlaps with the He burning shell when $M_{\rm core} \approx 1.12 - 1.20 M_\odot$ (the exact core mass at which this coupling happens depends on the history of the star, e.g. its initial core mass and temperature). Once the burning layer couples with the convective envelope, the burning products are no longer primarily deposited on the core, but a large portion of them are mixed with the entire envelope.

To understand why the convection zone base extends deeper into the star until it reaches the burning layer, we first must explain why the envelope is convective in the first place. We see in Figure 7.1 that even at core masses of $0.90 M_\odot$ the base of the convection zone extends to $\log T/{\rm K} = 7.7$. The reason for this is that He burning occurs at much higher temperatures and densities and lower opacities than H burning; high enough temperature that the Klein-Nishina relation becomes relevant (Buchler & Yueh, 1976). This means that opacity is increasing outwards from the burning layer as

$$\kappa_{\rm es} \approx 0.2 \left[1 + \left(\frac{T}{4.5 \times 10^8 \text{ K}} \right)^{0.86} \right]^{-1} \text{cm}^2 \text{g}^{-1}. \tag{7.2}$$

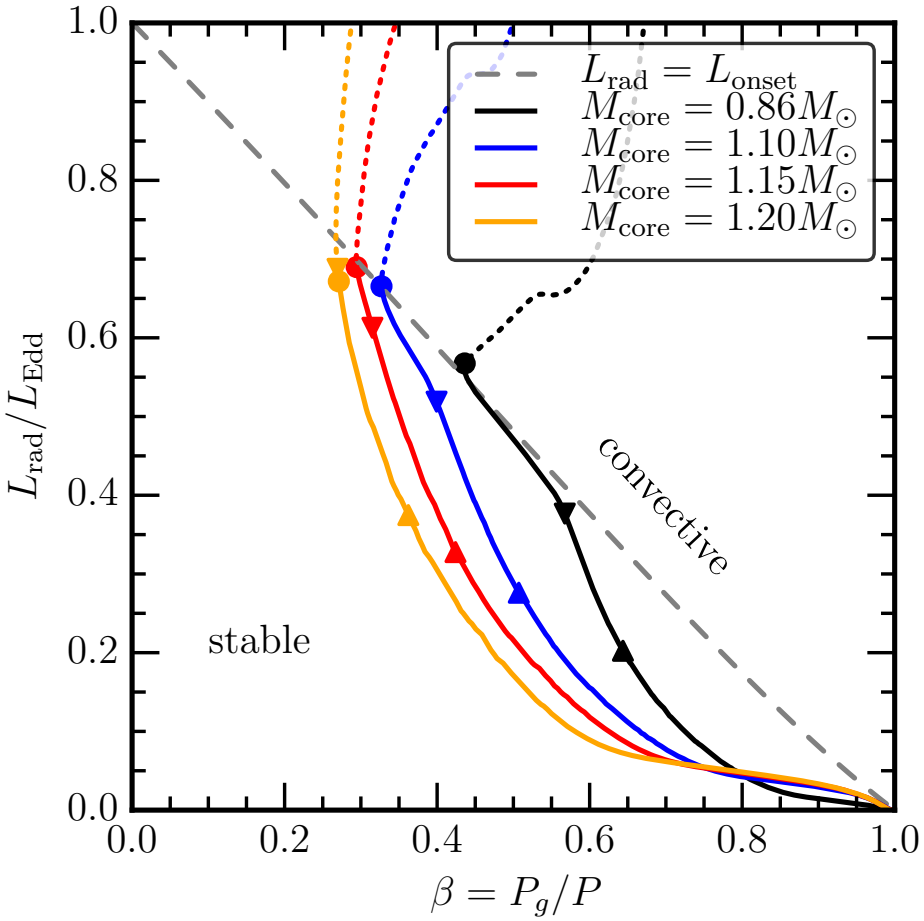

Figure 7.2 Profiles from the model with an initial core mass of $0.86 M_\odot$ are shown at various later core masses. The grey dashed curve is the convective instability line described by equation 7.3. The "up" triangles are where $L(r) = 0.5 L_{\rm surf}$, the "down" triangles are where $L(r) = 0.9 L_{\rm surf}$. The circles mark the base of the convection zone, and the profiles are solid in radiative regions and dotted in convective regions. Note how the "down" triangle on the last profile sits above the base of the convective layer, implying that burning is occuring in the convective envelope.

Furthermore, the core mass-luminosity relation is steeper for He shell burning sources than for H shell burning sources (Jeffery, 1988). This means that for a given core mass, at the burning layer, the He shell source will have higher radiation luminosity ($L_{\rm rad}$) and a smaller Eddington luminosity ($L_{\rm Edd}$) that decreases at larger radius. As we move out-

wards from the burning layer and κ is increasing, we encounter a point where $L_{\rm rad}/L_{\rm Edd}$ exceeds the convective instability criterion described in Joss et al. (1973); Paxton et al. (2013):

$$\frac{L_{\rm rad}}{L_{\rm Edd}} > \frac{8(1-\beta)(4-3\beta)}{32-24\beta+3\beta^2}, \tag{7.3}$$

where $\beta = P_g/P$, shown by the grey dashed line in Figure 7.2. This shows that the reason for deep convection in these models is that the local luminosity just above the burning layer is approaching $L_{\rm Edd}$.

Since we know that the burning luminosity increases with $M_{\rm core}$ more rapidly than $L_{\rm Edd}$ does (Kippenhahn, 1981; Jeffery, 1988), the ratio $L/L_{\rm Edd}$ must increase with $M_{\rm core}$. This means that as the core mass grows and we follow the $L_{\rm rad} = L_{\rm onset}$ grey dashed line up to higher values of $L_{\rm rad}/L_{\rm Edd}$, the base of the convection zone must have a decreasing β with increasing core mass. The convection zone base moves inwards to higher temperatures and thus lower values of β.

As the convection zone base moves deeper into higher temperatures, the mass between the burning layer and convection zone becomes smaller, which steepens the profiles in Figure 7.2, as there is a smaller region where both $L(r)$ and $\kappa(r)$ are relatively constant. This means that as $M_{\rm core}$ grows, the value of $L_{\rm rad}/L_{\rm Edd}$ at the base of the convection zone increases, which decreases the value of β at the base of the convection zone, which decreases the mass between the burning layer and convection zone (where both $L(r)$ and $\kappa(r)$ are relatively constant). This, in turn, steepens the profiles in Figure 7.2 leading to smaller values of β in the burning layer. As β decreases (radiation pressure increases) in the burning layer, the entropy rises rapidly until it is comparable with the entropy of the convection zone. At this point, the convective envelope couples to the burning layer, mixing a significant fraction of the burning products into the envelope.

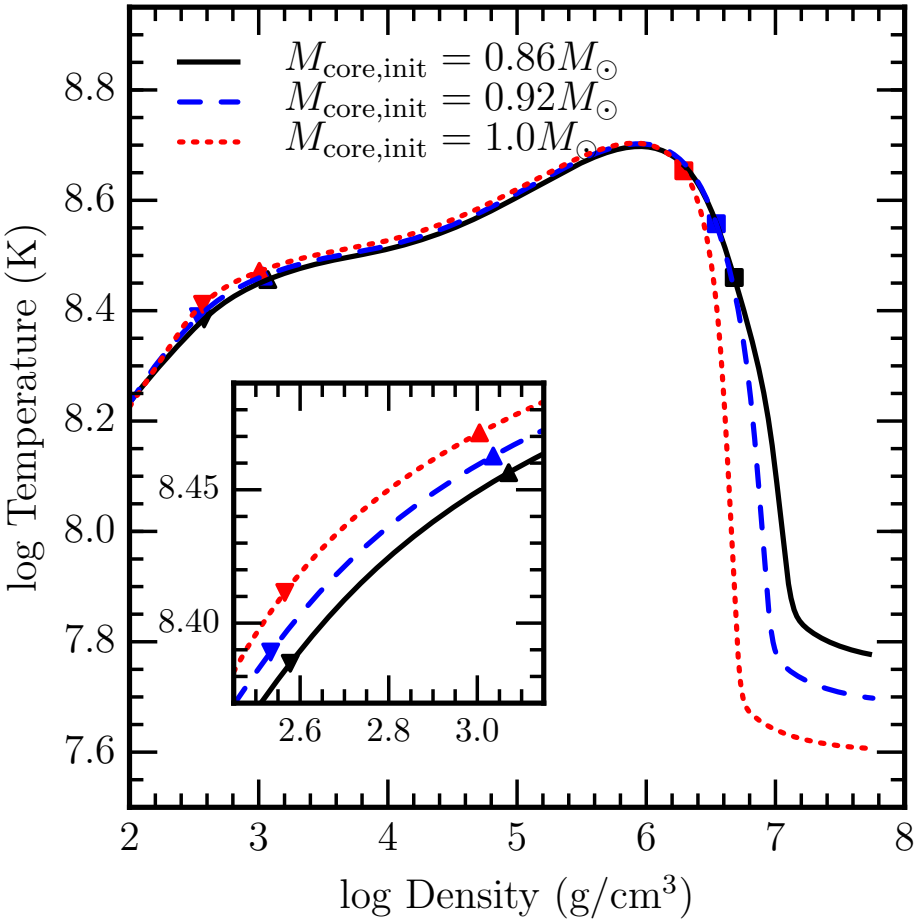

Figure 7.3 Profiles from different initial core masses at a common core mass of $1.10 M_\odot$. The "up" triangles are where $L(r) = 0.5 L_{\rm surf}$, the "down" triangles are where $L(r) = 0.9 L_{\rm surf}$. The squares mark the initial core mass coordinates. This plot emphasizes the effect of initial conditions on the density and temperature of the burning layer at a common core mass.

As we mentioned above and show in Figure 7.1, models with different starting masses experience the coupling between the burning layer and the convective envelope at different core masses. This is because this coupling is sensitive to the temperature, density, and the exent of the burning layer, which in turn depend on the history of the model. For a given core mass, models with higher initial core masses have less time for conduction to heat the core and have less freshly-burned ashes directly below the burning layer. This

leads to different core temperatures, luminosities, and radii for models with different initial core masses when compared at a common core mass (Figure 7.3).

From this point on in the paper, we will only discuss models that start with O/Ne WD cores, such that they will begin runaway electron captures in their centers upon reaching $M_{\rm Ch}$. Models that instead start with C/O WD cores will ignite carbon shell flames before reaching $M_{\rm Ch}$ that convert the entire C/O core to O/Ne and lift the core degeneracy, following the evolution described in Schwab et al. (2016). Even though such an evolution still may lead to the collapse of a degenerate core to a NS inside an extended envelope, the envelope masses will be much smaller (due to small initial C/O core masses). The resulting lightcurves would only last $\lesssim$a couple days, and are thus harder detect. We defer exploration of these explosions and light curves to future work.

7.2 Post-coupling Regimes

As discussed above, when the core mass grows large enough to cause the burning layer to couple with the convective envelope, the burning products are evenly

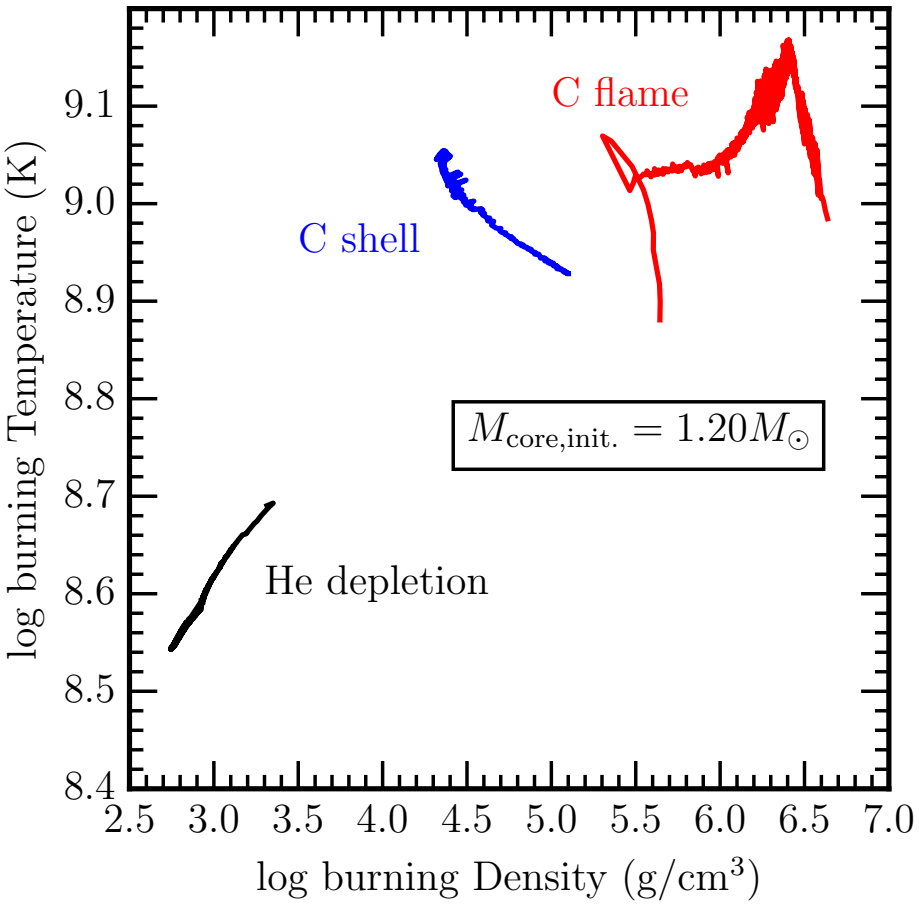

Figure 7.4 Evolution of the main burning layer during different stages for the model with $M_{\rm core,init.} = 1.20 M_\odot$. Due to the initially large core mass, the first phase of evolution depletes the envelope of He (black curve), followed by a C-flame (red curve) leading to C-shell burning (blue curve) powering the outer convection zone while keeping the radius $> 400 R_\odot$.

mixed throughout the convective envelope instead of primarily being deposited on the core. This then causes uniform depletion of helium in the envelope, and a rising metallicity. At the thermodynamic conditions present in the hot parts of the envelope, the default configuration of the `MESA` eos module uses the OPAL equation of state for $Z \leq 0.04$ (Rogers & Nayfonov, 2002). The OPAL tables do not extend to higher Z, and so for more metal-rich mixtures the `MESA` eos switches to using HELM (Timmes & Swesty, 2000),

which does not self-consistently include ionization. For the models presented in this paper we use the OPAL tables for $Z < 0.08$, using the $Z = 0.04$ table for $0.04 < Z < 0.08$. We use the HELM eos, assuming complete ionization, for $Z > 0.10$. We blend between the two over the interval $0.08 < Z < 0.10$. With this choice, we observe that the convective zone and burning layer remain coupled until the helium is largely depleted from the envelope[1].

[1] `MESA` provides an option to schematically include ionization when using HELM by blending from a version of HELM assuming complete ionization to one assuming a fully neutral composition. The location and extent of this blend (in temperature) is user-specified. We experimented with several blend locations, but all models that used this option were plagued by convergence errors caused by the blend. We were unable to evolve any of these models for sufficiently long durations to allow their core masses to grow to $M_{\rm Ch}$.

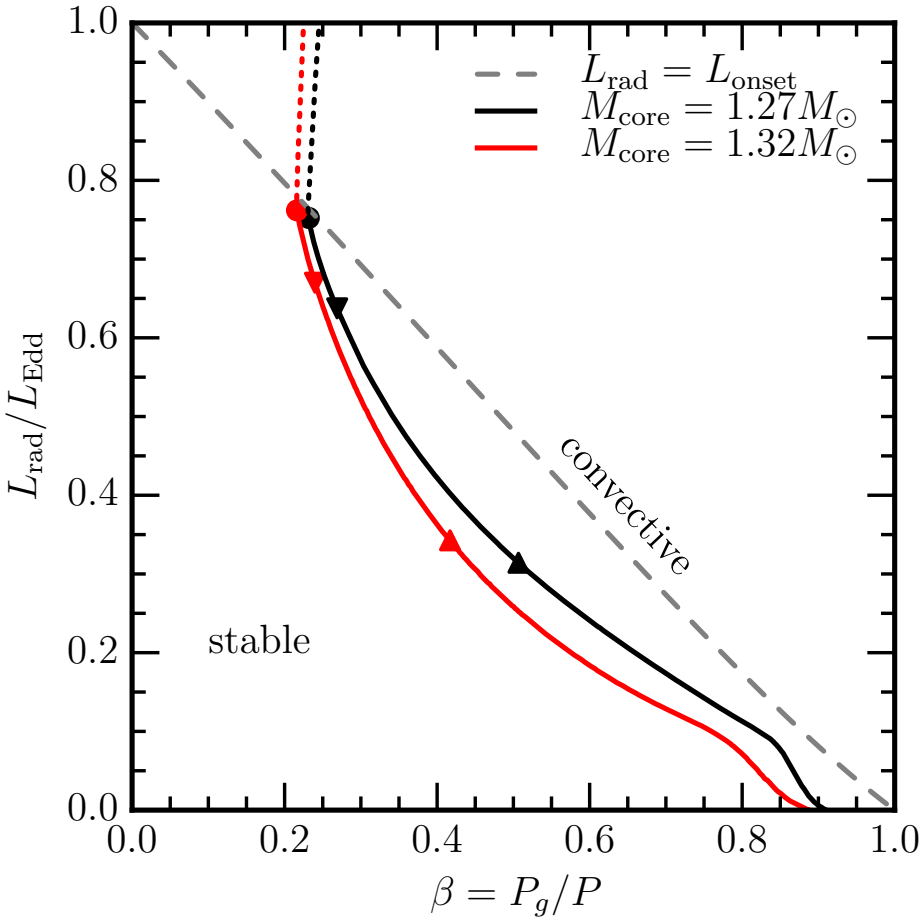

Figure 7.5 Same as Figure 7.2 but for a coupled simulation that burns all of its He and starts doing C-shell burning. These two profiles are from the C-shell burning phase. Note that during C shell burning, the burning layer and convective envelope are not coupled, so that C burning grows the mass of the degenerate core, leading to AIC.

Due to the large core masses (and small core radii), the helium burns at such high temperatures and densities that the ^{16}O nuclei produced are quickly consumed by α-captures, along with the ^{20}Ne nuclei, such that the composition of the envelope becomes ^{24}Mg rich, with significant amount of ^{12}C (mass fractions given in Table 7.1).

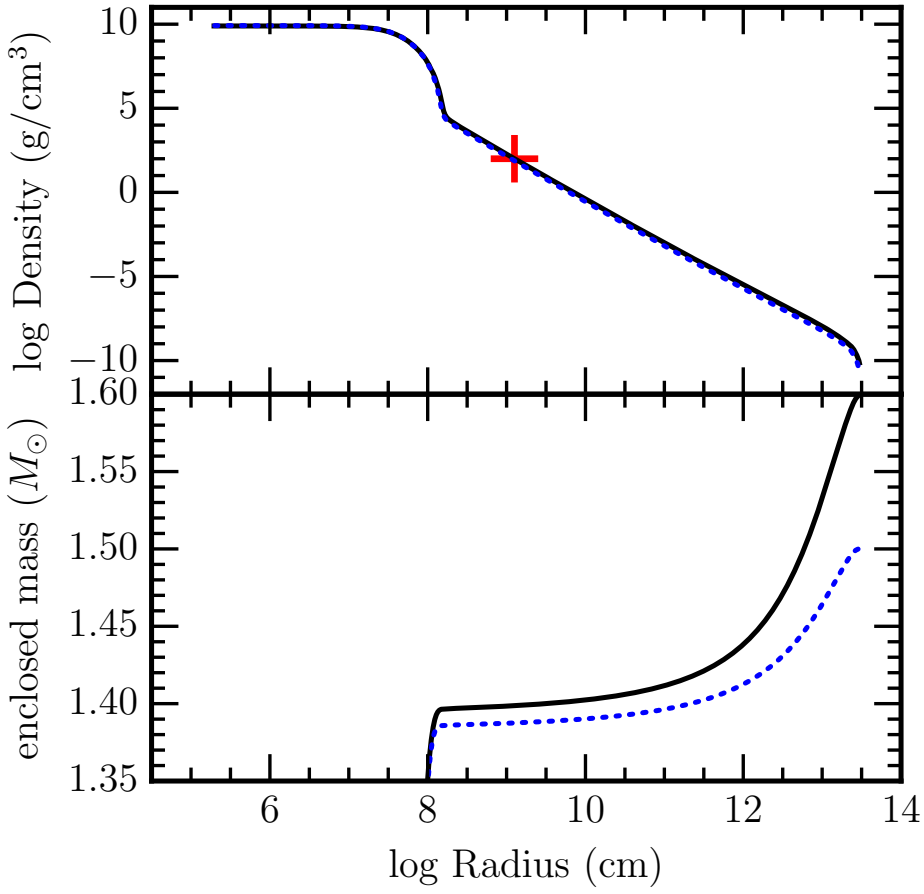

Figure 7.6 Profiles from the two models used for our explosion calculations when the core reaches conditions for AIC. Top Panel: Density structure. The red cross marks the mass coordinate at which we separate the core zones from the envelope zones and inject the SN energy. Bottom Panel: Mass profile, showing that most of the mass of the envelope is above the energy injection coordinate.

Once there is insufficient helium to power a burning layer to prop up the envelope, it begins to Kelvin-Helmholtz (KH) contract until the underlying carbon is ignited, and a carbon flame propagates through the existing C/O layer until it reaches the O/Ne core (Brooks et al., 2017b), as shown by the red curve in Figure 7.4. Once the flame is extinguished, the envelope continues to KH contract until the Mg/C layer reaches densities and temperatures high enough for carbon burning, shown by the blue curve

in Figure 7.4. This carbon shell burning powers the convective envelope and keeps the radius above $400R_{\odot}$. The carbon shell burning occurs at temperatures ($T = 8-11\times10^8$ K) and densities ($\rho = 2-13\times10^4$ g/cm^3) high enough that, even though the temperature at the base of the convection zone was just as hot as it was during helium depletion and only gets hotter as the core grows, the carbon burning layer remains decoupled from the convection zone (see Figure 7.5). This means that the composition in the envelope remains constant and uniform, as the underlying O/Ne core grows in mass, eventually triggering an AIC. Hence, for each super-Chandrasekhar mass model, there is a Mg/C envelope of mass $\approx0.1M_{\odot}$ above the O/Ne core, with a density structure shown in Figure 7.6.

7.3 Shock Heating the Envelopes

The collapse of the core to a NS releases a large amount of gravitational potential energy, which can be transformed to thermal/kinetic energy to power a bright transient. The steep density gradient present in our models is similar to that around O/Ne low mass Fe cores produced in single star evolution which are known to robustly lead to collapse to a NS and generate a shock energy of $\approx10^{50}$ ergs (Kitaura et al., 2006; Melson et al., 2015; Radice et al., 2017). The light curve will look different from that of canonical AIC (Woosley & Baron, 1992; Piro & Kulkarni, 2013) or a stripped-envelope electron capture supernova (Moriya & Eldridge, 2016), since the envelopes in our models extend out to $\sim$ a few$\times100R_{\odot}$, and thus produce much brighter light curves. They also look different from regular electron-capture SNe from $8-10M_{\odot}$ stars, due to the much smaller envelope masses, producing shorter light curves that lack hydrogen (Takahashi et al., 2013; Smith, 2013; Tauris, 2015; Jones et al., 2016).

We take the most massive models described in §7.1 and 7.2 after reaching core

masses near $M_{\rm Ch}$ such that electron captures in the core began (Schwab et al., 2015), and we remove the $1.4M_\odot$ cores just above the burning layer where $\log T/K = 8.3$, $\log \rho/{\rm g\,cm^{-3}} = 2$, and $r = 0.018R_\odot$ (marked by the red cross in Figure 7.6), and inject 10^{50} ergs of energy into the inner $0.01M_\odot$ of the remaining envelope over 5 milliseconds. The resulting shock then propagates through the envelope for about a third of a day, and when it is near the surface, we save data from the model and use it as input for the `STELLA` code. `STELLA` is an implicitly differenced hydrodynamics code that incorporates multigroup radiative transfer (Blinnikov & Bartunov, 1993; Blinnikov et al., 2006). `STELLA` typically uses about 100 frequency groups, enough to produce a spectral energy distribution, but not sufficient to produce spectra. The opacity is computed based on over 153,000 spectral lines from Kurucz & Bell (1995) and Verner et al. (1996). Opacity also includes photoionization, free-free absorption and electron scattering.

We use the two most massive envelope models, a $0.1(0.2)M_\odot$ envelope from the $1.5(1.6)M_\odot$ total mass model that started with a $1.1(1.2)M_\odot$ O/Ne WD core. At the time of explosion, the envelopes extended out to $410R_\odot$ and $426R_\odot$ for the $0.1M_\odot$ and $0.2M_\odot$ envelopes, respectively. The envelopes' composition is uniform and dominated by ^{24}Mg and ^{12}C, with mass fractions given in Table 7.1.

The light curves for these two models are shown in the top panel of Figure 7.7, with the photospheric velocities shown in the bottom panel. Figure 7.8 shows additional properties of these models. The reason for the short light curves and high photospheric velocities is the low ejecta mass; we are injecting SN energies into an envelope with a small fraction of the mass of the regular shock-powered type IIP SNe. The peak luminosity is that expected for the radiative losses of an expanding and cooling ejecta, while the duration is consistent with the time it takes for the ejecta to become optically thin.

Table 7.1. Elemental Mass Fractions in the envelopes at explosion

$M_{\rm env}/M_\odot$	^{24}Mg	^{12}C	^{20}Ne	^{16}O	^{28}Si	^{4}He
0.1	0.603	0.308	0.032	0.017	0.015	0.000
0.2	0.653	0.269	0.022	0.017	0.014	0.000

Note. — For both of the models studied in this section, we give the mass fractions of the dominant elements. Composition is uniform throughout the envelope for both models.

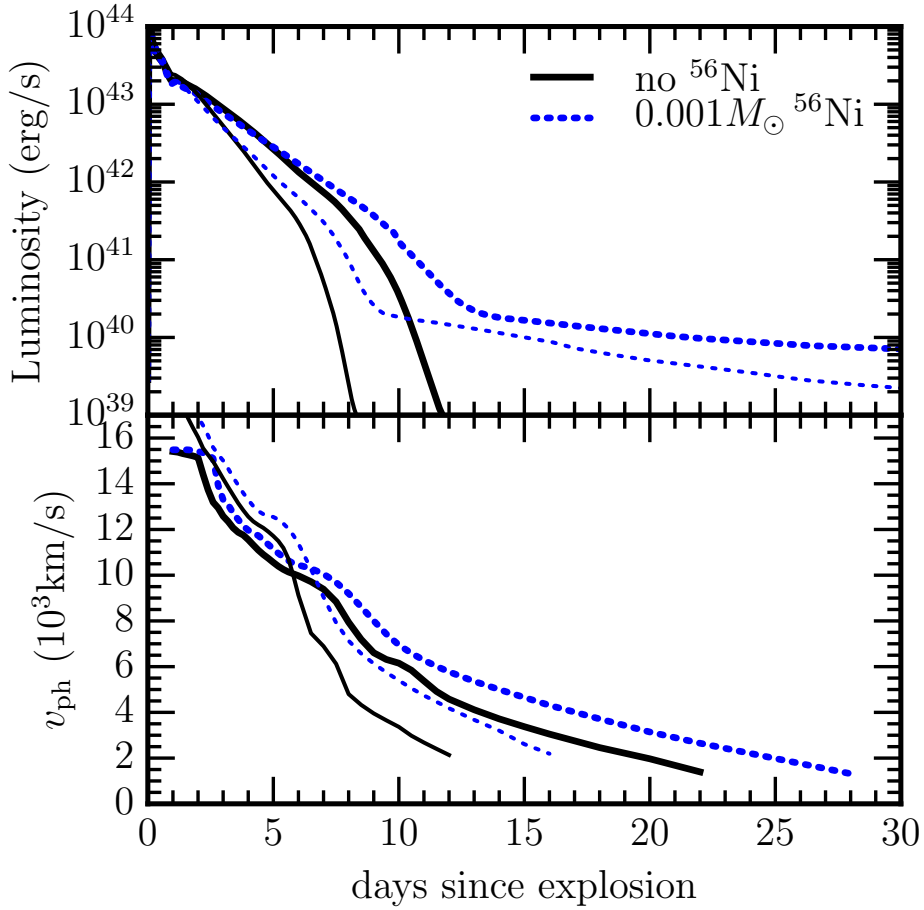

Figure 7.7 Bold curves are for the $0.2M_\odot$ model. Thinner curves are for the $0.1M_\odot$ model. Top panel: bolometric luminosity. Bottom panel: Photospheric velocites.

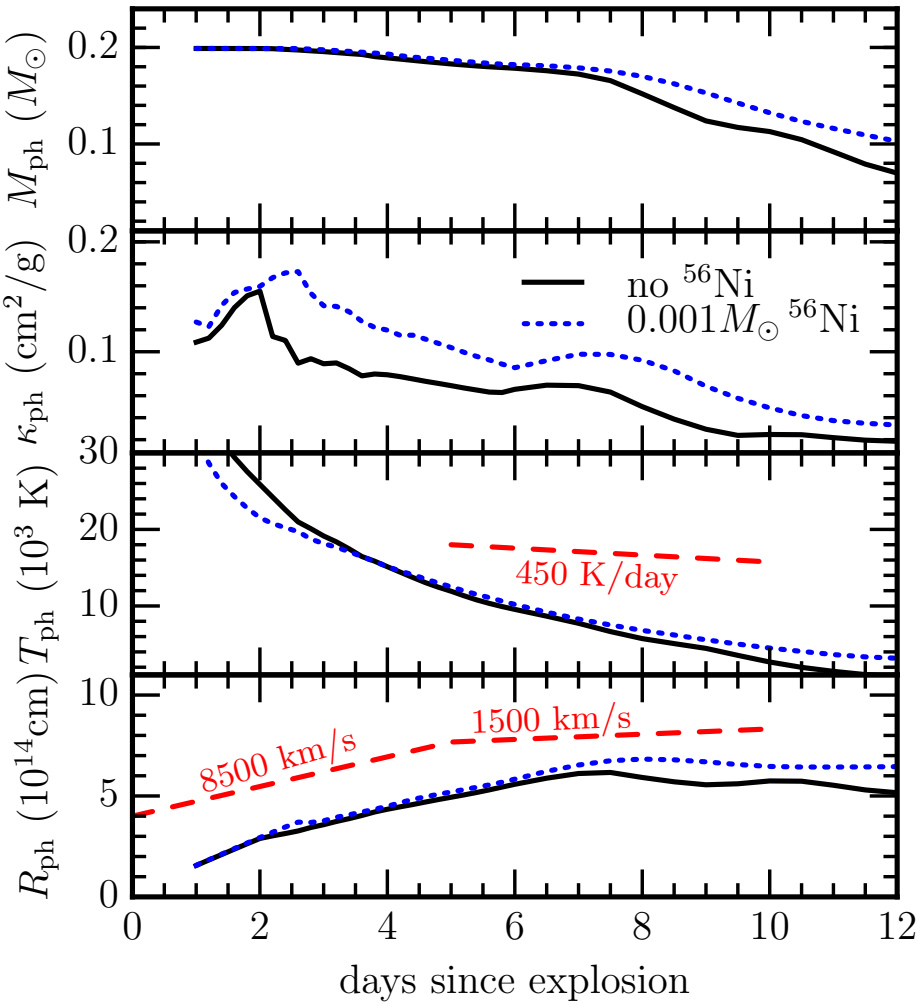

Figure 7.8 Additional properties from our STELLA radiation transfer calculations of explosions of $0.2M_\odot$ envelope with no ^{56}Ni (solid black curve) and with $0.001M_\odot$ of ^{56}Ni (dotted blue curve), same as in Figure 7.7. Top panel: mass coordinate of the photosphere. Second panel: Opacity at the photosphere. Third panel: Temperature of the photosphere. Bottom panel: Radius coordinate of the photosphere. The red dashed lines show fiducial cooling rates and photosphere expansion speeds based of the best observed object from Drout et al. (2014): PS1-10bjp.

The light curves through the filters B, V, I, and R show (Figure 7.9) that the peak in optical light occurs 3-4 days post-explosion for the $0.2M_\odot$ model. The rise time of the optical light curves is slightly faster than the decay time, but a modest amount of ^{56}Ni

may slow the decay time to be more consistent with the objects in Drout et al. (2014). An addition of $0.001M_{\odot}$ of ^{56}Ni in the inner $0.03M_{\odot}$ extends the visible light curve by ≈a day (shown in Figure 7.9). We found that $0.001M_{\odot}$ of ^{56}Ni was the minimum amount necessary to keep the bolometric luminosity above 10^{40} erg/s at day 20 after energy injection. Compare this to the $\approx 2.5 \times 10^{-4} M_{\odot}$ of ^{56}Ni found in AIC calculations by Dessart et al. (2006), but with only a total ejecta mass of $0.001M_{\odot}$, because these models did not have the extended envelope considered here. Additionally, we also varied the injection energy. A factor of 2 increase in the explosion energy leads to half of a magnitude increase in peak brightness and ≈a day decrease in light curve duration, and vice versa for a factor of 2 decrease in explosion energy.

From the selection criteria given in §2.2 of Drout et al. (2014), both of the explosion models shown here would be included in this new class of rapidly evolving luminous transients (see also Arcavi et al., 2016; Tanaka et al., 2016, for additional observational examples). Specifically, the transients rise by $\gtrsim$ 1.5 mag in the 9 days immediately prior to observed maximum light, and they decline by $\gtrsim$ 1.5 mag in the ∼25 days post observed maximum. The third selection criterion is that the transient must be present in at least three sequential observations. The relatively short light curves of these models, compared to the average timescales of transients in Drout et al. (2014), somewhat reduces the likelihood of obtaining three or more sequential observations.

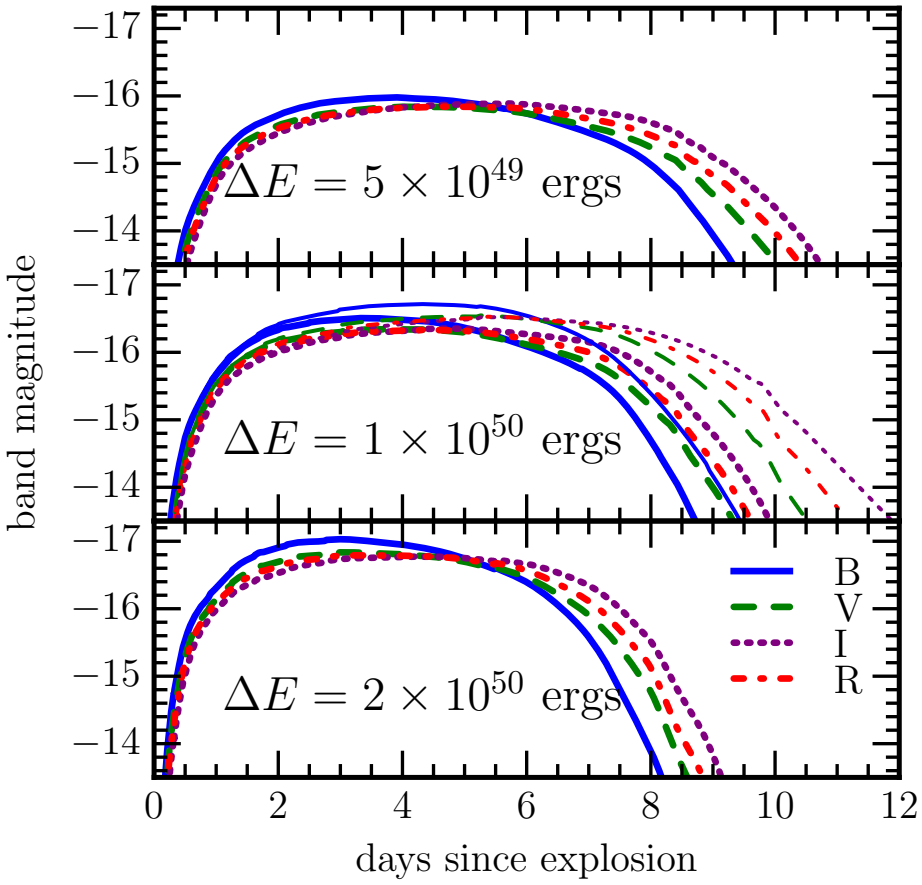

Figure 7.9 B, V, I, and R band light curves for Mg/C envelopes of $0.2M_{\odot}$ with explosion energies of $5e49$ ergs (top panel), $1e50$ ergs (middle panel), and $2e50$ ergs (bottom panel). The middle panel also includes a simulation with $1e50$ ergs and $0.001M_{\odot}$ of ^{56}Ni in the inner $0.03M_{\odot}$ of the envelope (thin lines).

7.4 Conclusions

We have presented the first evolutionary simulations of super-Chandrasekhar merger remnants of He and O/Ne WDs. The remnants expand to giant configurations supported by He burning shells that power extended convection zones. We have shown that upon reaching core masses $M_{\rm core} \approx 1.12 - 1.20 M_{\odot}$, depending on initial conditions, the base of

the surface convection zone extends deep enough into the burning layer that the burning products are no longer primarily deposited on the core, but mixed evenly throughout the convective envelope. This leads to He depletion and metal enrichment of the envelopes, resulting in uniform compositions dominated by ^{24}Mg and ^{12}C (see Table 7.1). Once the He is depleted and the Mg/C envelopes begin to KH contract, they ignite and steadily burn the ^{12}C in a shell, uncoupled to the convection zone, keeping the envelope extended above $400R_{\odot}$ when the core reaches conditions for electron capture induced collapse.

Our $1.6M_{\odot}$ model spends ≈7000 years in the C shell burning phase prior to reaching AIC conditions. The merger rate producing such systems is uncertain but the super-Chandrasekhar merger rate in the Milky Way is perhaps one every 1000 years (Badenes & Maoz, 2012) so that there could be several such C shell burning objects in the Galaxy and M31 at any time. Observatonally, these would appear as H deficient C stars, with an unusually high abundance of ^{24}Mg. The low $T_{\rm eff}$ mean that dust production might well be efficient, possibly leading to large mass loss rates in dust-driven winds and significant self-obscuration (Schwab et al., 2016). One significant uncertainty in our evolutionary calculations is that dust-driven winds can in principle be strong enough to decrease the mass of the remnant below $M_{\rm Ch}$, avoiding the collapse and explosion scenario we have explored in this paper. Unfortunately the physics of dust production and dust-driven winds under these conditions are not well enough understood to robustly determine whether or not the remnants will remain above $M_{\rm Ch}$.

Once the cores reach $M_{\rm Ch}$, electron captures in the center will lead to the collapse of the degenerate core to a NS. The resulting shock propagates through the envelope and generates a light curve as the ejecta expand. The light curve (Figures 7.7 and 7.9) is bright ($> 10^{43}$ erg s^{-1}) due to the extended ($> 400R_{\odot}$) envelope and short (∼a week) due to the low ejecta mass ($\approx 0.1M_{\odot}$).

These fast and luminous light curves fit many of the observed features of a class of

rapidly evolving luminous transients (Drout et al., 2014), including peak brightness ($L > 10^{43}$ erg s^{-1}), light curve shape and duration (time above half-maximum of < 12 days), radius and velocity evolution, and hot continuum-dominated spectra. There are other objects that have been suggested as progenitors to the rapidly evolving and luminous transients, including stripped massive stars (Tauris et al., 2013; Kleiser & Kasen, 2014), ".Ia" SNe from detonations of helium shells on WDs (Bildsten et al., 2007b; Shen et al., 2010; Perets et al., 2010), and shock breakout from a dense circumstellar shell (Ofek et al., 2010). Due to the very fast light curves and velocities generated by the exploding WD merger remnant models shown here (Figures 7.7-7.9), we conclude that they can only account for a subset of this observed class of rapidly evolving, luminous transients. The lack of H and He and strong enrichment of ^{12}C and ^{24}Mg in the spectra for these objects may help to distinguish them from other possible fast and luminous transients.

Chapter 8

Future Work

Looking forward, there are a number of improvements and extensions to the work in this dissertation that could prove fruitful. To start, there are some improvements to `MESA` that would enable simulations of AM CVn systems and their progenitors (discussed in Chapter 2) to run much more quickly and smoothly, and thus allow a broader study of the parameter space. This includes a more complete and denser coverage of equation of state (EOS) tables. These He donating models struggled to evolve smoothly when the orbital period drops below 15 minutes, due to the surface convection zone extending down into the blending region between OPAL and HELM (Rogers & Nayfonov, 2002; Timmes & Swesty, 2000). The poor coverage and low density of the tables lead to uncertainty in the EOS in this region, causing the surface convection zone base location to be numerically noisy. The quickly changing convection zone depth causes the radius to also be numerically noisy, and since the mass loss rate depends sensitively on the radius, the mass loss rate is even noisier, leading to changes of the mass transfer rate of an order of magnitude between steps unless very small timesteps were taken. This means that these simulations required hundreds of thousands to millions of timesteps, which takes weeks or months to run. Therefore, we could only afford to run a small handful of

simulations for each paper.

Furthermore, the existing mass loss mechanisms in the binary module of MESA are not well suited for degenerate objects, since they all rely sensitively on the ratio of the radius to the RL in one form or another. The basic mechanism they follow is to raise the mass loss rate if the radius is too big and to lower the mass loss rate if the radius is too small. The problem for degenerate objects is that they have an inverse mass-radius relation, so an increase in the mass transfer rate causes an increase in the radius, and vice versa, which is the opposite of the expectation of the existing mass loss mechanisms in MESA. This means that, along with the small timesteps enforced by the convection zone entering into an EOS blending region, each step takes multiple iterations to decide on an appropriate mass loss rate, multiplying the run-time several times over. Until these problems are addressed in MESA, these types of studies will be limited to only a few models per study.

There are also some improvements on the predictions of observed systems given in this dissertation that can be made with updated physics. We modeled an observed system in Chapter 2, CD-30° 11223 (Geier et al., 2013), and made some predictions about its future. Recently Bauer et al. (2017) took the mass transfer history from Brooks et al. (2015) (Chapter 2) and included NCO reactions in the nuclear network for the accreting WD and found that the shell ignites much closer to the base of the He layer at a somewhat earlier time. Furthermore, Shen & Moore (2014) showed that a much larger network that allowed proton-catalyzed reactions found conditions suitable for detonations at much lower envelope masses than previous work. Including rotation (Yoon et al., 2004) and magnetic fields (Maeder & Meynet, 2003) can also have significant effects on the build up and ignition of He envelopes on WDs.

Due to the length of time many of these simulations took, we were limited in the amount of parameter space we could cover. Future studies could expand the covered

parameter space for improved formation rates and statistics. In Chapter 3 we discuss the phenomenon of carbon shell ignitions, followed by carbon flames, on He accreting and steady burning C/O WDs. The parameter space of this study, however, is quite limited, as we only explored two different initial C/O WD masses and two initial orbital periods. In order to increase the accuracy of binary population synthesis (BPS) studies, it would be useful to map out the parameter space of the initial He star mass, initial WD mass, and initial orbital period of binary systems that experience a carbon shell ignition before a carbon core ignition, thereby removing such systems from the progenitors to SNe Ia.

Additionally, in Chapter 3 we discuss the uncertainty of the rates of angular momentum loss via mass loss from the system (§3.1.3). We chose to assign the sytem mass loss the specific angular momentum of the accreting WD, but this could be an underestimate, as found by Pejcha et al. (2016) who studied double RL filling systems. A similar study to that of Pejcha et al. (2016) but with He star + WD systems would prove quite useful to the field.

Chapter 4 discusses the mixing between the C/O core and O/Ne mantle in cooling hybrid C/O/Ne WDs. Any future studies using multi-dimensional hydrodynamic simulations to explode these hybrid WDs should use models with fully mixed interiors. Additionally, we include in our paper a citation to Lecoanet et al. (2016) that suggests that the buoyancy barrier across the C flame in the cores of AGB stars is too great to allow any convective boundary mixing that might quench the C flame. This would prevent any hybrid C/O/Ne WDs from forming in the first place. Since there is currently no way to detect if any observed WDs have hybrid C/O/Ne structures in their interiors, more theoretical and computational work is required to confirm whether such an interior structure is likely form.

After we published the paper in Chapter 4, we received an email from the authors of Denissenkov et al. (2013) who informed us that some of their calculations using larger

nuclear networks showed a smaller ΔY_e across the core-mantle boundary. Given this smaller ΔY_e, we ran some simulations and found that the mixing was slower, but not significantly slower and we stand by the conclusions in §4.5.

In Chapter 5 we show our calculations of He star + WD progenitors to AIC, which happens due to electron captures in the center that relieve pressure and lead to a runaway collapse to a NS, but we never show any electron capture calculations, as we cut off our models just before then. Schwab et al. (2015) shows how electron capture reactions can be implemented in `MESA`, but in our more realistic models, the electron capture reactions began to generate and interact with convection zones in a way that was numerically unstable. We were therefore unable to incorporate electron capture reactions into our models, but future improvements to the implementation of these rates, which are currently under development, may allow us to perform more realistic simulations during this last phase before the models become hydrodynamic. This could help better inform the initial conditions for multi-dimensional hydrodynamic simulations of AIC. Furthermore, a full calculation of a C flame in a C/O WD that propagates all the way to the center would tell us if the flame lifts the core degeneracy sufficiently to allow an evolution that leads to Fe cores as in Schwab et al. (2016), or if it leads to electron captures in O/Ne as in Schwab et al. (2015).

We discuss the evolution of He shell burning on the merger remnants of massive C/O and O/Ne WDs with He WDs in Chapter 7. We discovered that the convective envelopes couple with the burning layer at core masses $M_{\rm core} \approx 1.12 - 1.20 M_{\odot}$. This means that the He burning products are shared with the entire convective envelope, instead of being deposited on the core. The resulting metal enrichment of the extended envelopes pushes them off the existing EOS tables, meaning that none of the EOS tables are appropriate for the envelope of these massive WD merger remnant models. We showed the results of using the EOS's that covered the relevant area in ρ, T space, but a more realistic

treatment would require new EOS tables for the metallicities reached by the envelopes in our models. Additionally, future observational surveys may find more rapid and luminous transients that can best be explained by our exploding WD merger remnant models.

Bibliography

Alcock, C., Allsman, R. A., Alves, D. R., Axelrod, T. S., Becker, A., Bennett, D. P., Clayton, G. C., Cook, K. H., Dalal, N., Drake, A. J., Freeman, K. C., Geha, M., Gordon, K. D., Griest, K., Kilkenny, D., Lehner, M. J., Marshall, S. L., Minniti, D., Misselt, K. A., Nelson, C. A., Peterson, B. A., Popowski, P., Pratt, M. R., Quinn, P. J., Stubbs, C. W., Sutherland, W., Tomaney, A., Vandehei, T., & Welch, D. L. 2001, The Astrophysical Journal, 554, 298

Althaus, L. G., Miller Bertolami, M. M., & Córsico, A. H. 2013, A&A, 557, A19

Althaus, L. G., Serenelli, A. M., & Benvenuto, O. G. 2001, MNRAS, 323, 471

Antoniadis, J., Tauris, T. M., Ozel, F., Barr, E., Champion, D. J., & Freire, P. C. C. 2016, eprint arXiv:1605.01665

Arcavi, I., Wolf, W. M., Howell, D. A., Bildsten, L., Leloudas, G., Hardin, D., Prajs, S., Perley, D. A., Svirski, G., Gal-Yam, A., Katz, B., McCully, C., Cenko, S. B., Lidman, C., Sullivan, M., Valenti, S., Astier, P., Balland, C., Carlberg, R. G., Conley, A., Fouchez, D., Guy, J., Pain, R., Palanque-Delabrouille, N., Perrett, K., Pritchet, C. J., Regnault, N., Rich, J., & Ruhlmann-Kleider, V. 2016, The Astrophysical Journal, 819, 35

Arnett, D. & Livne, E. 1994, The Astrophysical Journal, 427, 330

Badenes, C. & Maoz, D. 2012, The Astrophysical Journal Letters, 749, L11

Bailyn, C. D. & Grindlay, J. E. 1990, The Astrophysical Journal, 353, 159

Bauer, E. B., Schwab, J., & Bildsten, L. 2017, The Astrophysical Journal, 845, 97

Benz, W., Bowers, R. L., Cameron, A. G. W., & Press, W. H. . 1990, The Astrophysical Journal, 348, 647

Biermann, P. & Kippenhahn, R. 1971, A&A, 14, 32

Bildsten, L., Shen, K. J., Weinberg, N. N., & Nelemans, G. 2007a, The Astrophysical Journal Letters, 662, L95

—. 2007b, ApJL, 662, L95

Bildsten, L., Townsley, D. M., Deloye, C. J., & Nelemans, G. 2006, The Astrophysical Journal, 640, 466

Bisscheroux, B. C., Pols, O. R., Kahabka, P., Belloni, T., & van den Heuvel, E. P. J. 1997, Astronomy and Astrophysics, 317, 815

Blinnikov, S. I. & Bartunov, O. S. 1993, A&A, 273, 106

Blinnikov, S. I., Röpke, F. K., Sorokina, E. I., Gieseler, M., Reinecke, M., Travaglio, C., Hillebrandt, W., & Stritzinger, M. 2006, A&A, 453, 229

Bloecker, T. 1995, A&A, 297, 727

Boyles, J., Lorimer, D. R., Turk, P. J., Mnatsakanov, R., Lynch, R. S., Ransom, S. M., Freire, P. C., & Belczynski, K. 2011, The Astrophysical Journal, 742, 51

Bravo, E., Gil-Pons, P., Gutiérrez, J. L., & Doherty, C. L. 2016, A&A, 589, A38

Brooks, J., Bildsten, L., Marchant, P., & Paxton, B. 2015, The Astrophysical Journal, 807, 74

Brooks, J., Bildsten, L., Schwab, J., & Paxton, B. 2016, The Astrophysical Journal, 821, 28

Brooks, J., Kupfer, T., & Bildsten, L. 2017a, ArXiv e-prints

Brooks, J., Schwab, J., Bildsten, L., Quataert, E., & Paxton, B. 2017b, The Astrophysical Journal, 843, 151

—. 2017c, The Astrophysical Journal Letters, 834, L9

Brown, J. M., Garaud, P., & Stellmach, S. 2013, The Astrophysical Journal, 768, 34

Brown, W. R., Kilic, M., Kenyon, S. J., & Gianninas, A. 2016, The Astrophysical Journal, 824, 46

Buchler, J. R. & Yueh, W. R. 1976, The Astrophysical Journal, 210, 440

Campbell, C. G. 1983, MNRAS, 205, 1031

—. 1984, MNRAS, 207, 433

Canal, R., Isern, J., & Labay, J. 1990, Annual Review of Astronomy and Astrophysics, 28, 183

Caughlan, G. R. & Fowler, W. A. 1988, Atomic Data and Nuclear Data Tables, 40, 283

Chamulak, D. A., Brown, E. F., Timmes, F. X., & Dupczak, K. 2008, The Astrophysical Journal, 677, 160

Chen, M. C., Herwig, F., Denissenkov, P. A., & Paxton, B. 2014, Monthly Notices of the Royal Astronomical Society, 440, 1274

Chen, W.-C., Liu, X.-W., Xu, R.-X., & Li, X.-D. 2011, MNRAS, 410, 1441

Clayton, G. C. 2012, Journal of the American Association of Variable Star Observers (JAAVSO), 40, 539

Clayton, G. C. 2013, in Astronomical Society of the Pacific Conference Series, Vol. 469, 18th European White Dwarf Workshop., 133

Clayton, G. C., Geballe, T. R., Herwig, F., Fryer, C., & Asplund, M. 2007, The Astrophysical Journal, 662, 1220

Constantino, T., Campbell, S. W., Christensen-Dalsgaard, J., Lattanzio, J. C., & Stello, D. 2015, MNRAS, 452, 123

Cumming, A. & Bildsten, L. 2001, The Astrophysical Journal, 559, L127

Cyburt, R. H., Amthor, A. M., Ferguson, R., Meisel, Z., Smith, K., Warren, S., Heger, A., Hoffman, R. D., Rauscher, T., Sakharuk, A., Schatz, H., Thielemann, F. K., & Wiescher, M. 2010, The Astrophysical Journal Letters Supplement Series, 189, 240

Dan, M., Guillochon, J., Brüggen, M., Ramirez-Ruiz, E., & Rosswog, S. 2015, MNRAS, 454, 4411

Dan, M., Rosswog, S., Brüggen, M., & Podsiadlowski, P. 2014, MNRAS, 438, 14

Darbha, S., Metzger, B. D., Quataert, E., Kasen, D., Nugent, P., & Thomas, R. 2010, Monthly Notices of the Royal Astronomical Society, 409, 846

Deloye, C. J., Taam, R. E., Winisdoerffer, C., & Chabrier, G. 2007, MNRAS, 381, 525

Denissenkov, P. A., Herwig, F., Truran, J. W., & Paxton, B. 2013, The Astrophysical Journal, 772, 37

Denissenkov, P. A., Truran, J. W., Herwig, F., Jones, S., Paxton, B., Nomoto, K., Suzuki, T., & Toki, H. 2015, Monthly Notices of the Royal Astronomical Society, 447, 2696

Dessart, L., Burrows, A., Ott, C. D., Livne, E., Yoon, S., & Langer, N. 2006, The Astrophysical Journal, 644, 1063

Doherty, C. L., Siess, L., Lattanzio, J. C., & Gil-Pons, P. 2010, MNRAS, 401, 1453

Dominguez, I., Chieffi, A., Limongi, M., & Straniero, O. 1999, The Astrophysical Journal, 524, 226

Drout, M. R., Chornock, R., Soderberg, A. M., Sanders, N. E., McKinnon, R., Rest, A., Foley, R. J., Milisavljevic, D., Margutti, R., Berger, E., Calkins, M., Fong, W., Gezari, S., Huber, M. E., Kankare, E., Kirshner, R. P., Leibler, C., Lunnan, R., Mattila, S., Marion, G. H., Narayan, G., Riess, A. G., Roth, K. C., Scolnic, D., Smartt, S. J., Tonry, J. L., Burgett, W. S., Chambers, K. C., Hodapp, K. W., Jedicke, R., Kaiser, N., Magnier, E. A., Metcalfe, N., Morgan, J. S., Price, P. A., & Waters, C. 2014, The Astrophysical Journal, 794, 23

Dufton, P. L. 1972, Monthly Notices of the Royal Astronomical Society, 159, 79

Eggleton, P. P. 1983, The Astrophysical Journal, 268, 368

Farmer, R., Fields, C. E., & Timmes, F. X. 2015, The Astrophysical Journal, 807, 184

Fink, M., Hillebrandt, W., & Röpke, F. K. 2007, A&A, 476, 1133

Fink, M., Kromer, M., Seitenzahl, I. R., Ciaraldi-Schoolmann, F., Ropke, F. K., Sim, S. A., Pakmor, R., Ruiter, A. J., & Hillebrandt, W. 2013, Monthly Notices of the Royal Astronomical Society, 438, 1762

Fink, M., Röpke, F. K., Hillebrandt, W., Seitenzahl, I. R., Sim, S. A., & Kromer, M. 2010, A&A, 514, A53

Fuller, J. & Lai, D. 2014, MNRAS, 444, 3488

Fürst, F., Walton, D. J., Harrison, F. A., Stern, D., Barret, D., Brightman, M., Fabian, A. C., Grefenstette, B., Madsen, K. K., Middleton, M. J., Miller, J. M., Pottschmidt, K., Ptak, A., Rana, V., & Webb, N. 2016, The Astrophysical Journal Letters, 831, L14

García-Berro, E., Ritossa, C., & Iben, I. 1997, The Astrophysical Journal, 485, 765

Geier, S., Fürst, F., Ziegerer, E., Kupfer, T., Heber, U., Irrgang, A., Wang, B., Liu, Z., Han, Z., Sesar, B., Levitan, D., Kotak, R., Magnier, E., Smith, K., Burgett, W. S., Chambers, K., Flewelling, H., Kaiser, N., Wainscoat, R., & Waters, C. 2015, Science, 347, 1126

Geier, S., Marsh, T. R., Wang, B., Dunlap, B., Barlow, B. N., Scha, V., Chen, X., & Irrgang, A. 2013, Astronomy & Astrophysics, 554, 1

Geier, S., Marsh, T. R., Wang, B., Dunlap, B., Barlow, B. N., Schaffenroth, V., Chen, X., Irrgang, A., Maxted, P. F. L., Ziegerer, E., Kupfer, T., Miszalski, B., Heber, U., Han, Z., Shporer, A., Telting, J. H., Gänsicke, B. T., Østensen, R. H., O'Toole, S. J., & Napiwotzki, R. 2013, A&A, 554, A54

Gil-Pons, P. & García-Berro, E. 2001, Astronomy and Astrophysics, 375, 87

Guillochon, J., Dan, M., Ramirez-Ruiz, E., & Rosswog, S. 2010, The Astrophysical Journal Letters, 709, L64

Hachisu, I., Kato, M., & Nomoto, K. 1996, The Astrophysical Journal, 470, L97

—. 1999, The Astrophysical Journal, 522, 487

Hamann, W.-R., Gruschinske, J., Kudritzki, R. P., & Simon, K. P. 1981, A&A, 104, 249

Han, Z. 1998, MNRAS, 296, 1019

Han, Z., Podsiadlowski, P., Maxted, P. F. L., & Marsh, T. R. 2003, MNRAS, 341, 669

Han, Z., Podsiadlowski, P., Maxted, P. F. L., Marsh, T. R., & Ivanova, N. 2002, MNRAS, 336, 449

Hills, J. G. 1988, Nature, 331, 687

Howell, D. A. 2011, Nature Communications, 2, 350

Iben, I. & Tutukov, A. 1991, The Astrophysical Journal, 370, 615

—. 1994a, The Astrophysical Journal, 431, 264

Iben, Jr., I. & Tutukov, A. V. 1984, The Astrophysical Journal Letters Supplement Series, 54, 335

Iben, Icko, J. & Tutukov, A. V. 1989, The Astrophysical Journal, 342, 430

—. 1994b, The Astrophysical Journal, 431, 264

Israel, G. L., Papitto, A., Esposito, P., Stella, L., Zampieri, L., Belfiore, A., Rodríguez Castillo, G. A., De Luca, A., Tiengo, A., Haberl, F., Greiner, J., Salvaterra, R., Sandrelli, S., & Lisini, G. 2017, MNRAS, 466, L48

Israel, G. L., Stella, L., Angelini, L., White, N. E., & Giommi, P. 1995, IAU Circ., No. 6277, #1 (1995). Edited by Green, D. W. E., 6277

Israel, G. L., Stella, L., Angelini, L., White, N. E., Kallman, T. R., Giommi, P., & Treves, A. 1996, The Astrophysical Journal, Volume 474, Issue 1, pp. L53-L56., 474, L53

Jaschek, C. & Gómez, A. E. 1970, Publications of the Astronomical Society of the Pacific, 82, 809

Jaschek, M. & Jaschek, C. 1963, Publications of the Astronomical Society of the Pacific, 75, 365

Jeffery, C. S. 1988, MNRAS, 235, 1287

Jeffery, C. S. 2008a, in Astronomical Society of the Pacific Conference Series, Vol. 391, Hydrogen-Deficient Stars, ed. A. Werner & T. Rauch, 53

Jeffery, C. S. 2008b, in Astronomical Society of the Pacific Conference Series, Vol. 391, Hydrogen-Deficient Stars, ed. A. Werner & T. Rauch, 3

Jeffery, C. S., Karakas, A. I., & Saio, H. 2011, MNRAS, 414, 3599

Jones, S., Roepke, F. K., Pakmor, R., Seitenzahl, I. R., Ohlmann, S. T., & Edelmann, P. V. F. 2016, Astronomy & Astrophysics, Volume 593, id.A72, 11 pp., 593

Joss, P. C., Salpeter, E. E., & Ostriker, J. P. 1973, The Astrophysical Journal, 181, 429

Justham, S., Wolf, C., Podsiadlowski, P., & Han, Z. 2009, A&A, 493, 1081

Kahabka, P. & van den Heuvel, E. P. J. 1997, Annual Review of Astronomy and Astrophysics, 35, 69

Karakas, A. I., Ruiter, A. J., & Hampel, M. 2015, The Astrophysical Journal, 809, 184

Kasliwal, M. M., Kulkarni, S. R., Gal-Yam, A., Yaron, O., Quimby, R. M., Ofek, E. O., Nugent, P., Poznanski, D., Jacobsen, J., Sternberg, A., Arcavi, I., Howell, D. A., Sullivan, M., Rich, D. J., Burke, P. F., Brimacombe, J., Milisavljevic, D., Fesen, R., Bildsten, L., Shen, K., Cenko, S. B., Bloom, J. S., Hsiao, E., Law, N. M., Gehrels,

N., Immler, S., Dekany, R., Rahmer, G., Hale, D., Smith, R., Zolkower, J., Velur, V., Walters, R., Henning, J., Bui, K., & McKenna, D. 2010, The Astrophysical Journal Letters, 723, L98

Kato, M. & Hachisu, I. 2004, The Astrophysical Journal, 613, L129

Kato, M., Hachisu, I., Kiyota, S., & Saio, H. 2008, The Astrophysical Journal, 684, 1366

King, A., Lasota, J.-P., & Kluzniak, W. 2017, ArXiv e-prints

Kippenhahn, R. 1981, A&A, 102, 293

Kippenhahn, R., Ruschenplatt, G., & Thomas, H.-C. 1980, A&A, 91, 175

Kitaura, F. S., Janka, H.-T., & Hillebrandt, W. 2006, A&A, 450, 345

Kleiser, I. K. W. & Kasen, D. 2014, MNRAS, 438, 318

Koen, C., Orosz, J. A., & Wade, R. A. 1998, MNRAS, 300, 695

Kromer, M., Ohlmann, S. T., Pakmor, R., Ruiter, A. J., Hillebrandt, W., Marquardt, K. S., Röpke, F. K., Seitenzahl, I. R., Sim, S. A., & Taubenberger, S. 2015, MNRAS, 450, 3045

Kromer, M., Sim, S. A., Fink, M., Röpke, F. K., Seitenzahl, I. R., & Hillebrandt, W. 2010, The Astrophysical Journal, 719, 1067

Kudritzki, R. P. & Simon, K. P. 1978, Astronomy and Astrophysics, 70, 653

Kupfer, T., Geier, S., Heber, U., Østensen, R. H., Barlow, B. N., Maxted, P. F. L., Heuser, C., Schaffenroth, V., & Gänsicke, B. T. 2015, A&A, 576, A44

Kupfer, T., van Roestel, J., Brooks, J., Geier, S., Marsh, T. R., Groot, P. J., Bloemen, S., Prince, T. A., Bellm, E., Heber, U., Bildsten, L., Miller, A. A., Dyer, M. J., Dhillon,

V. S., Green, M., Irawati, P., Laher, R., Littlefair, S. P., Shupe, D. L., Steidel, C. C., Rattansoon, S., & Pettini, M. 2017, The Astrophysical Journal, 835, 131

Kurucz, R. L. & Bell, B. 1995, Atomic line list

Kwiatkowski, . 2015, eprint arXiv:1512.00678

Landau, L. D. & Lifshitz, E. M. 1975, The classical theory of fields

Law, N. M., Kulkarni, S. R., Dekany, R. G., Ofek, E. O., Quimby, R. M., Nugent, P. E., Surace, J., Grillmair, C. C., Bloom, J. S., Kasliwal, M. M., Bildsten, L., Brown, T., et al. 2009, PASP, 121, 1395

Lecoanet, D., Schwab, J., Quataert, E., Bildsten, L., Timmes, F. X., Burns, K. J., Vasil, G. M., Oishi, J. S., & Brown, B. P. 2016, The Astrophysical Journal, 832, 71

Limongi, M. & Tornambe, A. 1991, The Astrophysical Journal, 371, 317

Liu, J.-F., Bregman, J. N., Bai, Y., Justham, S., & Crowther, P. 2013, Nature, 503, 500

Liu, W.-M., Chen, W.-C., Wang, B., & Han, Z. W. 2010, Astronomy & Astrophysics, 523, A3

Livne, E. 1990, The Astrophysical Journal Letters, 354, L53

Livne, E. & Arnett, D. 1995, The Astrophysical Journal, 452, 62

Livne, E. & Glasner, A. S. 1991, The Astrophysical Journal, 370, 272

Maeder, A. & Meynet, G. 2003, A&A, 411, 543

Maoz, D., Mannucci, F., & Nelemans, G. 2014, Annual Review of Astronomy and Astrophysics, 52, 107

Marigo, P. & Aringer, B. 2009, A&A, 508, 1539

Marsh, T. R., Nelemans, G., & Steeghs, D. 2004, MNRAS, 350, 113

Martínez-Rodríguez, H., Piro, A. L., Schwab, J., & Badenes, C. 2016, The Astrophysical Journal, 825, 57

Melson, T., Janka, H.-T., & Marek, A. 2015, The Astrophysical Journal Letters, 801, L24

Menon, A., Herwig, F., Denissenkov, P. A., Clayton, G. C., Staff, J., Pignatari, M., & Paxton, B. 2013, The Astrophysical Journal, 772, 59

Mereghetti, S., La Palombara, N., Tiengo, A., Pizzolato, F., Esposito, P., Woudt, P. A., Israel, G. L., & Stella, L. 2011, The Astrophysical Journal, 737, 51

Mereghetti, S., Palombara, N. L., Tiengo, A., Sartore, N., Esposito, P., Israel, G. L., & Stella, L. 2013, Astronomy & Astrophysics, 46, 1

Mereghetti, S., Pintore, F., Esposito, P., La Palombara, N., Tiengo, A., Israel, G. L., & Stella, L. 2016, Monthly Notices of the Royal Astronomical Society, 458, 3523

Mereghetti, S., Tiengo, A., Esposito, P., Palombara, N. L., Israel, G. L., & Stella, L. 2009, Science, 325, 1222

Metzger, B. D. 2012, MNRAS, 419, 827

Metzger, B. D., Piro, A. L., & Quataert, E. 2009, Monthly Notices of the Royal Astronomical Society, 396, 1659

Michaud, G., Richer, J., & Richard, O. 2007, The Astrophysical Journal, 670, 1178

Miyaji, S., Sugimoto, D., Nomoto, K., & Yokoi, K. 1980, In: International Cosmic Ray Conference, 2, 13

Moll, R. & Woosley, S. E. 2013, The Astrophysical Journal, 774, 137

Moore, K., Townsley, D. M., & Bildsten, L. 2013, The Astrophysical Journal, 776, 97

Moriya, T. J. & Eldridge, J. J. 2016, MNRAS, 461, 2155

Motch, C., Pakull, M. W., Soria, R., Grisé, F., & Pietrzyński, G. 2014, Nature, 514, 198

Müller, S. 2009, Master's thesis, University of Erlangen-Nuremberg, Germany

Nelemans, G. 2010, Astrophysics and Space Science, 329, 25

Nelemans, G., Portegies Zwart, S. F., Verbunt, F., & Yungelson, L. R. 2001, A&A, 368, 939

Nomoto, K. 1982a, The Astrophysical Journal, 257, 780

—. 1982b, The Astrophysical Journal, 253, 798

Nomoto, K. 1984, The Astrophysical Journal, 277, 791

—. 1987, The Astrophysical Journal, 322, 206

Nomoto, K. & Iben, I., J. 1985, The Astrophysical Journal, 297, 531

Nomoto, K. & Kondo, Y. 1991, The Astrophysical Journal, 367, L19

Nomoto, K., Miyaji, S., Sugimoto, D., & Yokoi, K. 1979, Bulletin of the American Astronomical Society, 11

Nomoto, K., Saio, H., Kato, M., & Hachisu, I. 2007, The Astrophysical Journal, 663, 1269

Ofek, E. O., Rabinak, I., Neill, J. D., Arcavi, I., Cenko, S. B., Waxman, E., Kulkarni, S. R., Gal-Yam, A., Nugent, P. E., Bildsten, L., Bloom, J. S., Filippenko, A. V., Forster, K., Howell, D. A., Jacobsen, J., Kasliwal, M. M., Law, N., Martin, C., Poznanski, D., Quimby, R. M., Shen, K. J., Sullivan, M., Dekany, R., Rahmer, G., Hale, D., Smith, R., Zolkower, J., Velur, V., Walters, R., Henning, J., Bui, K., & McKenna, D. 2010, The Astrophysical Journal, 724, 1396

Paczyński, B. 1967, Acta Astronomica, 17, 287

—. 1973, Acta Astronomica, 23, 1

Paczynski, B. & Zytkow, A. N. 1978, The Astrophysical Journal, 222, 604

Paczyski, B. 1971, Acta Astronomica, 21

Pakmor, R., Hachinger, S., Röpke, F. K., & Hillebrandt, W. 2011, Astronomy & Astrophysics, 528, A117

Pakmor, R., Kromer, M., Röpke, F. K., Sim, S. A., Ruiter, A. J., & Hillebrandt, W. 2010, Nature, 463, 61

Pakmor, R., Kromer, M., Taubenberger, S., Sim, S. A., Röpke, F. K., & Hillebrandt, W. 2012, The Astrophysical Journal, 747, L10

Pakmor, R., Kromer, M., Taubenberger, S., & Springel, V. 2013, The Astrophysical Journal Letters, 770, L8

Paxton, B., Bildsten, L., Dotter, A., Herwig, F., Lesaffre, P., & Timmes, F. 2011, The Astrophysical Journal Supplement Series, 192, 3

Paxton, B., Cantiello, M., Arras, P., Bildsten, L., Brown, E. F., Dotter, A., Mankovich, C., Montgomery, M. H., Stello, . D., Timmes, F. X., & Townsend, R. 2013, The Astrophysical Journal Letters Supplement Series, 208, 4

Paxton, B., Marchant, P., Schwab, J., Bauer, E. B., Bildsten, L., Cantiello, M., Dessart, L., Farmer, R., Hu, H., Langer, N., Townsend, R. H. D., Townsley, D. M., & Timmes, F. X. 2015, The Astrophysical Journal Letters Supplement Series, 220, 15

Pejcha, O., Metzger, B. D., & Tomida, K. 2016, MNRAS, 455, 4351

Perets, H. B., Gal-Yam, A., Mazzali, P. A., Arnett, D., Kagan, D., Filippenko, A. V., Li, W., Arcavi, I., Cenko, S. B., Fox, D. B., Leonard, D. C., Moon, D.-S., Sand, D. J., Soderberg, A. M., Anderson, J. P., James, P. A., Foley, R. J., Ganeshalingam, M., Ofek, E. O., Bildsten, L., Nelemans, G., Shen, K. J., Weinberg, N. N., Metzger, B. D., Piro, A. L., Quataert, E., Kiewe, M., & Poznanski, D. 2010, Nature, 465, 322

Piersanti, L., Tornambé, A., & Yungelson, L. R. 2014, MNRAS, 445, 3239

Piro, A. L. 2015, The Astrophysical Journal, 801, 137

Piro, A. L. & Bildsten, L. 2008, The Astrophysical Journal, 673, 1009

Piro, A. L. & Kulkarni, S. R. 2013, The Astrophysical Journal, 762, L17

Poznanski, D., Chornock, R., Nugent, P. E., Bloom, J. S., Filippenko, A. V., Ganeshalingam, M., Leonard, D. C., Li, W., & Thomas, R. C. 2010, Science, 327, 58

Prialnik, D. & Kovetz, A. 1995, The Astrophysical Journal, 445, 789

Radice, D., Burrows, A., Vartanyan, D., Skinner, M. A., & Dolence, J. C. 2017, ArXiv e-prints

Rau, A., Kulkarni, S. R., Law, N. M., Bloom, J. S., Ciardi, D., Djorgovski, G. S., Fox, D. B., Gal-Yam, A., Grillmair, C. C., Kasliwal, M. M., Nugent, P. E., Ofek, E. O., Quimby, R. M., Reach, W. T., Shara, M., Bildsten, L., Cenko, S. B., Drake, A. J., Filippenko, A. V., Helfand, D. J., Helou, G., Howell, D. A., Poznanski, D., & Sullivan, M. 2009, Publications of the Astronomical Society of the Pacific, 121, 1334

Ritossa, C., Garcia-Berro, E., & Iben, Icko, J. 1996, The Astrophysical Journal, 460, 489

Ritter, H. 1988, A&A, 202, 93

Robinson, E. L. 1976, Annual Review of Astronomy and Astrophysics, 14, 119

Rogers, F. J. & Nayfonov, A. 2002, The Astrophysical Journal, 576, 1064

Ruiter, A. J., Belczynski, K., & Fryer, C. 2009, The Astrophysical Journal, 699, 2026

Ruiter, A. J., Belczynski, K., Sim, S. A., Seitenzahl, I. R., & Kwiatkowski, D. 2014, MNRAS, 440, L101

Ruiter, A. J., Sim, S. A., Pakmor, R., Kromer, M., Seitenzahl, I. R., Belczynski, K., Fink, M., Herzog, M., Hillebrandt, W., Ropke, F. K., & Taubenberger, S. 2012, Monthly Notices of the Royal Astronomical Society, 429, 1425

Saio, H. 1988, MNRAS, 235, 203

Saio, H. 2008, in Astronomical Society of the Pacific Conference Series, Vol. 391, Hydrogen-Deficient Stars, ed. A. Werner & T. Rauch, 69

Saio, H. & Jeffery, C. S. 1988, The Astrophysical Journal, 328, 714

—. 2002, MNRAS, 333, 121

Saio, H. & Nomoto, K. 1985, Astronomy and Astrophysics (ISSN 0004-6361), 150

—. 1998, The Astrophysical Journal, 500, 388

Sato, Y., Nakasato, N., Tanikawa, A., Nomoto, K., Maeda, K., & Hachisu, I. 2015, The Astrophysical Journal, 807, 105

Savonije, G. J., de Kool, M., & van den Heuvel, E. P. J. 1986, A&A, 155, 51

Schindler, J.-T., Green, E. M., & Arnett, W. D. 2015, The Astrophysical Journal, 806, 178

Schwab, J., Quataert, E., & Bildsten, L. 2015, Monthly Notices of the Royal Astronomical Society, 453, 1910

Schwab, J., Quataert, E., & Bildsten, L. 2015, MNRAS, 453, 1910

Schwab, J., Quataert, E., & Kasen, D. 2016, Monthly Notices of the Royal Astronomical Society, Volume 463, Issue 4, p.3461-3475, 463, 3461

Schwarzschild, M. & Härm, R. 1965, The Astrophysical Journal, 142, 855

Shen, K. J. 2015, The Astrophysical Journal Letters, 805, L6

Shen, K. J. & Bildsten, L. 2007, The Astrophysical Journal, 660, 1444

—. 2009, The Astrophysical Journal, 699, 1365

Shen, K. J. & Bildsten, L. 2014, The Astrophysical Journal, 785, 61

Shen, K. J., Bildsten, L., Kasen, D., & Quataert, E. 2012, The Astrophysical Journal, 748, 35

Shen, K. J., Kasen, D., Weinberg, N. N., Bildsten, L., & Scannapieco, E. 2010, The Astrophysical Journal, 715, 767

Shen, K. J. & Moore, K. 2014, The Astrophysical Journal, 797, 46

Sim, S. A., Fink, M., Kromer, M., Röpke, F. K., Ruiter, A. J., & Hillebrandt, W. 2012, MNRAS, 420, 3003

Sim, S. A., Röpke, F. K., Hillebrandt, W., Kromer, M., Pakmor, R., Fink, M., Ruiter, A. J., & Seitenzahl, I. R. 2010, The Astrophysical Journal Letters, 714, L52

Smith, N. 2013, MNRAS, 434, 102

Stickland, D. J. & Lloyd, C. 1994, The Observatory, 114, 41

Stroeer, A. & Nelemans, G. 2009, MNRAS, 400, L24

Takahashi, K., Yoshida, T., & Umeda, H. 2013, The Astrophysical Journal, 771, 28

Tanaka, M., Tominaga, N., Morokuma, T., Yasuda, N., Furusawa, H., Baklanov, P. V., Blinnikov, S. I., Moriya, T. J., Doi, M., Jiang, J.-a., Kato, T., Kikuchi, Y., Kuncarayakti, H., Nagao, T., Nomoto, K., & Taniguchi, Y. 2016, The Astrophysical Journal, 819, 5

Tauris, T. M. 2015, ArXiv e-prints

Tauris, T. M., Sanyal, D., Yoon, S.-C., & Langer, N. 2013, Astronomy & Astrophysics, 558, A39

Thackeray, A. D. 1970, Monthly Notices of the Royal Astronomical Society, 150, 215

Timmes, F. X. & Swesty, F. D. 2000, The Astrophysical Journal Letters Supplement Series, 126, 501

Timmes, F. X., Woosley, S. E., & Taam, R. E. 1994, The Astrophysical Journal, 420, 348

Townsley, D. M. & Bildsten, L. 2004, The Astrophysical Journal, 600, 390

Townsley, D. M., Jackson, A. P., Calder, A. C., Chamulak, D. A., Brown, E. F., & Timmes, F. X. 2009, The Astrophysical Journal, 701, 1582

Townsley, D. M., Miles, B. J., Timmes, F. X., Calder, A. C., & Brown, E. F. 2016, The Astrophysical Journal Letters Supplement Series, 225, 3

Townsley, D. M., Moore, K., & Bildsten, L. 2012, The Astrophysical Journal, 755, 4

Tutukov, A. V. & Fedorova, A. V. 1989, Soviet Ast., 33, 606

Tutukov, A. V. & Yungelson, L. R. 1990, Soviet Ast., 34, 57

Verner, D. A., Verner, E. M., & Ferland, G. J. 1996, Atomic Data and Nuclear Data Tables, 64, 1

Wang, B., Li, Y., Ma, X., Liu, D.-D., Cui, X., & Han, Z. 2015, Astronomy & Astrophysics, 584, A37

Wang, B., Meng, X., Chen, X., & Han, Z. 2009, Monthly Notices of the Royal Astronomical Society, 395, 847

Wang, B., Meng, X., Chen, X., & Han, Z. 2009, MNRAS, 395, 847

Wang, B., Meng, X., Liu, D.-D., Liu, Z.-W., & Han, Z. 2014, The Astrophysical Journal, 794, L28

Webbink, R. F. 1984, The Astrophysical Journal, 277, 355

Weiss, A. 1987, A&A, 185, 165

Willcox, D. E., Townsley, D. M., Calder, A. C., Denissenkov, P. A., & Herwig, F. 2016, The Astrophysical Journal, 832, 13

Wolf, W. M., Bildsten, L., Brooks, J., & Paxton, B. 2013, The Astrophysical Journal, 777, 136

Woosley, S. E. & Baron, E. 1992, The Astrophysical Journal, 391, 228

Woosley, S. E. & Kasen, D. 2011, The Astrophysical Journal, 734, 38

Woosley, S. E. & Weaver, T. A. 1986, IN: Nucleosynthesis and its implications on nuclear and particle physics; Proceedings of the NATO Advanced Research Workshop (Fifth Moriond Astrophysics Meeting), 145

Woosley, S. E. & Weaver, T. A. 1994, The Astrophysical Journal, 423, 371

Yaron, O., Prialnik, D., Shara, M. M., & Kovetz, A. 2005, The Astrophysical Journal, 623, 398

Yoon, S.-C. & Langer, N. 2003, Astronomy and Astrophysics, 412, L53

Yoon, S.-C., Langer, N., & Scheithauer, S. 2004, A&A, 425, 217

Yungelson, L. & Livio, M. 1998, The Astrophysical Journal, 497, 168

Yungelson, L. R. 2008, Astronomy Letters, 34, 620

Zhang, X. & Jeffery, C. S. 2012, MNRAS, 426, L81

Zhang, X., Jeffery, C. S., Chen, X., & Han, Z. 2014, MNRAS, 445, 660